Università Politecnica delle Marche
Scuola di Dottorato di Ricerca in Scienze dell'Ingegneria
Corso di Dottorato in Ingegneria Industriale

Development of biomimetic propulsive systems in a multiphysics environment

Ph.D. Dissertation of:

Daniele Costa

Supervisor:

Prof. Massimo Callegari

Assistant Supervisor:

Prof. David Scaradozzi

Ph.D. Course coordinator:

Prof. F. Mandorli

XVII edition - new series

Università Politecnica delle Marche
Scuola di Dottorato di Ricerca in Scienze dell'Ingegneria
Corso di Dottorato in Ingegneria Industriale

Development of biomimetic propulsive systems in a multiphysics environment

Ph.D. Dissertation of:

Daniele Costa

Supervisor:

Prof. Massimo Callegari

Assistant Supervisor:

Prof. David Scaradozzi

Ph.D. Course coordinator:

Prof. F. Mandorli

XVII edition - new series

Università Politecnica delle Marche
Dipartimento di Ingegneria Industriale e Scienze Matematiche
Via Brecce Bianche — 60131 - Ancona, Italy

“And the Sea will grant each Man new hope, as sleep brings dreams of home.”

Christopher Columbus

Acknowledgements

Many people have supported me during my research and any merit in it is in large measure due to them. First and foremost, I would like to express my gratitude to my advisor, Prof. Ing. Massimo Callegari, whose expertise and understanding added considerably to my experience. I would also like to thank my co-advisor, Prof. Ing. David Scaradozzi, who supported me as a guide and as a source of inspiration, but above all, as the best friend I could even hope to find. Finally, I would like to thank the faculty supervisor of my Ph.D. program, Prof. Ing. Ferruccio Mandorli, who has carefully followed my education.

A very special thanks goes out to my colleagues, Prof. Ing Giacomo Palmieri, Prof. Ing. Matteo Palpacelli, Prof. Ing. Andrea Crivellini, Ing. Luca Carbonari, Ing. David Corinaldi, Ing. Daniele Massa and Ing. Matteo Franciolini, for the help and suggests they provided, and for their friendship as well.

In conclusion, I would like to thank my family: my father and my mother, for the thrust and support they provided me through my entire life, and my brilliant brother as well, who has always been my first fan and beloved sibling. Last but not least, I must particularly acknowledge my girlfriend Sara, without whose presence and love I would not have been the man I am today.

Abstract

Autonomous Underwater Vehicles (AUVs) are robotic systems capable to move underwater and complete a planned mission autonomously, thus without the presence of human operators nearby or on a ship close to the working site. While their sensors payload allows AUVs to examine the surrounding environmente and know their position, which is a fundamental issue in order to operate autonomously, the propulsive system allows the vehicle to move and thus perform its mission. Besides a hull shape optimization, which in turn reduce the resistance force that the water exercise on the AUV, a more efficient propulsive system allows to save power and thus increase the vehicle autonomy, thus reducing hull space reserved to batteries which in turn can be exploited to house a larger sensor payload.

In order to improve the propulsive performances of AUVs, bio-inspired solutions have been thoroughly investigated in the last two decades as a source of efficiency and manoeuvrability improvement: indeed, the propulsive performances evolved by aquatic animals in thousands of years are still far superior to the state of art of modern nautical technology. For example, dolphins dart through water with apparent ease, playfully bursting through the waves as they follows ships cruising at 20 nautical miles per hour; similarly, a nibble fish can reverse its direction of motion without breaking, with a turning radius of the order of 10-30% of their body length. For comparison, a ship must slow down by half of its speed to perform the same manoeuvre, with a turning radius ten times higher than the corresponding value for a fish.

Despite the efforts made to pursue the huge potential payoffs of marine animals' locomotion, the propulsive performances of biological swimmers are still far to reach. Nevertheless, the last two decades have withnessed a considerable growth in the in the study of aquatic animals propulsion and several prototypes of robotic fish have been manufactured by researchers all around the world.

The aim to replace the conventional screw propellers traditionally employed on AUVs with more efficient bio-ispired thruster has guided the author of the present dissertation during his research. In the robotic literature, biomimetic underwater vehicles usually adopt a direct drive to actuate their undulating bodies, being those piecewise-flexible open-chain mechanisms or soft and compliant structures. Therefore, the use of servomotors, which are characterized by low mechanical efficiency is a common feature among robotic fish prototypes. Therefore, in the present dissertation, two transmission mechanisms have been designed in order to replace the aforementioned direct drive actuation with more efficient solutions integrating DC motors or brushless ones. Moreover, the proposed systems are characterized by a constant velocity setting for the motor, while the alternate-rotation motion law of servomotors requires non-linear position control which increases the effort of the onboard electronic.

In order to test the worthiness of the proposed transmission system in a real case scenario, it has been adopted to drive tha biomimetic thruster, i.e. the fin, of an *ostraciiform* robotic fish. In order to predict the value of thrust force necessary to move the vehicle and correspondingly select a motor, the propulsive forces generated by fin have been investigated by adopting a multiphysics approach: computational fluid dynamics simulations and multi-body analysis

have been coupled in order to obtain a complete characterization of the vehicle dynamics and its propulsive systems. Once the motor torque has been successfully computed in the cruising condition, the mechatronic system composed by the motor, the trasnmission mechanism and its driven member, i.e. the thrust-generating fin, has been optimized by integrating a torsional spring in the fin shaft. This solution allowed to save power, and thus increase the efficiency, in the absence of a proper energy recovery system. Moreover, the method adopted to simulate the dynamic behaviour of the robotic fish manufactured by the author can be also used to size biomimetic robots of different size, once a cruise condition and target velocity have been properly set.

The aforementioned numerical predictions have been also validated experimentally on a scale model of the fin suspended in a water flume. The proposed setup has required the design and manufacturing of a custom estensimetric force sensor, sized accordingly to the computational fluid dynamics results that the tests aimed to validate. By means of this device, a complete characterization of the *ostraciifom* thruster has been obtained in a set of operating conditions close to regime of maximal propulsive efficiency.

Finally, the last topic discussed in the present dissertation regards the investigation of the forces generated by a flapping foil, a motion law that exactly matches the one exhibited by the most efficient swimmers in nature. Following a sensitivity analysis, performed by CFD techniques, a transmission mechanism has been succesfully designed and prototyped in order to generate the aforementioned motion law.

Future work will include the investigation of the propulsive performances of the resulting propulsive system, composed from the assembly of the high-performing biomimetic thruster and its driving transmission mechanism.

.

Contents

List of Figures

List of Tables

Chapter 1.

Introduction

1.1. Background

The development of Autonomous Underwater Vehicles (AUVs) has been carried out since 1970's. The concept of a robotic system capable to move underwater and complete a planned mission autonomously has a huge potential and many fields of application. The first AUV was developed at the Applied Physics Laboratory at the University of Washington as early as 1957 by Stan Murphy, Bob Francois and Terry Ewar [1]; then, with the fast improvement of artificial intelligence, control theory and computer hardware, novel and performing AUVs became reality.

According to the definition commonly adopted in the nautical field, autonomous underwater vehicles are maritime systems, independent in terms of power and intelligence [2]. They are typically manoeuvrable in three dimensions and this level of control, under most conditions of the environment, allows the vehicle to follow precise preprogramed trajectories [3].

AUVs main advantage consists in its autonomy, especially in carrying out hazardous tasks, since it avoids human operators to be underwater or on a ship near the working area [4-5].

An AUV can be employed in several applications: for intance, the oil and gas industry uses this robot to draw detailed maps of the seafloor before the installation of their infrastructures; researchers employ AUVs to acquire images and other data in order to document and monitor underwater sites, lakes, the ocean and the ocean floor. Sometimes they have been used to find or inspect the wreckages of missing airplanes and cruising boats. Therefore, in order to carry out these type of survey missions, a proper sensor payload must be installed aboard AUVs. Still, the original purpouse of the onboard acquisition devices was to allow reliable vehicle operations: in other words, instrumentation is needed to allow the robot to know its position, detect obstacles and acquire data. The pressure sensors, for example, allows the measurement of the depth, while the Doppler velocity logs (DVLs) and the inertial navigation system (INS) respectively measure the vehicle velocity with respect to the ground and its acceleration. As reliability was achieved, more sensors have been added to the electronic system in order to acquire data from the underwater environment.

While the sensor payload allows AUVs to know its position, which is a fundamental issue in order to operate autonomously, the propulsive system permits the vehicle to move and thus perform its mission. As an AUV moves at constant speed, the trust force must exactly balance the hydrodynamic resistance: the less drag it experiences, the less propulsive power it needs. However, besides hull shape optimizations, which in turn reduce the resistance force that the water exercise on the AUV, a more efficient propulsive system allows – for a given thrust

force – to save power and thus increase the vehicle autonomy, reduce the hull space reserved to batteries and then house a larger sensor payload.
In order to improve the propulsive performances of AUVs, bio-inspired solutions have been thoroughly investigated in the last two decades as a source of efficiency and manoeuvrability enhancement: indeed, fish generate high thrust forces by the coordinated movements of body, tail and fins with high mechanical efficiency; this particular motion produces an arrangement of vortices in the wake of their tails, whose rotational direction is always compatible with the desired direction of thrust, thus producing an efficient jet. On the contrary, a screw propeller generates a long jet that rotates in the direction perpendicular to those of advancemente and to the thrust vector, thus wasting a lot of power and resulting in an efficiency loss [6].
For these reasons, the swimming capabilities of marine animals are still beyond the state of art of the modern nautical technology, in terms of velocity, acceleration and manoeuvrability. Dolphins, for example, dart through water with impressive grace and apparent ease, playfully bursting through the waves as they follows ships cruising at 20 nautical miles per hours. Whereas records of the maximum speeds of fish are not always reliable and are often quite contentious, marine biologists have reported that yellowfin tuna can swim at speeds of at least 40 knots while fishing. The pike overcomes its prey with short burst of acceleration that can exceed that of gravity by about 20 times. Similarly, nibble fish can reverse their direction of motion without breaking and with a turning radius of the order of 10-30% of their body length. For comparison, a ship must slow down by 50% of its speed, sometimes even more, to perform the same manoeuvre, with a turning radius ten times higher than the corresponding value for a fish [6].
Marine animals' propulsive performances has attracted the attention of biologists long before engineers have started to take active interest on this subject: yet, in 1936, the British zoologist James Grey [7] calculated the power required for a dolphin to cruise at 20 knots (as someone had reported they did), under the hypothesis that the swimming drag could be approximated by the common expression used for a rigid model inside a turbulent flow. However, his results showed that the power required for the effort outnumbered the muscular output of the marine mammal by a factor of seven. About 60 year later, efficiency measurement performed on the first swimming robot [6] allowed to formulate the following new hypothesis in order to expain the well-known *Grey's Paradox*: an undulating body can extract kinetic energy from incoming vortices, actually lowering the apparent swimming drag when compared to a rigid equivalent. This conclusion neglects the old assumption on the higher value of the swimming drag for undulating bodies.
Despite the efforts made to pursue the huge potential payoffs of marine animals' locomotion, the propulsive performances of biological swimmers are still far to reach. Nevertheless, the last two decades have withnessed a considerable growth in the in the study of aquatic animals propulsion and several prototypes of robotic fish have been manufactured by researchers all around the world. Driven by a new way of thinking and guided by a design method based on bio-inspiration, engineers have tried to exploit the best that nature had to offer in order to improve the capabilities of underwater vehicles: the proposed solutions have included even eels [8], turtles [9], octopuses [10] and fish-shaped AUVs as well like the Ghostswimmer[11], the first commercialized robotic fish developed by Boston Engineering, Figure 1.1.
However, the possibility to replicate successfully the different swimming modes evolved by fish in thousands of years, depends from the understanding of the fluid mechanics principles exploited by marine animals' locomotion. By using a multiphysics approach consisting in

advanced mechatronic systems, as well as simulation and measurement techniques, engineers are trying to quantify the propulsive performances of biological swimmers, such as efficiency and thrust. Still, when analysing the outstanding complexity of the locomotion mechanisms exploited by fish, it is important to remember that every design results from the necessity to reach a compromise between different requirements, like feeding, avoiding predators, energy conservation, etc. For example, the dorsal fin of the seahorse oscillate at frequencies up to 40 Hz, significantly higher than the frequency normally used for propulsion (less than 10 Hz), at the expense of its swimming efficiency. However, this feature makes it indistinguishable from the surrounding vegetation. Therefore, when considering designs and kinematics of marine animals, the importance of this non-locomotor factors and the relative impact on their performances have to be considered.

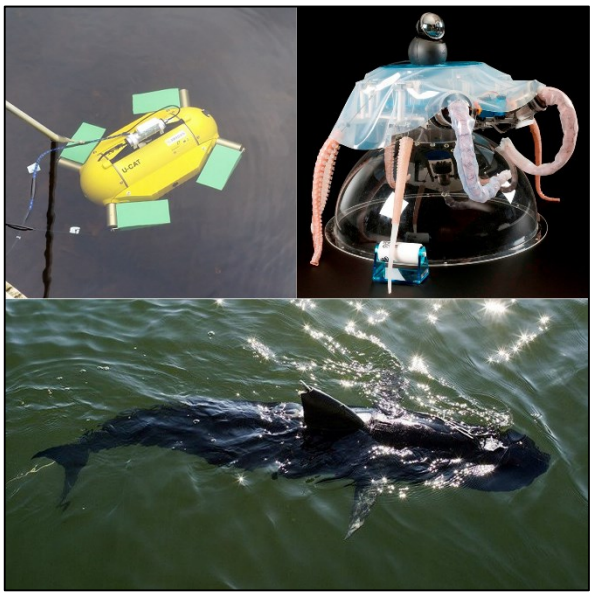

Figure 1.1: Biomimetic underwater robots. Upper left: U-Cat [9]; upper right: Octobot [10]; lower: Ghostswimmer [11].

1.2 Objective of the research

The aim to replace the conventional screw propellers traditionally employed on AUVs with more efficient bio-ispired thruster has guided the author of the present dissertation during his research. In the robotic literature, biomimetic underwater vehicles usually adopt a direct drive to actuate their undulating bodies, being those piecewise-flexible open-chain mechanisms or soft and compliant structures. Therefore, the use of servomotors is a common feature among robotic fish prototypes, although different driving systems like artificial muscles, hydraulic actuators and shape memory alloys have been tested in the last two decades. However, since servomotors are characterized by low mechanical efficiency, the first objective of the present

work has been the study and development of transmission mechanisms, suited to replace the aforementioned direct drive actuation with more efficient solutions where DC and brushless motors were integrated. Therefore, two transmission systems have been designed according to that requirement. Furthermore, the proposed solutions are characterized by a linear motion law for the drive, which in turn implies a constant velocity setting for the motor. On the other hand, the alternate-rotation motion law of servomotors requires non-linear position control, thus increasing the effort of the onboard electronics.

In order to test the worthiness of the proposed transmission system, it has been integrated in the propulsive compartment of two swimming robots composed by a rigid hull and propelled by the pendulum-like oscillation of a flat plate connected to the forebody through a revolute joint. Thus, the second aim of the present work has been to manufacture a working prototype. The necessary activities have been divided in two successive steps: first, a preliminary sizing of the robot and its propulsive system; then, a study on the realization of a solid and watertight structure that could be assembled using commercial components, machined parts as well as elements obtained through 3-D printing rapid prototyping techniques. The aformentioned fin motion law has been selected for its simplicity and because it matches the actual propulsion mechanism exhibited by a class of biological swimmers called *ostraciiforms*. Furthermore, harmonic oscillation coincides with the links relative motion law in a piecewise-flexible tail mechanism; thus, the transmission system proposed in the present dissertation is suited to be extended also to more complex – and more efficient as well – tail undulation mechanisms. In order to predict the value of thrust force necessary to move the vehicle and correspondingly select a motor, the propulsive performances of the oscillating thruster have been investigated by adopting a multiphysics approach: computational fluid dynamics and multi-body analysis have been successfully coupled to obtain a complete characterization of the vehicle dynamics and its propulsive systems. Moreover, the proposed method can be used to design biomimetic robots of different size, payload and mission, once a cruise condition and target velocity have been properly set.

Another objective has been the experimental validation of the numerical simulations: here, the main issue has been the impossibility to measure the actual forces acting on the physical prototypes as well as on the real biomimetic thruster separated by the robot forebody. Indeed, while the first option has been neglected due to onboard space limitations, the unavailability of a water flume of the necessary size has denied the second one. Hence, a scale model of the fin has been adopted, which in turn has required the design and manufacturing of a dedicated estensimetric force sensor, sized accordingly to the numerical predictions already performed. This device has thus allowed to obtain a complete characterization of the *ostraciifom* thruster, while validating the trends computed by the numerical analysis.

The final purpose of the research activity performed by the author of the present dissertation has regarded the investigation of the forces generated by a flapping foil in a freestream. This roto-traslation, which matches the fin motion law of the most efficient swimmers in nature, has requested a large number of numerical simulations in order to calculate the sensitility of the propulsive forces from the various fluid dynamic and kinematic parameters characterizing flapping motion. Once the required analysis have been performed, a transmission mechanism has been designed and prototyped in order to drive the flapper.

In summary, the research activity has been focused on the pursue of the maximum propulsive efficiency for a biomimetic thuster, obtained by optimizing the individual factors from which efficiency depends. Once a solution has been found to integrate a performing motor in the

tail section of the robot, a dedicated transmission system has been developed to generate the fin motion law exhibited by the most efficient swimmers in nature.

1.3 Outline of the dissertation

Being new to the field of biomimetics applied to autonomous underwater robots, the first part of the activities performed by the author have regarded the classification of the various swim modes of locomotion and the origin of the propulsive forces generated by the fluid-structure interactions between the fish undulating bodies and the surrounding water. Thus, an extensive review on the aforementioned subjects is presented in Chapter 2, toghether with a collection of the most rapresentative robotic fish manufactured in the last twenty years by engineers all around the world.
Chapter 3 opens with the computational fluid dynamics analysis performed on an oscillating flat plate shaped like a caudal fin. This type of motion perfectly matches those exhibited by a class of biological swimmers called *ostraciiforms*. The computed results has been exploited to desing a transmission mechanism suited to replace the inefficient servomotors commonly adopted on robotic fish prototypes, with a performing DC motor. In order to test the devised solution, it has been installed on two fully functional biomimetic vehicles, both presented in the third Chapter. The transmission mechanism has then been subjected to a dynamic analysis in order to estimate its mechanical efficiency and to a feasibility study as well in order to predict the internal volumes necessary to house the mechatronic systems.
Chapter 4 is entirely dedicated to the experimental tests performed to validate the numerical predictions presented in Chapter 3. While sections 4.1 and 4.2 motivate the choice of working on a scale model and provide an overview of the setup devised by the author, the central part of the Chapter is focused on the force sensor design and fabrication procedures, with a special attention on the strain gages configuration, installation and calibration, performed before the actual measurement took place. Prelimary examinations have been also scheduled in order to visualize the flow behind the oscillating foil, particularly the vortex structures inside its wake. The final part of the Chapter details the force measurements and discusses their results.
The multiphysics approach followed to couple the whole vehicle dynamics with the thruster characterization obtained by means of computational fluid dynamics techniques, is presented in Chapter 5. The regime swimming speed and the forebody oscillation amplitude have been computed at different motor angular velocities, while the obtained results allowed to compute the propulsive efficiency in the various navigation conditions. The whole modeling and simulation procedure has been also proposed as a novel sizing method for autonomous bio-inspired underwater vehicles.
In conclusion, in the sixth Chapter, the computational fluid dynamics analysis performed on a flapping foil are presented. A sensitivity analysis has been thus conducted to identify the relationship between the geometric and kinematic parameters characterizing the fin motion and its propulsive performances. Then, guided by the obtained results, a novel transmission mechanism has been designed to generate the necessaty roto-translating motion of the fin.
The conclusions on the presented topics and suggestions for the inherent future research are finally provided in Chapter 7.

Chapter 2.

Swimming robots

2.1. Introduction

The comparative biomechanics of bodies moving through water has attracted the attention of engineers for a long time and the last decades have witnessed considerable growth in the study of aquatic animals' locomotion. The attempts to design machines capable of propelling themselves like marine mammals and fish are inspired by the aim to exploit the best that nature has to offer to improve the capabilities of underwater vehicles in terms of both speed and manoeuvrability. However, it's worthy to remark that these principle does not necessary imply the construction of a robotic fish; that would be *mimicking* nature, which is different from *biomimesis*. The construction of a robotic fish could be still a necessity when the aim is to understand the fluid-mechanics of swimming, but in general, the aim is to apply marine animals locomotion principles to solve major design and control issues of underwater vehicles, like power-efficient cruising, trajectory tracking, manoeuvrability and so on. Still, in order to replicate successfully the swimming modes evolved by fish in thousands of years, biological systems must be deeply investigated and their features soundly understood.
To this aim, the following sections are meant to provide an extensive introduction on the topic, focusing on the current classification of fish modes of locomotion, with a particular focus on the *Body and Caudal Fin* swimming mechanics. Thrust generation is also described in terms of the momentum transfer mechanisms resulting from the fluid-structure interactions between the fish body and the sorrounding water. The following sections are also dedicated to the state of the art of biomemic underwater robots: details of their architecture as a function of the swimming modes they aim to replicate are also provided, together with a comparison between the performances exhibited by the manufactured prototypes and the expected results.

2.2. Fish swimming modes

The main features presented by water as a locomotion medium are incompressibility and high density. While the first allows any fish to move water during swimming, and vice versa, the second generates a buoyancy force that can counterbalance its weight. This has allowed the development of a great variety of swimming propulsions, as vertical support is not of primary importance. The forces acting on a swimming fish are displayed in Figure 2.1, where thrust and resistance forces act in the horizontal direction, while weight, buoyancy and hydrodynamic lift act in the vertical. According to the momentum conservation principle, a

fish swimming at constant velocity must generate enough thrust to balance the resistance it encounters while moving forward. Particularly, thrust can be generated by means of the following momentum transfer mechanism: drag, lift and acceleration reaction forces.

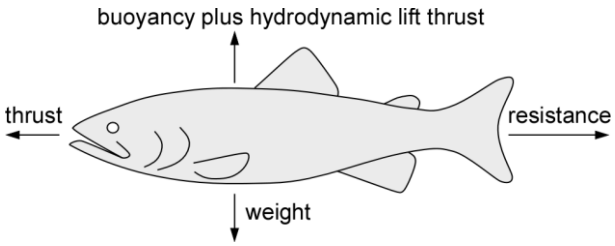

Figure 2.1: Forces acting on a swimming fish.

Swimming drag can be classified as skin friction and pressure drag: skin friction is due to the presence of large velocity gradients and is normally proportional to the fluid viscosity, at least for a large class of fluids called *Newtonian fuids*. Skin friction never contributes to thrust generation, since it acts as a resistance force only. Pressure drag is further classified as form drag, which originates from the flow distortions around solid bodies, and induced drag, which is due to lift generation. Lift forces originate whenever the pressure on one side of an object is greater than the opposite, resulting in a force perpendicular to the flow direction. Finally, acceleration reaction is the additional inertial force required, in unsteady motion, to accelerate the water close to a body; the equivalent mass of water, which must be effectively accelerated to account for this force is usually called virtual or added mass.
The contribution in terms of thrust generation which is due to drag, lift and added mass forces depends from the flow *Reynolds* number, a dimensionless parameter standing for the ratio of inertial over viscous forces and defined as:

$$Re = \frac{LU}{\nu} \tag{2.1}$$

where U is the swimming speed, L is a characteristic length (usually the lenght of a body, the span of a tail or the chord of a foil) and ν is the kinematic viscosity of water. For adult fish swimming, the *Reynolds* number varies between 10^3 and 10^5 [12]: in this range, lift, pressure drag and acceleration reaction forces contribute to thrust generation as shown in figure 2.2.

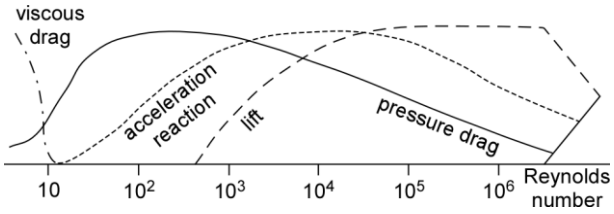

Figure 2.2: Magnitude of swimming forces as a function of the Reynolds number [12].

In order to understand the relationship between the swimming performances exhibited by fish and the aforementioned propulsive forces, it's necessary to introduce the nomenclature formerly presented by Breder [13] to classify the acquatic locomotion of marine animals and traditionally adopted by engineers working on the field of biomimetics. Figure 2.3 shows the terminology used in literature to describe the morphological features of fish: in *Body and/or Caudal Fin* (BCF) locomotion, the swimmer bends its body into a backward propulsive wave, which extends to its tail up to its caudal fin. A similar behavious is exhibited by *Median and Paired Fin* (MPF) swimmers, but the bending motion is confined to their median and paired fins. Both BCF and MPF locomotion mechanisms are further classified as *undulatory* and *oscillatory*, depending from the type of motion exhibited by the thrust-generating structure.

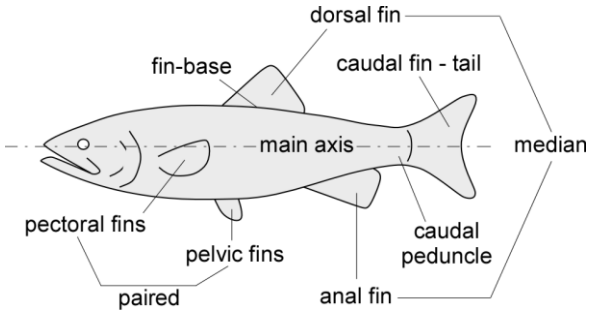

Figure 2.3: Morphological features of fish.

The optimum designs for fish morphology corresponding to a specialization for accelerating, cruising and manoeuvring have been identified by Webb in [14], as shown in Figure 2.4. Nevertheless, expertise in one of the aforementioned swimming condition does not exclude the possibility to use the others: indeed, many fish employ MPF locomotion for foraging and then switch to BFC thrust generation to cover long distances at constant speed.

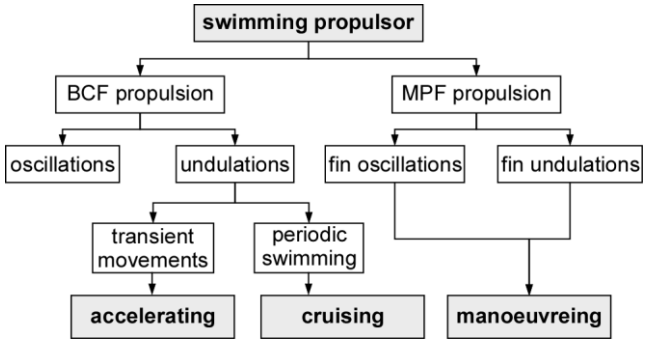

Figure 2.4: Relation between swimming locomotion and swimming functions [14].

The BCF *undulatory* thrust-generation mechanisms are further classified in four swimming modes identified by the terminology clarified in [13]. In *undulatory* BCF modes, a propulsive

wave propagates along the fish body in the opposite direction with respect to the swimming direction and at a greater speed compared to the overall forward velocity. Figure 2.5 shows the four *undulatory* BCF modes; the main differences among them are the amplitudes of the undulation wavelength, the fraction of the body bent by the passage of the wave itself and the thrust generating force type: particularly, *anguilliform*, *sub-carangiform* and *carangiform* modes are associated with the acceleration reaction forces (the added mass effect), while *thunniform* swimming is associated with lift (vorticity) forces.

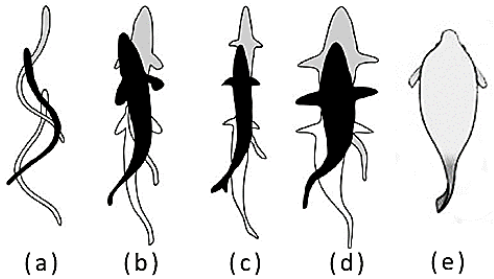

Figure 2.5: BCF swimming modes: (a) *anguilliform*, (b) *sub-carangiform*, (c) *carangiform*, (d) *thunniform*, (e) *ostraciiform* [13].

The fluid-structure interaction mechanism normally associated to the acceleration reaction forces can be briefly explained as follows, also using Figure 2.6: as the fish body is bent by the passage of the propulsive wave, each body segment (called *propulsive element*) transfers part of its momentum to the surrounding water. A reaction force F'_R, usually approximated as the product of the accelerated mass and its acceleration, is then exerted by the water on the propulsive element, in a direction normal to the latter. The forward, horizontal component of F'_R contributes to thrust generation, while the lateral component F'_L induces the fish body to sideslip and recoil, leading to significant energy losses. The accelerated mass is normally computed as the water density times the volume of a cylinder with diameter equal to the body segment cross-section.

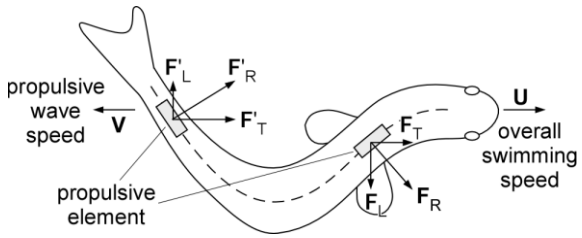

Figure 2.6: Added mass forces in BCF locomotion.

In *anguilliform* mode, the whole body of the fish is bent in large-amplitude undulations. Since at least a complete wavelength is always present along the fish body, the yawing moment is usually neglectible, along with any tendencies to recoil. The same feature allows *anguilliform*

swimmers (e.g. eel and lamprey) to move backward, inverting the direction of the propulsive wave. *Sub-carangiform* and *carangiform* swimmers employ a similar mechanism, but the percentage of the body involved in the undulation is considerably smaller: about half the length of the body for the former, the last third for the latter. *Carangiform* swimmers are generally faster than *sub-carangiform* and *anguilliform*, but this advantage comes at the expense of their turning and accelerating capability, compromised by the increased stiffness of their body. Moreover, since the reaction forces due to the added mass effect are distributed near the fish tail, the tendency to recoil is greater when compared to *anguilliform* locomotion; still, the following morphological adaptations allow fish to compensate this effect [15-16]: a reduced depth of their bodies near the anal peduncle and the concentration of the body depth and mass in the anterior part of the fish body. *Thunniform* locomotion represents the apex of swimming evolution in terms of efficiency: unlike the previous modes, thrust is generated by lift; specifically, more than 90% of the propulsive force comes from the caudal fin, while the rest is produced by the added mass effect associated to the lateral undulations of the area near the peduncle. This mechanism allows scombrinds like tunas, sharks and marine mammals, to maintain high cruising speeds for a long time. At the same time, the slender and streamlined body of *thunniform* swimmers minimizes the pressure drag they experience while moving forward, while the stiff and crescent-moon shaped caudal fin minimizes the induced drag due to lift generation [16]. Sections depth and body mass distribution are further optimized to compensate the power of the caudal thrust, effectively minimizing sideslip and recoil at the expense of manoeuvrability. *Ostraciiform* swimming mode is the only BCF *oscillatory* thrust generating mechanism; particularly, it consists of low-efficiency pendulum-like oscillations of the stiff caudal fin, while the rest of the body remains rigid.
A similar classification exists regarding MPF locomotion. As stated before, many fish swim using their pectoral fins and/or both their anal and dorsal fins. However, since the present work is focused on the swimming modes opimized for efficienct locomotion at high cruising speed for a long time, the author choose to limit this dissertation to BCF propulsion only, as predicted by the aforementioned analysis provided by Webb.

2.2.1 Wake structure and *Strouhal* number in BCF locomotion

The thrust-type structure of the wake behind the tail of a BCF swimming fish is composed by a staggered array of trailing vortices of alternating sign; the rotational direction of this vortices is the opposite of the one exhibited by vortices inside the drag-producing *Karman vortex street* wake, which propagates behind bluff objects for a specific range of the *Reynolds* number, as it is shown respectively in Figure 2.7 (b) and (a).
In fluid dynamics, the *Strouhal* number *St* is a dimensionless parameter used to characterize oscillating flow mechanisms; for a BCF swimmer, it is defined as:

$$St = \frac{fA}{U} \tag{2.2}$$

where f is the tail-beat frequency, A is the width of the wake as in Figure 2.7 (c), while U is the average swimming speed. Tryantafyllou *et al.* [17] observed that thrust development in oscillating foils is optimal for a specific range of St, namely $0.25 < St < 0.35$; data collected

from biologists for high-speed swimmers support this conclusion [18]. An interesting factor is that this feature does not belong only to the *thunniform* mode but also to *carangiform* and *sub-carangiform* modes for *Re* ranging between 10^4 and 10^6. This makes *St* the essential parameter when analysing BCF locomotion. Besides high thrust and efficiency, oscillating foils offer the possibility to recapture kinetic energy from an incoming wake: supporting this theory, tests conducted by Tryantafyllou *et al.* [6], [19] showed a reduction of the apparent drag of swimming by at least 50%. A 38% swimming drag reduction were obtained by Wen *et al* testing a robotic Saithe swimming at Re $3x10^5$ [20].

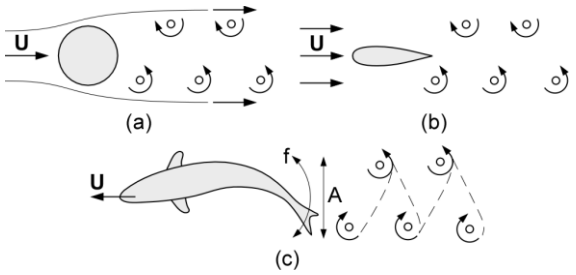

Figure 2.7: Wake structure: (a) bluff object, (b) thrust-generating foil. (c) Parameters of the *Strouhal* number.

2.3 A comparison between biological and robotic swimmers

Fish survival techniques and underwater vehicle design have much in common in terms of performances required; grounding on this evidence, the University of Southampton and the National Oceanographic Centre, UK, collected data regarding the equivalent capabilities of marine mammals, fish and AUVs, as part of a greater project called "Nature in Engineering for Monitoring the Ocean" (NEMO) [21]. Particularly, NEMO researchers created a database from the collected data about the performances of 73 different types of AUVs, investigating sources like manufacturers publications, journals and so on. The swimming performances in engineering terms were also collected for marine animals and the comparison between these data brings to the following considerations.

Marine animals are definitely faster than AUVs, both in terms of their absolute speed, which is velocity in meters per second, and in terms of relative speed, which is the ratio between speed and body length and thus expressed as Body Length per second (BL/s). Considering absolute speed, *thunniform* swimmers – marked with the number 1400 before the name of the marine animal – are far superior than AUVs, both in terms of their maximum swimming capability (corresponing to the highest value in the line representing their speed range in Figure 2.8) and also in terms of their optimum speed (the start of the aformentioned line), i.e. the speed of maximum autonomy. The dashed lines in the same figure represent the highest economic and maximum speed of all AUVs in the database. However, speaking in terms of relative speed, *sub-carangiform* and *carangiform* swimmers (marked respectively with 1200 and 1300) exhibit the highest maximum values, as it is shown in Figure 2.9, although their optimum speed is much lower (which is correct, since the highest swimming efficiency is

associated with *thunniform* locomotion, as it has already been stated). AUVs performances, indicated again by a dashed line, are still very low compared to marine animals.

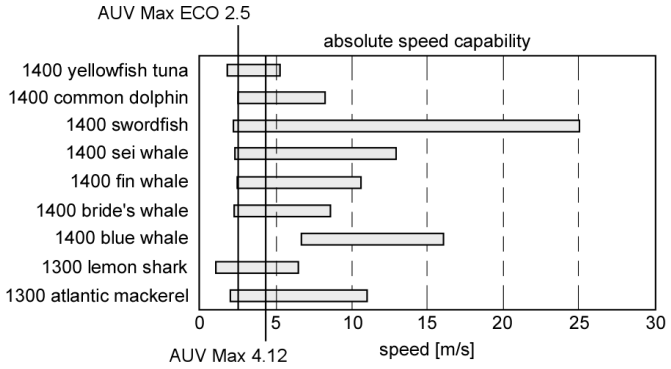

Figure 2.8: Absolute speed comparison between marine animals and AUVs [21].

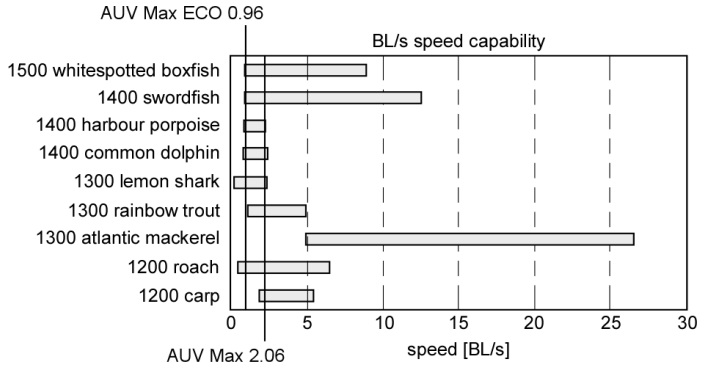

Figure 2.9: Relative speed comparison between marine animals and AUVs [21].

Manoeuvrability is measured as the normalized turning radius, expressed in BLs, necessary to reverse the direction of motion. The corresponding values for AUVs and marine animals in the database are shown in Figure 2.10: once more, the superiority of biological swimmers compared to propeller propulsion is obvious. Particularly, Figure 2.11 shows that the lowest values for the turning radius belong to fish possessing multi-joints flexible bodies (marked with a circle), while the high efficient, rigid-body *thunniform* swimmers (marked with a plus) such as tunas, exhibit much larger values.
Swimming efficiency and autonomy can be expressed in terms of Cost of Transport (COT) and energy storage capability, which relates to endurance. The COT parameter quantifies the energy expenditure required to swim at a given speed and it is expressed as follows

$$COT = \frac{Energy}{Mass * Distance} \tag{2.3}$$

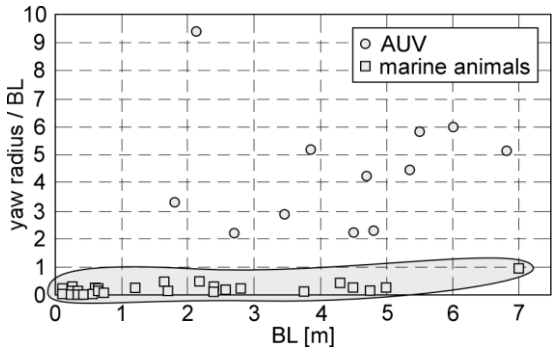

Figure 2.10: Turning radius per unit length of AUVs and marine animals [21].

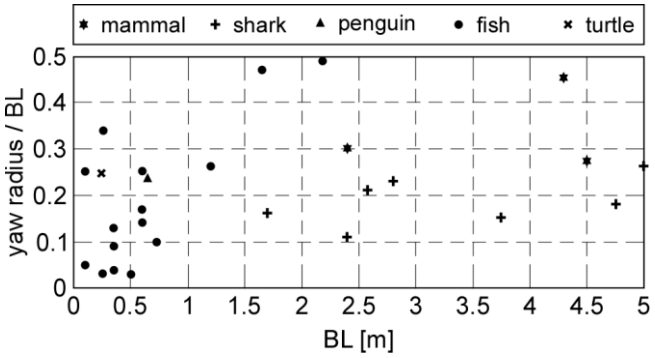

Figure 2.11: Turning radius for marine animals; Circle=Fish, Plus=Shark, Star=Mammal, Cross=Turtle; Triangle=Penguin [21].

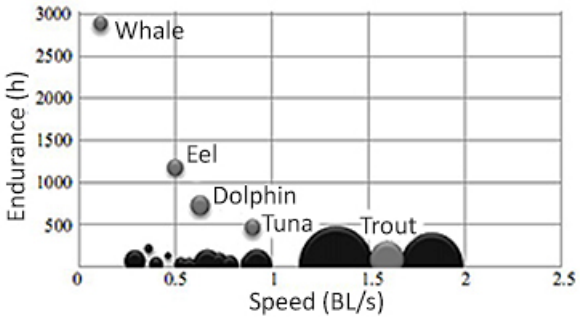

Figure 2.12: COT and endurance of marine animals (light circle) and AUVs (dark circle) [21].

Figure 2.12 shows the endurance of several marine animals, expressed in hours, compared with the power reserve of an AUV; furthermore, the size of the circle is an indication of the

COT value. The graph shows a significant higher endurance and lower COT within marine animals compared to AUVs.

2.4 Mathemathical models for fish locomotion

The production of a performing AUV propelled by biological locomotion principles, requires the development of a mathematical model, which accurately describes the kinematics of the swimming mode adopted to generate the necessary propulsive forces. One of the most successful mathematical models, widely used to design biomimetic robots, is Lighthill's elongated-body theory [22], which is best suited to *anguilliform* and *sub-carangiform* swimming modes. The original theory was lately extended by Lighthill [23] to account for large lateral motion of the undulating body, better suiting to *carangiform* swimming. However, both theories agree in one prominent factor: the mean thrust can be estimated by the trailing edge kinematics of the tail. Lighthill's theories states that the bending motion of the tail of a fish, swimming according to one of the aforementioned modes, can be described using the Travelling Wave (TW) function:

$$y_{TW} = (c_1 x + c_2 x^2)\sin(kx + \omega t) \tag{2.4}$$

where y is the lateral displacement, $k=2\pi/\lambda$ is the wave number and $\omega=2\pi f$ is the undulating pulse, as shown in Figure 2.13.

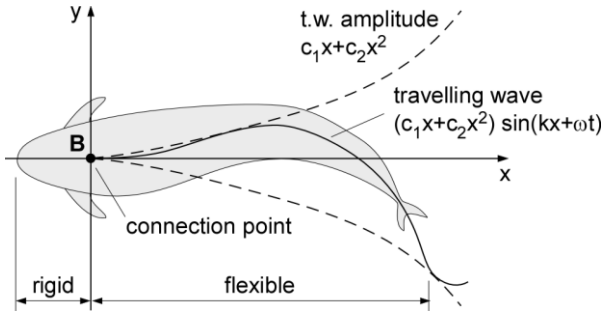

Figure 2.13: Travelling Wave function in fish locomotion.

Elongated-body theory cannot be applied to *thunniform* locomotion because the shape of the caudal fin violates the fundamental assumption of slenderness. Therefore, theories developed for *thunniform* swimming consider the tail as an oscillating (flapping) foil independent from the rest of the body. Mean propulsive efficiencies as high as 91% have been reported for the Robo-Tuna [24], a *thunniform*-swimming biomimetic robot manufactured as an actual tuna at MIT in 1995. Actually, the Tuna adopted a fairly different kinematics compared to the one exhibited by scombrids: particularly, the oscillating foil behaved like the tail of a real tuna, but the undulation of the flexible body was characterized by a larger amplitude, more suited to *carangiform* swimming. However, the results shown by the Tuna spawned much of the work in the years to come [25], [26].

The performances of a *thunniform* swimmer depend on the properties of its tail: geometrically speaking, the stiff caudal fin is shaped like a tapered hydrofoil, with a moderate sweepback angle, a curved leading edge and a sharp trailing edge; from a kinematic point of view, it behaves like a pitching and heaving body (also known as *flapper*) tracing an oscillating path behind the fish while this moves forward; this is shown in Figure 2.14.

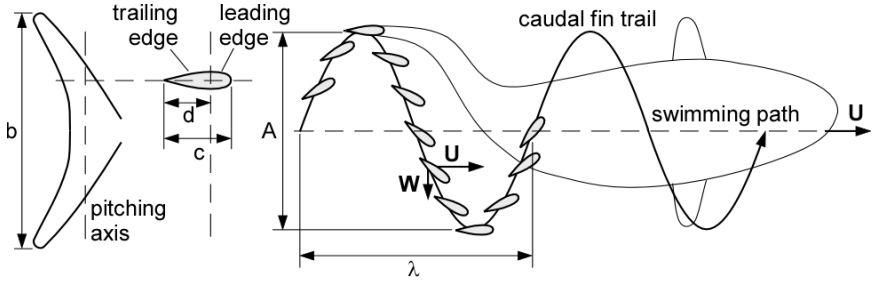

Figure 2.14: Geometric and kinematic features of thunniform swimming.

The models presented so far assume a rigid tail: research has also been conducted on the elastic properties of the caudal fin [27]. Far more promising is the manner in which fish make use of passive mechanical properties, most notably elastic, to enhance the effectiveness of their muscles: Harper et al. computed a 33% reduction in energy cost for heaving motion when driving a hydrofoil via a properly tuned series stiffness [28]. Springs may be also used for energy storage, shock absorption, catapulting and more important, acting as muscle antagonist: for example, the skin of a lemon shark behaves like a non-linear spring working in parallel with the musculature; as the shark body is flexed from side to side, the outside muscle may get stretched to a point where they are ineffective at generating force. On the contrary, the springs are highly stretched and may contribute to accelerate unbending.

2.5 Mechanics of bio-inspired underwater robots

The following section presents some biomimetic underwater robots, showing the mechanical solutions employed to exploit fish propulsion mechanisms. The focus, as stated before, is on BCF swimming modes.
In 1994, [29] MIT produced the famous RoboTuna, a 49-inch *thunniform* swimmer propelled by an eight-link mechanism, driven by six brushless motors mounted outside the fish and an assembly of pulleys and strings; the robot was suspended in a water tank by means of a mast. The major structural components were a segmented backbone made up of eight discrete rigid vertebra, a composite-manufactured lunate tail and a flexible steel spline element on which the ribs were mounted to sustain the outer skin during swimming (much like the real fish ribs do). The skin, representing the outmost part of the hull, consisted of a thin layer of flexible, reticulated foam covered by a Lycra sock, Figure 2.15.
At the same time, Hirata [30] developed a three-joint fish robot driven by three servomotors. Figure 2.16 shows the architecture of the vehicle and its unique mechanism designed for the tail. Two different caudal fins were installed on its aft: a pike-type, with plane cross-sections,

and also a tuna-type, with a streamlined cross-section similar to an airfoil. The highest speed obtained during the tests was 0.7 BL/s, a result achieved with a 90 degrees phase difference between the translation motion of the tail peduncle and the rotation of the tuna-type fin, just as predicted by airfoil theory. A few years later, Draper Laboratory produced the Vorticity Control Unmanned Undersea Vehicle [31], a fully autonomous *thunniform* swimmer driven by hydraulic actuators.

Figure 2.15: MIT RoboTuna [29].

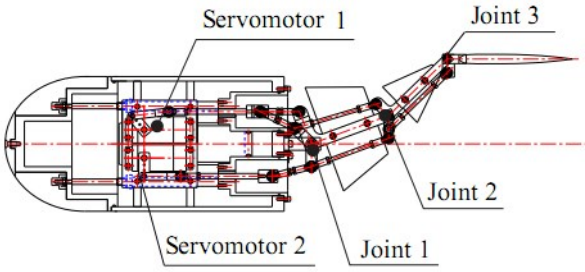

Figure 2.16: Hirata RoboPike [30].

In those years , Fukuda [32] developed a novel class of biomimetic fish using Ionic Polymer-Metal Composites (IPMCs), a type of actuation materials particularly suited to swimming microbots designed for pipe inspection, defence and blood vessel microsurgery. Indeed, IPMC is physically light and flexible, uses a low driving voltage (less than 3 V) and operates well underwater. Nafion 117 was the IPMC chosen to drive a pair of tail fins to generate the

necessary thrust, as well as to adjust the buoyancy of the robot using a strip of IPMC attached under its bow section, as shown in Figure 2.17. The microbot measured only 45 mm in length, 15 mm without the tail. Following Fukuda's work, Kim *et al.* [33] designed a 96-mm-long robotic tadpole using a previously developed casting method to control the thickness of the ion-exchange polymer films selected as the actuation material for the tail. Later, Tan *et al.* [34] and Ye *et al* [35] used IPMCs for a series of robotic fish.

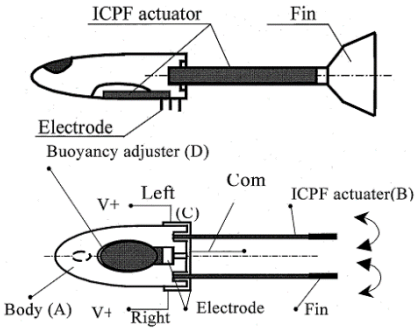

Figure 2.17: IPMC microbot scheme [32].

In the mid 2000s, Yu *et al.* [36-39] designed a series of multi-link, biomimetic robotic fish propelled by *carangiform* locomotion, whose configuration is displayed in Figure 2.18; the submerging and ascending control was realized by changing the angle of attack of the pectoral fin mechanism. A robotic fish capable of three-dimensional locomotion was also designed by Zhang *et al.* in 2007 [40]. R/C servomotors were used to actuate the four-link mechanism of the flexible tail and lunate fin. Two more servomotors were employed to drive a pair of pectoral fins through a mechanical gear, in order to realize up-and-down motion. A similar configuration was adopted by Wang [41] to design a three-link hybrid BCF-MPF robotic swimmer.

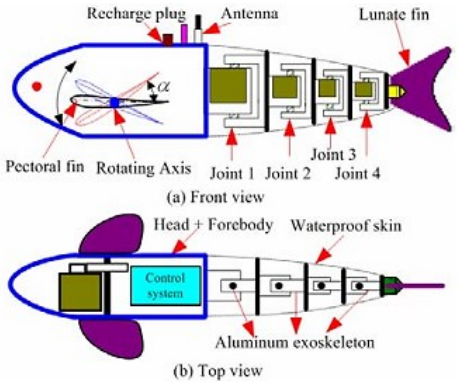

Figure 2.18: Robotic fish propelled by *carangiform* locomotion [36-39].

In 2008 [42], the University of Victoria adopted a Shape Memory Alloy (SMA) based design for the actuation of the flexible tail; a similar solution had already been proposed by Texas A&M University [43]. In order to mimic the *carangiform* mode of locomotion, a skeletal structure was developed: its basic element was a spline running from the bulkhead section to the tail peduncle, while fiberglass ribs were attached to the spline to provide the 3D shape of the tail. The entire aft section was flooded in order to avoid the problem of sealing it. Neoprene was the material chosen for the skin, stretched over the skeleton structure. Nitinol wires SMA were employed for actuation: the one-way shape memory effect occurred after an external force strained the material in its cold state; then, upon heating, the material would have returned to the initial "remembered" state, Figure 2.19 (upper). The overall level of performance was not satisfactory, particularly in terms of thrust generated by SMA, which required too much power to be useful in AUVs design, a proof that convinced the engineers to produce a second prototype, a Servo-Tuna, employing four servomotors to actuate a four-link serial tail, Figure 2.19 (lower).

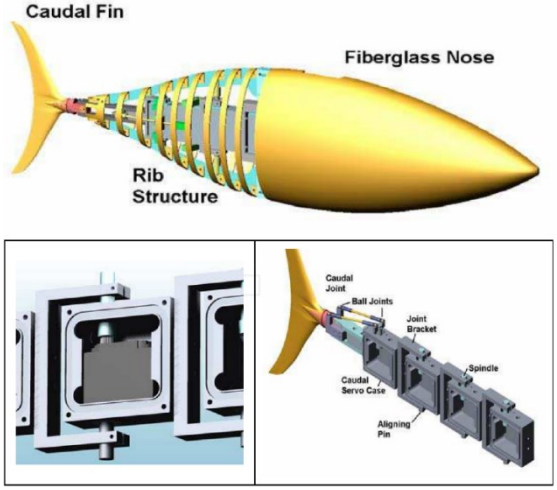

Figure 2.19: SMA-design Tuna (upper) and Servo-Tuna (lower) [42].

One year later, Alvarado tested the swimming performances of the first compliant fish-like robot [44]. A similar design was also used by Stefanini *et al.* (2012) [45]. Unlike the previous models, where the tail undulation is achieved by means of a serial kinematic chain consisting of rotational joints and rigid links driven by servomotors, compliant robotic fish possess a soft and passive tail and a single motor, in order to facilitate the interaction with the flow. Therefore, according to vibration theory, the compliant body bending deformation depends from its actuation (the aforementioned motor, installed near the joint section between the rigid forebody and the flexible tail) and its natural frequencies. Therefore, in order to comply with Lighthill's Travelling Wave expression (2.4), the distribution of internal mass, damping and stiffness inside the compliant tail must be properly chosen.
The method used in [44] to model the soft, nonhomogeneus body was extended by Kruusmaa at Tallin University since 2009, to build the first robotic fish capable to extract informations

from the incoming flow [46]. Flow sensing (also called “Svenning” in honor of the Svennish biologist Sven Dijkgraaf), is involved in a great variety of fish behaviors: for example, it is used to navigate with respect to the flow direction, to orient themself towards the current in order to detect odors and food or even in detecting the wake of a swimming prey. Figure 2.20 shows the FILOSE (Fish Locomotion and Sensing) project robotic fish: here, the sensing unit consists of 16 pressure sensors mounted on the rigid head of the vehicle. Tests conducted by the authors showed that flow informations can be extracted by the proposed sensing system and exploited for a variety of purposes: for example, the wakes of objects could be identified and used for map building and localization. Furthermore, flow sensing coupled with a soft tail could be used to identify Karman Vortex Streets and other flow conditions where vehicle control is more stable and energy efficient.
The compliant body feature adopted in [44-46] has been modified in the last year by Zhong [47] at University of Hong Kong: here, the design innovation consists in the combination of an active wire-driven body actuated by a single servomotor, with a soft compliant tail in order to accomplish undulatory swimming, Figure 2.21.

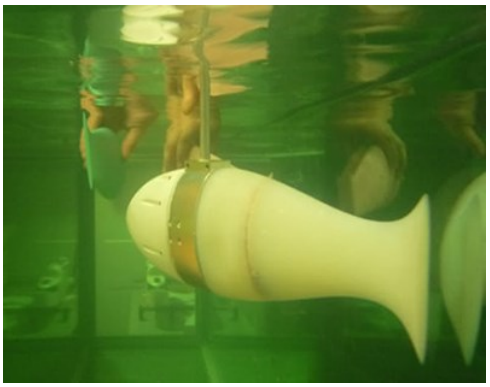

Figure 2.20: FILOSE project robotic fish [46].

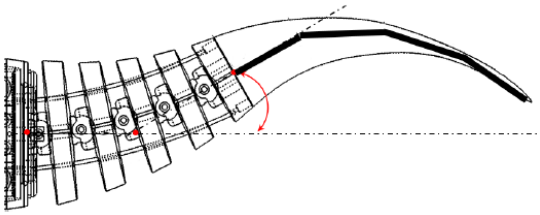

Figure 2.21: Wire-driven body and soft tail [47].

In 2010, Liu *et al*. designed the 52 cm long G9 *carangiform* swimmer at University of Essex. [48-49]. Here, tail undulation is achieved by means of a four link serial mechanism actuated by four servomotors. Two further DC motors are employed in the fixed, anterior part of the hull: the first is used to adjust the centre of gravity of the vehicle, while the second controls

a micro pump in order to regulate the weight of the robot by pumping water inside a ballast tank, Figure 2.22. The G9 was the first robotic fish where the rigid forebody rotation due to recoil effect was taken into account in order to compute the actual displacements of the tail segments. A three-link serial chain mechanism actuated by servomotors was adopted also to drive the tail of the Japanese, Ryomei Engineering KOI Carp Fish robot, [50-51], a 31 inches long, *carangiform* swimmer. The same architecture was adopted by Korkmaz *et al.* [52] to manufacure a *carangiform* swimming robotic fish propelled by a four-link serial tail actuated by servomotors.

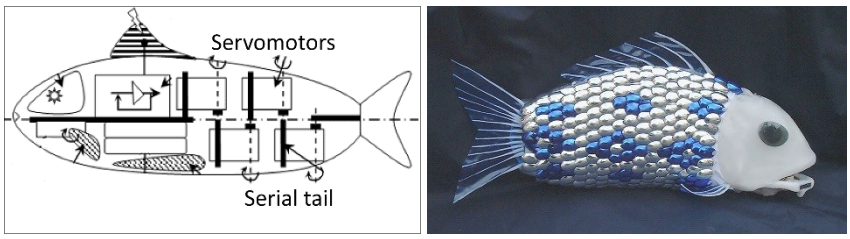

Figure 2.22: G9 Robotic fish. (a) schematics, (b) prototype [48-49].

Finally, in 2015 Marchese *et al.* manufactured at MIT the first soft robotic fish driven by an array of Fluidic Elastomer Actuators (FEAs), which constite the key mechanical innovation of the project [53]. The robot is designed to emulate escape responses in addition to forward swimming because such maneuvers require rapid body accelerations and continuum body motion. Therefore, soft robotics systems offered the potential to lift the limitations imposed by rigid-body kinematics, as their bodies can deform continuously when actuated. Moreover, fluid energy can be stored and subsequently released directly into soft actuators without a costly energy conversion stage. These features make soft robots well-suited to emulate the kinematics and dexterity displayed by some natural systems. However, since the motion of a soft robot is much harder to predict when compared to a multibody system, there is still much work to be done, particularly in terms of kinematic and dynamic modelling, device design, manufacturing process and control algorithms, in order to address the technical challenges of soft robotics systems, Figure 2.23.

Figure 2.23: MIT soft robotic fish drive by Fluid Elastomer Actuators [53].

2.5.1 Review of robotic fish architectures

According to the state of the art detailed in the previous section, three alternative ways to design a robotic fish can be identified.
The "oscillating plate" design, Figure 2.24 (a), consists of a rigid hull and an oscillating plate connected to the forebody through a revolute joint. Just like an *ostraciiform* swimmer, it has a low propulsive efficiency; nevertheless, the architecture is simple, inexpensive and its rigid body makes it is much simpler to waterproof and capable of withstanding greater depths. The robot manufactured by Kodati in 2008 [54] is an example of this style.
The "travelling wave" design method displayed in Figure 2.24 (b), aims to produce a smooth and continuously flexible hull. Thrust is produced by the undulatory motion travelling along the whole body with an amplitude that increases backwards as stated by expression (2.4). This style allows the design of extremely small robots [32-35] and compliant robots such as those in [44-47] and [53].
The "flapping wing" design, Figure 2.24 (c), consists of an anterior rigid head and a piecewise flexible tail driven by an N-joint serial mechanism. Expression (2.4) is then respected in a finite number of points only and different methods exist to optimize the relative length of the links. The robots in [29-31], [36-43] and [48-52] are examples of this style.
Although biomimetic robots with finite and infinite degree-of-freedom (DOF) bodies and electro-mechanical actuators show promising capabilities, they still cannot match the speed and dexterity of their natural counterparts. For instance, the popular G9 robotic fish achieved a linear speed equal to 1.02 body length per second, while the target value was 2.00 BL/s. Although the kinematic chain of the serial tail was designed according to a novel optimization technique [48-49], actuation still remains a critical issue of the project, as it will be shown in the next Chapter.

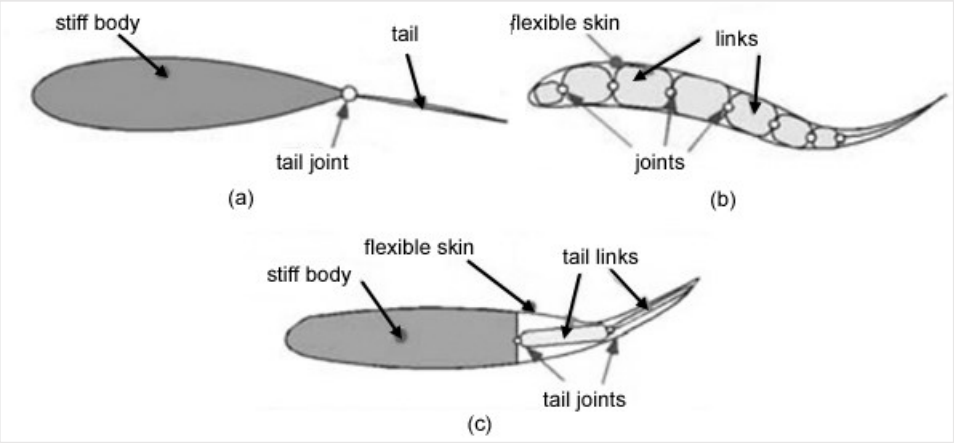

Figure 2.24: Robotic fish alternative design: (a) oscillating plate, (b) travelling wave, (c) flapping wing.

Chapter 3.

Design of an *ostraciiform* swimming robot

3.1. Introduction

The aim to achieve the highest possible propulsive efficiency in order to maximize the autonomy of a bio-ispired AUV has driven the author of this work to focus on *thunniform* locomotion. Then, since more than 90% of the propulsive thrust comes from the lift force generated by the flapping motion of the caudal fin, as stated in Section 2.1, the "flapping wing" design method seems a promising architecture for a *thunniform* swimming robot. Furthermore, the adoption of a multi-body tail structure composed by a series of rigid links and an equally stiff caudal fin, allows to predict the propulsive forces due to the fluid-body interaction without taking the tail deformability into account, contrary to what would happen with a soft robot and a "travelling wave" architecture. Particularly, the aforementioned design choice allows to predict the propulsive performances of the biomimetic thruster (the fin) by means of simulation techniques, where the finite elements-coupled fluid dynamics problem with a dynamic mesh boundary condition is replaced by a simple roto-translation of the mesh reference frame. Therefore, the computational cost of the numerical predictions is acceptable, about 24-36 hours each, and a large campaign of analysis can be effectively conducted in reasonable times.
In [50], Liu *et al.* demonstrated that, in order to comply with the required roto-translatory motion of the caudal fin, each link of a N-joint serial tail mechanism must oscillate following a harmonic motion law such as:

$$q_i = a_i \sin(2\pi f t + \Delta_i) \tag{3.1}$$

where q_i is the link angular position, a_i is the oscillation amplitude, f is its frequency – which is the same for each link – and Δ_i is the constant phase difference between the links harmonic functions of motion. As shown in Section 2.5, each link of the kinematic chain is actuated by a dedicated servomotor: then position control is required to comply with a non-linear motion law and to synchronize the servomotors in order to maintain the constant angular difference between the links. In [44], Alvarado measured the efficiency of the servomotor embedded in his soft robotic fish prototypes, reporting a peak of 0.55% at 2 Hz rotation frequency. Indeed, servomotors are not designed to be operated with continuous direction changes because the armature inductance heats up quickly and power is lost through heat even if they have coreless DC motors. Further issues may arise since each servomotor in the serial tail must be properly sealed, leading to an increase of the structure inertia and encumbrance.

In order to overcome these difficulties, the first objective of the present work is to replace the servomotors traditionally employed in the serial chains of *thunniform* swimming robots, with more efficient actuators like DC brushed or brushless motors. Then, in order to achieve this result, the author has designed a transmission mechanism capable to convert the continuous rotation, at constant angular speed, of the drive in the harmonic oscillation of the system output shaft. In this way, the effort of the control device is reduced, being sufficient a linear, constant velocity setting for the motor. Moreover, by means of this solution, the actuator can be properly chosen by ensuring that its rotation speed in the sizing condition (i.e. cruising at high speed), always remains inside the continuos operation zone and close to the peak efficiency value. This would be impossible with a direct drive (i.e. a servomotor) because of the continuos variations of the motor angular velocity inside an oscillation cycle. Finally, the proposed solution may represent a basic module that can be used to realize more complex bio-inspired propulsion systems driven by a single actuator, as it will be shown in the final Chapter of the present dissertation.
In order to test the wothiness of the devised solution, an *ostraciiform* swimming robot has been manufactured by the author, using the developed transmission to actuate the fish caudal fin. In fact, as stated in Section 2.5.1, this type of bio-inspired vehicle consists of a rigid hull and an oscillating plate connected to the forebody through a revolute joint. The optimal law of motion for the fin, in terms of frequency and amplitude, has been numerically predicted by using computational fluid dynamics techniques and the results used in the synthesis of the transmission system. The rest of the Chapter is also dedicated to the optimization of the actuation system and to the robot design and manufacturing. The employed techniques, the methods and the experience achieved by studying an *ostraciiform* swimming vehicle helped to identify the most important features of fish locomotion and the conclusions have been later extended also the more complex *thunniform* propulsion.

3.2 Computational fluid dynamics analysis of an oscillating fin

Computational fluid dynamics analysis represents an invaluable tool to assess the propulsive performances of bio-inspired thrusters. In the present work, the numerical simulations have been performed using an in-house developed research code named MIGALE. This code is based on the Discontinuous Galerkin (DG) space discretization and shares the same framework with a family of codes developed over the recent years to solve the compressible [55] and incompressible [56] Navier-Stokes and Reynolds-Averaged Navier Stokes (RANS) equations [57-58]. DG methods are variational methods which combine features proper of the finite elements - such as the element-wise polynomial representation of the solution - and of the finite volumes as well, like the computation of the numerical fluxes at the mesh element interfaces. The advantage of using such methods is related to the compact stencil of the space discretization, which is independent from the order of the polynomial approximation employed, as the solution is not required to be continuous at mesh elements interfaces. This fact makes DG methods to be very well suited for the implementation of high-order, implicit time-integration schemes, as well as adaptation strategies. Moreover, DG can provide very accurate solutions on curved and possibly hybrid computational grids. Since their accuracy is almost unaffected by the domain complexity and the quality of the mesh elements, they can be considered also for the simulation of industrial configurations.

In this work, the author has employed the two-dimensional and incompressible version of the DG code, suitably extended to deal with a moving reference frame [59] to account for the fin oscillation: as stated before, this technique has replaced a dynamic mesh boundary condition with a moving refence frame condition, thus reducing computational time. Moreover, in order to fulfill the incompressibility constraint, the artificial compressibility flux approach for the space discretization of the convective numerical fluxes has been adopted, while the second form of the Bassy-Rebay scheme (BR2) [60] has been used to deal with the viscous terms. The RANS equations have been closed using a Spalart-Allmaras turbulence model [58] and the governing equations have been discretized in time using a third-order, three-stages, Linearly Implicit Rosenbrock-type Runge-Kutta scheme. Linear solvers, preconditioners, distributed arrays and communication among them have been handled through the PETSc library [61]. The computational grid has been assembled using 3001 mesh elements, suitably curved to represent the leading edge, and fourth order polynomials have been employed to represent the solution within each element, resulting in a fifth order accurate space discretization. The time step size has been chosen according to the oscillation frequency of the fin to ensure the results to be independent from the time discretization. More details on the performed numerical analysis are provided in [62].
Figure 3.1 shows the propulsive efficiency and the average thrust coefficient as a funcion of the fin oscillation amplitude. In swim mechanics, the former is known as *Froude* efficiency and is defined as:

$$\eta = \frac{\langle T \rangle U}{\langle P \rangle} \tag{3.2}$$

where $<T>$ is the time-averaged thrust produced, $<P>$ is the average power required and U is the mean forward velocity of the fish. It results that both maximum values correspond to an oscillation angle equal to 14°, as confirmed by the *ostraciiform* swimming robot designed by Triantafyllou *et al.* in 2003 [63].

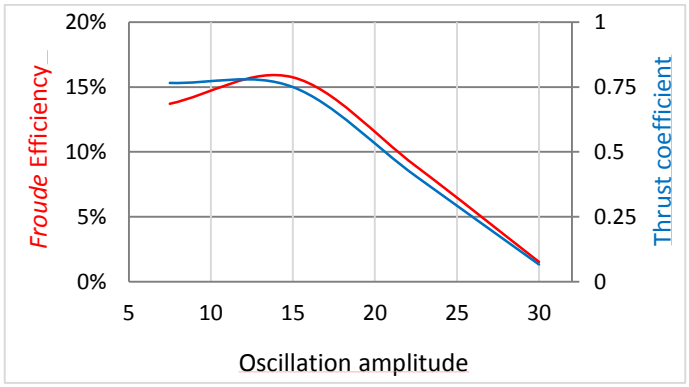

Figure 3.1: *Froude* efficiency and thrust coefficient as a function of the fin oscillation amplitude predicted by CFD analysis at *St* =0.5 [62].

Figure 3.2 shows the same quantities of Figure 3.1, displayed as a function of the *Strouhal* number. This dimensionless parameter has already been introduced in Section 2.2.1 by means of expression (2.2), which, for *ostraciiform* locomotion, further specializes in:

$$St = \frac{fA}{U} = \frac{f}{U} 2B \sin\theta_0 \tag{3.3}$$

where B is the fin chord (i.e. its length) and θ_0 is the oscillation amplitude.

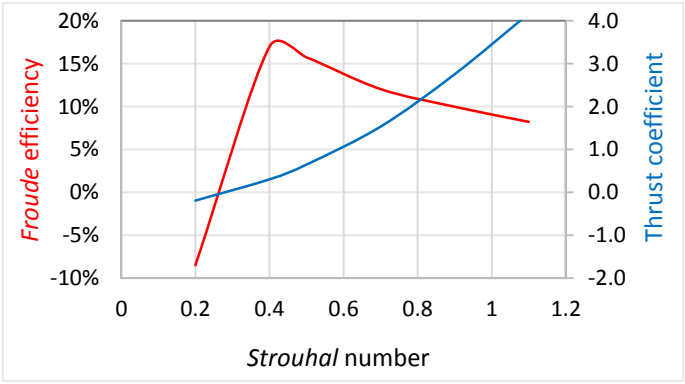

Figure 3.2: *Froude* efficiency and thrust coefficient as a function of the Strouhal number predicted by CFD analysis with the fin oscillation amplitude fixed at 14° [62].

The red curve displayed in Figure 3.2 shows that the efficiency η is negative when *St* is lower than 0.25, meaning that the oscillating fin is generating a negative thrust. As *St* grows, the efficiency rises up to a maximum equal to 17%, which corresponds to a 0.42 value of *St*. Experimental data collected on various swimming animals confirm the last result [18]. Then η decreases again as the fin oscillation frequency continues to grow. Indeed, despite the propulsive thrust is still rising, an increase of the separate flow region occurring at the fin leading edge causes it to grow slower than the transversal force component, generating a drop in the propulsive efficiency. This evidence, which is shown in Figure 3.3, is ascribed to the increasing of the separation bubble close to leading edge.

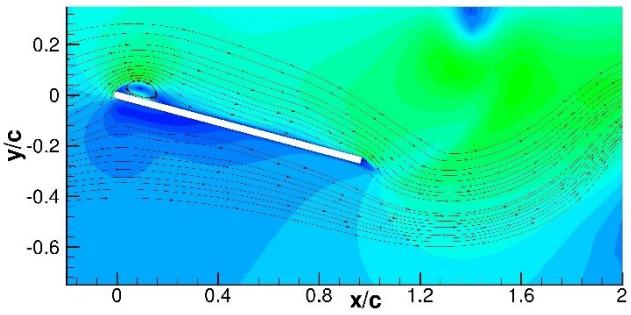

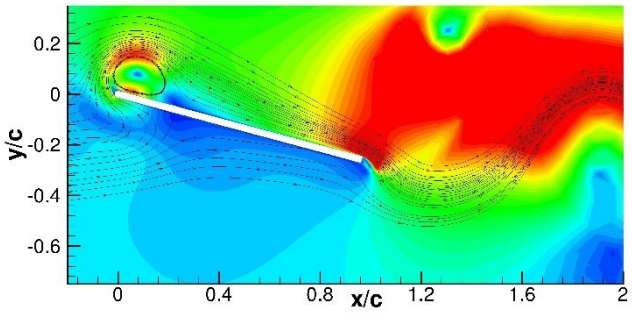

Figure 3.3: Flow visualizations at *St* 0.4 (top) and *St* 1.1 (bottom). Field coloured by velocity magnitude contours [62].

3.3 Transmission mechanisms for *ostraciiform* locomotion

The fin law of motion for ostraciiform locomotion is expressed by [64]:

$$\theta = \theta_0 \cos(2\pi f t) \tag{3.4}$$

where the oscillation amplitude θ_0 has been set equal to 14° according to the performed CFD analysis. The same quick consideration cannot be done about the oscillation frequency: in fact, expression (3.3) shows that the Strouhal number also depends from the robot swimming velocity U, so the whole vehicle dynamics must be taken into account. Particularly, it will be shown in Chapter 5 that each value of f corresponds to an average swimming speed, U, and therefore to a *Struohal* number value. Thus, the oscillation frequency can be properly set in order to match a particular navigation condition such as the maximum efficiency condition showed in Figure 3.2 as a function of *St*. However, for now it will be assumed that f belongs to the range [1-2] Hz, which is reasonable for an *ostraciiform* robotic fish swimming at the cruising speed of about 0.5 BL/s. Indeed, these values correspond to a *Strouhal* number close enough to the maximum efficiency value of 0.42.
Two different solutions have been designed to convert the continuous rotation, at constant angular speed, of the drive into an harmonic oscillation. The first mechanical system able to generate a motion law much similar to expression (3.4) is the Scotch-Yoke mechanism described in the following Subsection. The second transmission, which exactly replies the fin motion obtained with the Scotch-Yoke mechanism, is based on a spatial cam kinematic joint and will be detailed in Subsection 3.3.2. Both solutions reasonably approximate expression (3.4), so the final choice between one system or the other will be based on dynamic and manufacturing arguments, as shown in Subsection 3.3.3.

3.3.1 Scotch-Yoke transmission system

Figure 3.4 shows a kinematic scheme of the transmission system based on the Scotch-Yoke mechanism. It results easy to demonstrate that the provided solution transforms the input rotation angle of the motor, φ, in the harmonic oscillation of the output member, characterized

by the angle θ, which is fixed to the caudal fin. With reference to the geometric parameter in Figure 3.4:

$$h\cos\varphi = L\tan\theta \tag{3.5}$$

Output angle θ and the motor rotation φ are then related by the expression:

$$\tan\theta = \frac{h}{L}\cos\varphi \tag{3.6}$$

Expression (3.6) leads to the following velocity law:

$$\begin{aligned} \dot{\theta} &= -\left(\frac{hL\sin\varphi}{L^2 + h^2\cos^2\varphi}\right)\omega \\ \dot{\varphi} &= \omega \end{aligned} \tag{3.7}$$

Expression (3.6) slightly differs from the motion law (3.4), being the angle θ the argument of a tangent function; nevertheless, it results easy to demonstrate that equation (3.6) can be approximated to a pure sinusoidal function if

$$\frac{h}{L} = \tan\theta_0 \ll 1 \tag{3.8}$$

Since for θ_0 equal to 14° the ratio h/L is about 0.25, then the approximation is reasonable and the following simplified kinematic laws can be considered:

$$\begin{aligned} \theta &= \frac{h}{L}\cos\varphi \\ \dot{\theta} &= -\left(\frac{h}{L}\sin\varphi\right)\omega \\ \ddot{\theta} &= -\left[\left(\frac{h}{L}\sin\varphi\right)\dot{\omega} + \left(\frac{h}{L}\cos\varphi\right)\omega^2\right] \end{aligned} \tag{3.9}$$

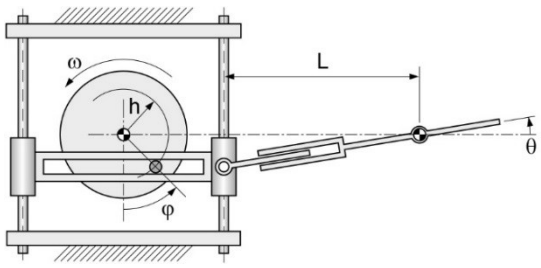

Figure 3.4: Scotch-Yoke transmission mechanism.

3.3.2 Spatial-cam kinematic joint

The second mechanism, which exactly replies the fin motion obtained with the Scotch-Yoke mechanism, is based on a spatial cam kinematic joint. This device is known in literature [65] but, to the best of the author's knowledge, it was never adopted to actuate the caudal fin of a bio-inspired underwater robot. The original assembly taken from [65] is shown in Figure 3.5. Here, the driving arm A has a drive-pin B which engages in a semicircular groove in a driven member C. This driven member is permitted to pivot freely on a pin D which is retained at each end is a support block E.

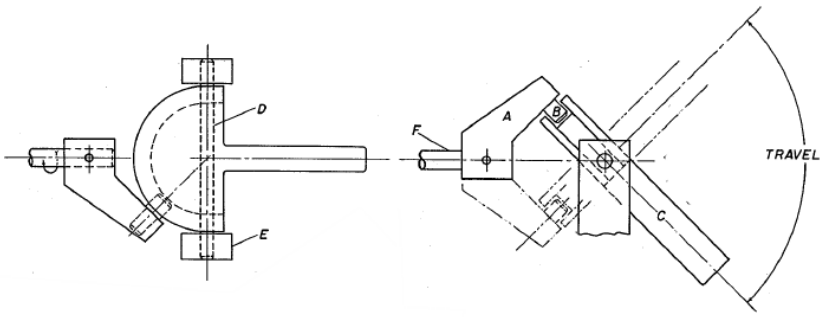

Figure 3.5: Kinematic scheme of the spatial-cam joint in [65].

The critical issue of the system displayed in Figure 3.5 in that the axis of pin D must intersect the axis of the drive shaft F and the axis of drive-pin B at a common point. Furthermore, the oscillation amplitude of driven member C is equal to the angle at which the drive-pin B intersects the axis of rotation of arm A: thus, in order to change the aforementioned amplitude value, it is necessary to disassemble the whole mechanism and replace driving arm A and pin B with new components having the desired geometry.

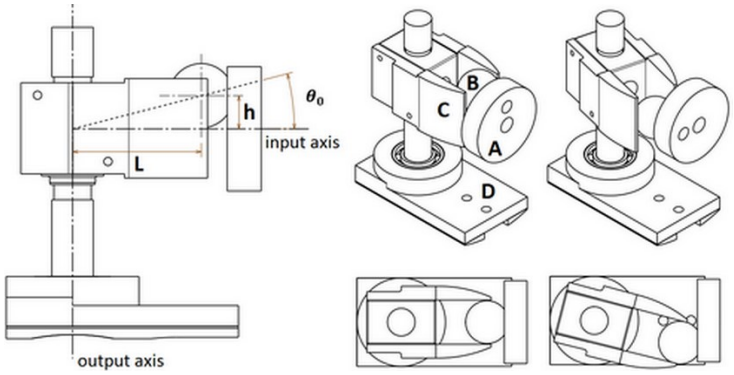

Figure 3.6: Kinematic scheme of the modified spatial-cam kinematic joint [66].

In order to overcome these difficulties, the original design in [65] has been modified by the author [66], as shown in Figure 3.6: the driving arm A has been replaced by a disk, while pin B has been substituted with a sphere. By means of this assembly, the critical issue mentioned above has been definitely solved. Furthermore, since driving disk A is installed on the motor shaft and fixed by means of a grab screw, the fin oscillation amplitude can be easily changed by adjusting the disk position forward or backward along the motor shaft without the need to disassemble the transmission system.
With the new meaning of the geometrical parameters *h* and *L*, defined in Figure 3.6 and 3.7, expressions (3.5), (3.6) and (3.7) still hold. Therefore, at the same condition for the ratio *h/L*, stated by equation (3.8), the approximated motion laws expressed by (3.9) are still acceptable for the present kinematic solution.

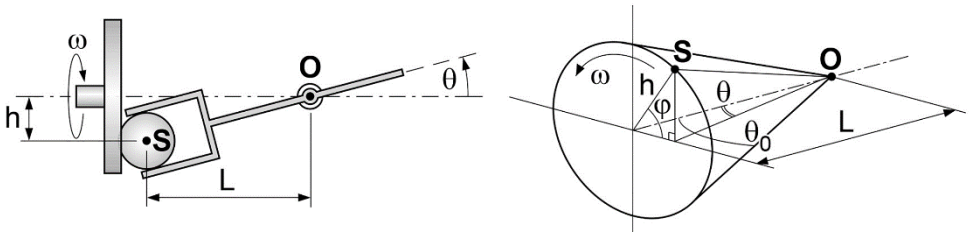

Figure 3.7: Kinematics of the spatial-cam joint [56].

3.4 Robot preliminary sizing

It is here presented a simple analytic model used to size the thruster (i.e. the caudal fin) of a swimming robot. The original procedure was provided by Triantafyllou in [63] and adopted by the author of the present work in [67-69] to design three *ostraciiform* swimming vehicles. A more detailed method, coupling CFD and multi-body analysis to account for the whole robot dynamics, will be presented in Chapter 5.
An *ostraciiform* swimming robot cruising in a straight path at average constant speed must generate enough thrust to balance the hydrodynamic drag exerted by the fluid:

$$D = \frac{1}{2}\rho_w c_D A_f U^2 \tag{3.10}$$

where ρ_w is the density of water, U is the targeted swimming speed and A_f is the wetted frontal surface of the vehicle. Appropriate values for the coefficient of drag c_D are function of the *Reynolds* number and are detailed in [18]. Therefore, in terms of power:

$$P_D = \frac{1}{2}\rho_w c_D A_f U^3 \tag{3.11}$$

According to the model provided by Tryantafyllou in [63], a propulsive thrust is generated when an oscillating foil accelerates the equivalent added mass of water surrounding it. Thus, the average propulsive power P_{prop} can be approximately computed by multiplying the power

of the hydrodynamic torque T_{am} required to accelerate the added mass of water surrounding the fin, with the propulsive efficiency η of *ostraciiform* locomotion [70].

$$\begin{aligned} P_{prop} &= \eta\overline{\left(\left|T_{am}\dot{\theta}\right|\right)} \\ T_{am} &= \left(\frac{9\pi}{8}\rho_w\left(\frac{B}{2}\right)^4 H\right)\ddot{\theta} = I_{am}\ddot{\theta} \end{aligned} \tag{3.12}$$

where the fin angular velocity and acceleration are the derivatives of expression (3.4) and the geometric parameters B and H are defined in Figure 3.8.

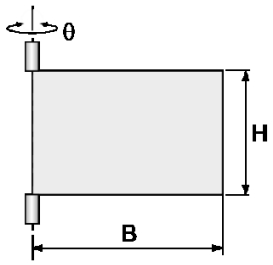

Figure 3.8: Geometry of the caudal fin.

By substituting the expression of the *Strouhal* number for *ostraciiform* locomotion (3.3) in the derivatives of (3.4), the following expressions are computed:

$$\begin{aligned} \dot{\theta} &= -2\pi\frac{St\ U}{2B\sin\theta_0}\theta_0\sin(2\pi ft) \\ \ddot{\theta} &= -4\pi^2\left(\frac{St\ U}{2B\sin\theta_0}\right)^2\theta_0\cos(2\pi ft) \end{aligned} \tag{3.13}$$

Finally, by equalling equations (3.11) and (3.12), where (3.13) is used in the latter to express the oscillating fin angular velocity and acceleration, while assuming $H \approx B$ as suggested by Tryantafyllou in [63], the following expressions can be obtained:

$$\begin{aligned} R_{eq} &= \lambda H_{av} \\ \lambda &= f(St, \theta_0, \eta) \end{aligned} \tag{3.14}$$

where R_{eq} is the frontal surface equivalent radius, H_{av} is the average height of the caudal fin and λ is a function of the *Strouhal* number, the oscillating amplitude θ_0 and the *ostraciiform* locomotion efficiency η.

As stated in subsection (2.5.1), the main components of a bio-inspired vehicle manufactured according to the "oscillating plate" architecture are the cylindrical rigid forebody and the tail section, where the fin is connected to the robot stern through a revolute joint. The body radius lower bound is set by the payload housed in the fore section. The largest components are the

robot battery pack and its main controller, i.e. a National Instruments MyRIO board. Since the transversal section of this device is a 90 mm x 25 mm rectangle, the fore body radius has been set to 60 mm. Thus, according to equations (3.14), where the amplitude of the oscillation θ_0 is chosen equal to 14°, *St* to 0.4 and the *ostraciiform* locomotion propulsive efficiency to 0.17 as predicted by the CFD analysis presented in Section 3.2, the caudal fin average height H_{av} results equal to 170 mm. All the other quantities are summarized in Table 3.1.

R_{eq}	B	H	θ_0	St	η
60 mm	200 mm	170 mm	14°	0.4	0.17

Table 3.1: Results of the robot preliminary sizing.

3.5 Dynamic analysis of the transmission systems

In the following Section, a simple analytic hydrodynamic model is presented and employed in order to estimate the torque acting on the motor shaft due to the fin oscillation at a certain frequency. The total torque T_{total} due to the external and inertial loads, computed with respect to the fin shaft, is composed by three terms:

$$T_{total} = T_{damp} + T_{fin} + T_{am} \tag{3.15}$$

The term T_{am} is due to the acceleration of the added mass of water surrounding the fin and has already been expressed by (3.12) in the previous Section. T_{damp} is the effect of the drag force that is opposed to the fin motion, while T_{fin} represents the torque component given by the fin inertia. The term T_{damp} can be computed according to the expression stated in [63]:

$$\begin{aligned} T_{damp} &= \left(c_d \rho_w \frac{B^4}{4} H\right) |\dot{\theta}|\dot{\theta} = \beta |\dot{\theta}|\dot{\theta} \\ T_{fin} &= \left(\rho_f H \int_{-s/2}^{s/2} \int_0^B (r^2 + s^2) dr ds\right) \ddot{\theta} = I_{fin} \ddot{\theta} \end{aligned} \tag{3.16}$$

where ρ_w is the water density, ρ_f is the density of aluminum alloy, s represents the thickness of the fin and c_d is the drag coefficient of a flat plate perpendicular to the flow; the geometric parameters B and H have already been defined in Section 3.4 and presented in Table 3.1. The former analytic model has been verified by means of the CFD simulation technique described in Section 3.2: Figure 3.9 shows a good correspondance between analytic data and numerical predictions. Table 3.2 summarizes the geometric parameters in (3.16).

I_{am}	I_{fin}	β
$= 6.01 \cdot 10^{-2}$ kg m^2	$= 0.36 \cdot 10^{-2}$ kg m^2	$= 2.72 \cdot 10^{-1}$ N ms^2

Table 3.2: Parameters of the caudal fin

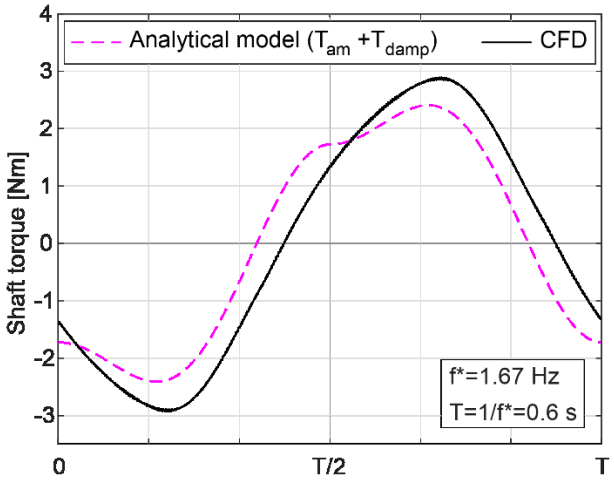

Figure 3.9: Shaft torque for a frequency f of 1.67 Hz; comparison between CFD and analytical model (only the added mass T_{am} and damping T_{damp} components are considered).

Equation (3.15) can be recomputed with respect to the driving shaft by means of expression (3.6) and by applying the work-kinetic energy theorem:

$$T_{total}\dot{\theta} = T_{total}\left(\frac{h}{L}\sin\varphi\right)\omega = T_{motor}\omega \tag{3.17}$$

Equation (3.17) proves that the implementation of a transmission system like those presented in this work, introduces a gear ratio proportional to h/L which in turns is equal to the tangent of the fin oscillation amplitude θ_0. Therefore, since the latter quantity is much lesser than one, as stated in Section 3.1, then the torque sensed by the motor is reduced with respect to a direct drive and a smaller actuator can be chosen.
The former conclusion applies to both the Scotch-Yoke and the cam-like mechanism. Figure 3.10 shows the torques sensed by the motor when friction forces are applied to the joints of the devised systems. Table 3.3 summarizes the friction coefficients introduced in the analytic models of the transmission mechanisms.

Scotch-Yoke Mechanism	
Pin (steel) – Slot (PTFE)	0.09
Prismatic Joints	0.25
Linear Slide Bearing	0.18
Spatial-cam kinematic joint	
Sphere (steel) – Groove (PTFE)	0.09

Table 3.3: Friction coefficients in the proposed transmission systems.

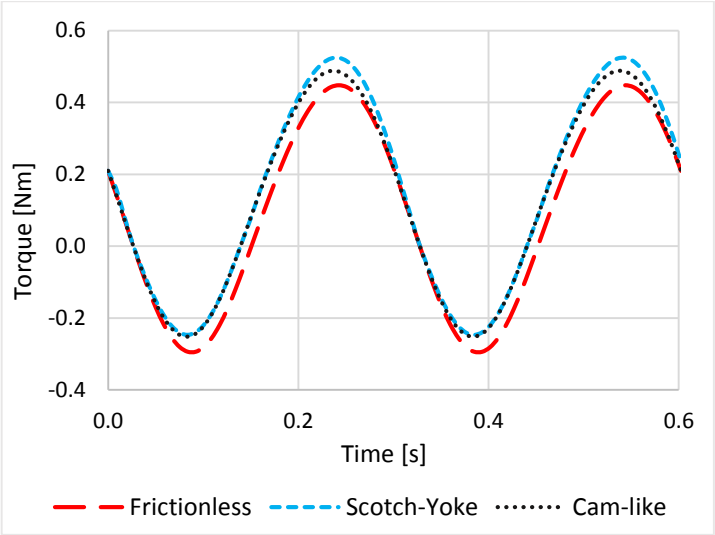

Figure 3.10: Total torque senses by the motor in three different conditions: frictionless (equal for both mechanisms) Scotch-Yoke and Cam-like transmission systems with applied friction [59].

Compared to the frictionless transmission system, the mechanical efficiency of the cam-like mechanism is 79.2%, while the corresponding value for the Scotch-Yoke solution is 70.6%, due to additional friction losses in the prismatic joints and in the coupling box. In the same way, the maximum torque sensed by the motor when the proposed solutions drive the fin shaft are respectively 9% higher than the frictionless condition for the spatial-cam joint and 17% higher for the Scotch-Yoke.

A further comparison is carried on by analyzing the proposed solution from a manufacturing point of view: Figure 3.11 shows a virtual prototype of both mechanisms; when compared to the cam-like transmission, the Scotch-Yoke solution is

i. Less compact: indeed, it results 25 mm longer in the robot roll axis direction, which in turn, considering the tail cross section R_{eq}, corresponds to a +4% of the vehicle total mass in water, calculated according to a preliminary assessment of the vehicle volume required to house the onboard payload.
ii. More expensive: due to a larger number of parts and components. Furthermore, the cost to purchase prismatic joints grows quickly when their size falls below 8-10 mm.
iii. Harder to manufacture: the rails of the prismatic joints must be carefully aligned in order to prevent the risk of malfunctions and vibrations.

According to the previous considerations, the spatial-cam kinematic joint has been employed as the fin transmission mechanism of the *ostraciiform* swimming robot manufactured by the author of the present dissertation. According to the total torque computed in this Section, a 12 V DC brushed motor, namely a Pololu 37Dx70L mm, with a free-load speed of 150 rpm, stall torque 1.4 Nm, 64 CPR Encoder and a 70:1 gearbox, has been chosen as the fin actuator [71]. The selected gear ratio allows the motor to spin at a constant angular speed of 100 rpm, close enough and comprised between the highest output power and the maximal efficiency

condition, respectively attained at 75 and 110 rpm. Additional details on the motor controller, driver and power supply are provided in the following Section with assembly blueprints and specifics.

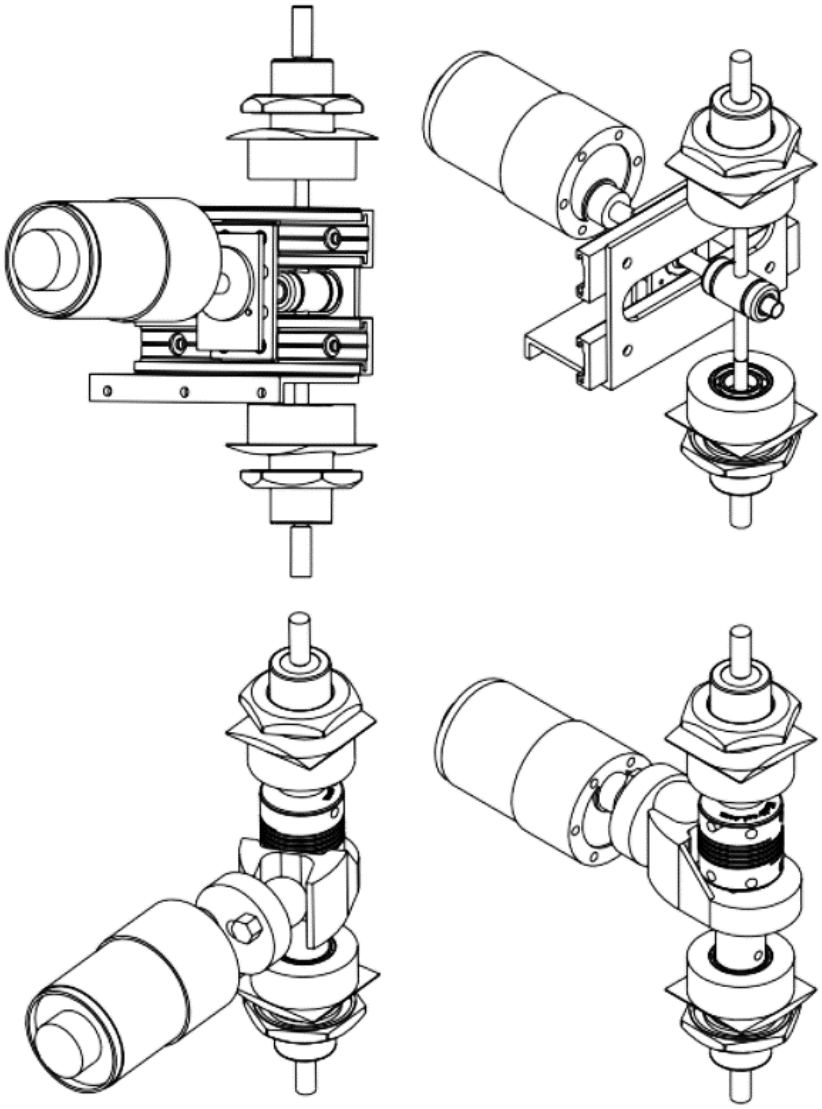

Figure 3.11: CAD prototypes of the Scotch-Yoke (upper scheme) and spatial-cam (lower scheme) transmission systems [69].

3.6 Robots manufacturing

The prototypes in [68-69] share the following features: a modular architecture and a hybrid propulsion system. The *ostraciiform* swimming robot in [68], named BRAVe - standing for Bimometic Research Autonomous Vehicle - has been presented on the occasion of the 2016 Student Autonomous Underwater Challenge – Europe, SAUC-E, at the Centre for Maritime Research and Experimentation (CMRE) at La Spezia, Italy, where it has won the Innovation Award. The second prototype [69], called DORI – the diminutive of "dorico", which means "from Ancona" – is much smaller and has been manufactured to test the performances of the transmission systems devised by the author.
The modular architecture consists of an assembly of waterproofing compartments composed by a cylindrical pressure hull enclosed between two flanged sockets and sealed by o-rings. This solution has been also adopted to manufacture the housing of the Optical Underwater Wireless Communication (OUWC) module designed for the SUNRISE platform within the OPTOCOMM project [72-74]. Because the compartments have been manufactured to be independent and watertight, permeability tests have been conducted on the modules one by one in order to validate the pressure hulls to reach a 100 m depth.
The hybrid propulsion system consists of two different types of thrusters: the fin installed on the robots tail section and three screw propellers, two oriented in the forward direction while the third is oriented along the vertical. The purpose of this redundancy is to allow the vehicle to navigate nimbly, turning around the yaw axis to adjust its heading and change its depth.

3.6.1 BRAVe prototype

BRAVe architecture consists of a three-compartment assembly with the following features: a waterproofing case, a battery pack, and a wired communication device designed to connect the various modules. The case is a cylindrical pressure hull (120 mm outer diameter, 5 mm wall thickness, 500 mm length) enclosed between two flanged sockets and sealed by o-rings. From prow to stern, there is the vision compartment (VC), the core compartment (CC) and the propulsive compartment (PC), as shown in Figure 3.12. Fully assembled, the vehicle is 1500 mm long (1700 mm including the caudal fin) and has a mass of approximately 15 kg.

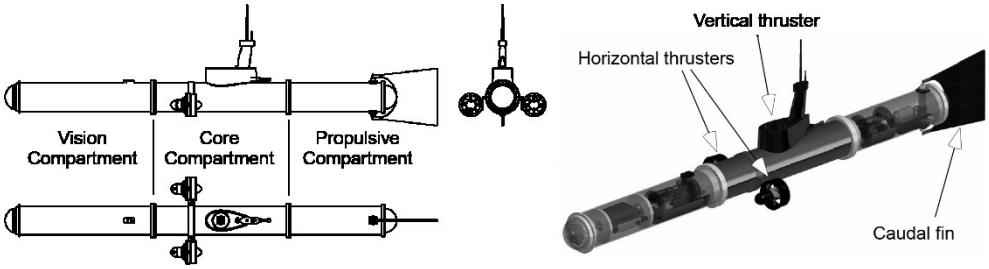

Figure 3.12: BRAVe blueprints and compartments assembly (left), thruster configuration (right) [68].

The vision compartment houses the robot sensory payload, which includes a set of cameras arranged in a custom layout, the control devices required to run the acquisition processing

software, and a battery pack capable of powering the entire module during a mission. In order to acquire pictures and videos from the environment, the VC pressure hull is made of Perspex. The core compartment houses the main controller of the vehicle, the vertical thruster, two BlueRobotics horizontal thrusters and a battery pack capable of powering the electronics and save data, even in the event of a major failure of the other modules. Because the weight and the buoyancy due to the vision and propulsive modules must be supported by the CC during out-of-water and underwater operations, its hull is made of aluminum. Two MyRIO boards provided by National Instruments manage the vehicle during its mission. One is exclusively dedicated to the vision module in order to allocate more resources to the video and image processing algorithms. The vertical propeller is ducted inside a foil-shaped sail manufactured by the 3D Fused Deposition Modeling (3D-FDM) technique. The propeller axis of rotation passes through the centers of buoyancy and mass of the entire robot in order to minimize the pitching moment during depth changing maneuvers.

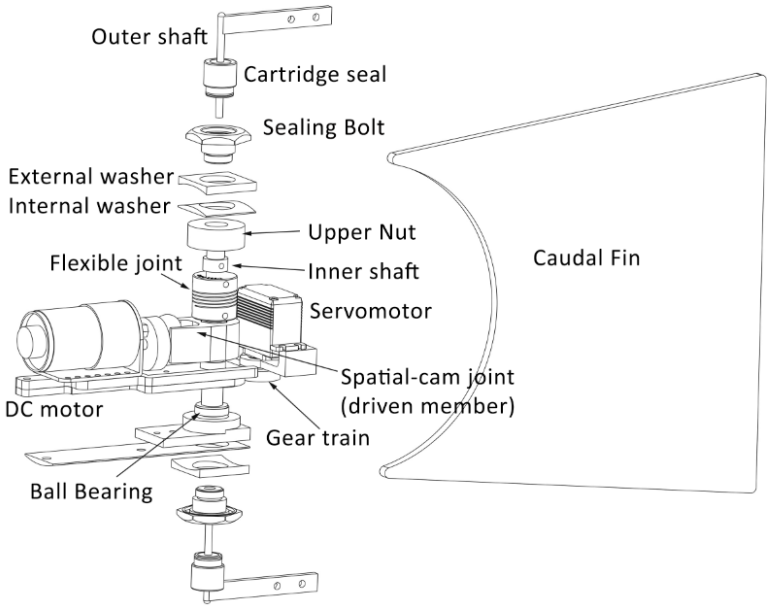

Figure 3.13: CAD assembly of BRAVe Propulsive Compartment.

Finally, regarding the Propulsive Compartment, the spatial-cam kinematic joint described in Subsection 3.3.2 and the aforementioned Pololu DC motor have been succesfully integrated in the tail section to drive the robot caudal fin, as shown in the test assembly of Figure 3.13. The driven member has been manufactured by 3D-FDM, while the other components – such as the driving disk – have been turned starting from an aluminium rod. Particularly, the fin shaft has been realized in four parts in order to ease its assembly and maintenance: two parts are screwed to the driven member inside the Perspex cylindric case of the compartment, while the remaining two parts are external to the case and must be in some way connected to their internal counterparts. Therefore, the main issue here has been the sealing of the areas where

the fin shaft passes through the cylindric hull. In order to overcome this difficulties, a custom support, made of aluminum and assembled like a bolt and its nut, has been manufactured by lathe: the nut, which is internal to the cylindrical case, has a threaded hole on the outward-looking face and bearing seat in the inward-looking face, where a radial ball bearing is housed in order to allow the shaft to spin. The bolt, which is external to the cylindrical case, has a an o-ring groove turned in the lower side of the hexagonal head, while its upper face is holed to house the cartridge seal showed in Figure 3.13. Finally, two curved washers, manufactured by 3D-FDM are employed in order to allow the bolt and nut to adapt to the curved surface of the cylindrical hull. A special adesive, traditionally adopted for marine applications, has been used to permanently fix the external washer to the case. All other connections are sealed by o-rings and can be thus dissassembled for maintenance and set-up operations. However, since the presence of fastned bolts may cause misalignments between the internal parts of the fin shaft, a flexible joint has been included in the shaft assembly to prevent that risk and allow the shaft to spin freely. Figure 3.14 shows the physical assembly of the driving mechanism inside BRAVe Propulsive Compartment. A bolt and nut sealing solution has been succesfully employed also to prevent water leaks in the Core Compartment, where the vertical propeller has been installed.

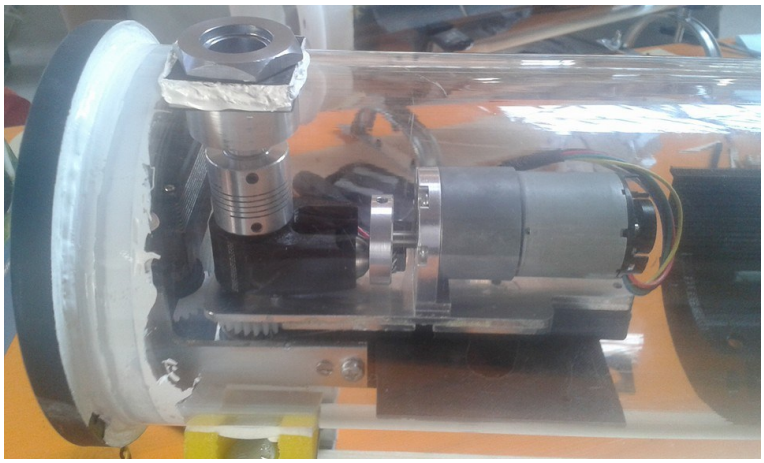

Figure 3.14: Assembly of the propulsive section [68].

Although the robot can use its horizontal propellers to adjust its heading and perform turning maneuvers, a second steering mechanism has been implemented in the biomimetic propulsive system in order to test its turning capability in view of the future elimination of the horizontal thrusters: since the introduction of the cam-like transmissione mechanism constraints the fin to rotate simmetrically around the vehicle vertical plane, the average value of the transversal force generated by the fluid-structure in an oscillation cycle is equal to zero, thus neglecting any possibility to generate a centripetal force component. In order to overcome this problem, the following solution has been devised: instead of fixing the DC motor to the compartment case, its supporting structure has been constrained to the fin shaft by means of a revolute joint and a servomotor has been installed behind the shaft itself to adjust the anglular position of

the DC motor with respect to the case. Here, the maximal rotation is limited to 20° because of the cylindrical hull internal surface. The choice to constraint the DC motor to rotate around the fin shaft forces the driven member to rotate it too in order to align itself with the actuator, while continuing to spin due to the contact with the driving sphere. Two rotations around the same axis are thus superimposed and the final result is that the neutral position of the fin is moved outside the vehicle vertical plane of simmetry, as shown in Figure 3.15, allowing the robot to steer. Even if the turning capability exhibited by the vehicle has seemed acceptable for simple cruising direction adjustments, the system assembly has proved difficult while the servomotor has been unable to prevent vibrations due to its slow response to control signals. For these reasons, the steering capability has been removed in the successive versions of the proposed prototype. Finally, Figure 3.16 shows the physical assembly of BRAVe.

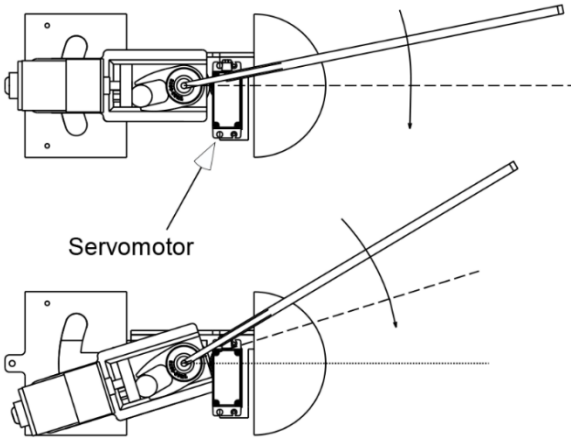

Figure 3.15: Steer control mechanism [67-68].

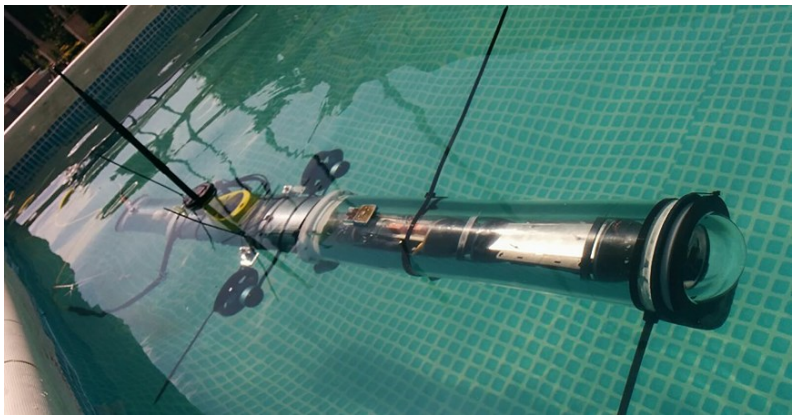

Figure 3.16: BRAVe underwater robot during a test at CMRE [68].

3.6.2 DORI prototype

As stated before, DORI has the same "oscillating plate" architecture of BRAVe but it's more compact and solid. As a whole, the robot consists of a two-module assembly: the longer fore body and the short tail section. From bow to stern, the vehicle is 600 mm long (or 800 mm including the fin) and has a mass of approximately 6 kg. The assembly was validated to safely reach 100 m without water leakages or structural damages.
The body is composed by an aluminum cylindrical pressure hull, enclosed between two acetal neck flanges; a Perspex dome closes the forward-most flange. In order to prevent any water leakage, a double o-ring seal was created between the flange and the dome. This module is 400 mm long and the cylinder wall is 5 mm thick. The body houses a vertical thruster ducted inside a low-drag shaped sail manufactured by 3D-FDM technique. The propeller axis of rotation passes through the center of buoyancy of the entire vehicle in order to minimize the pitching moment during depth changing manoeuvres. In order to allow the robot to steer and control its trajectory, two commercial horizontal thrusters were fixed on the sides of the vehicle, aligned with its roll axis. The aim of these components is to create a pure yawing moment during forward navigation, in order to adjust the robot heading. In future works, they will be replaced by pectoral fins. The body also houses the onboard electronics that consists of a battery pack sized to complete a two-hour mission, the robot main controller, namely a NI MyRIO, the Inertial Measurement Unit and three Photon microcontrollers used to manage the fin motor, the vertical and the horizontal thrusters.

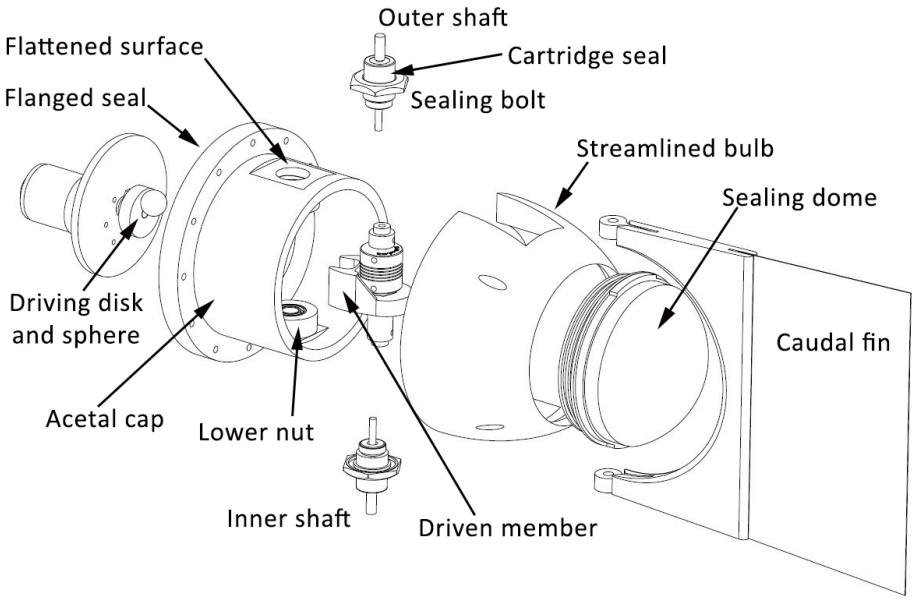

Figure 3.17: CAD assembly of the tail section [69].

The tail section consists of cylindrical cap manufactured by lathe from a POM/acetal block. The forward-most part of this module is connected to the body by twelve bolted screws while a double o-ring seal prevents water leakages between the joining surfaces. A second Perspex dome closes the tail section while allows inspections of the fin actuation system. The custom bolt and nut system developed for the BRAVe prototype has been employed also on DORI to seal the surface where fin shaft passes through the hull. However, in order to eliminate the outer washers, which may prove critical due to the poor mechanical properties of the printed material, the cylindrical cap has been accurately flattened near the holes corresponding to the bolt and nut connection, as shown in Figure 3.17 [69]. The cap hollow part houses the cam-like transmission system, its drive and the fin shaft, which has the same structure (i.e. flexible joint and two-parts assembly) already used on BRAVe. Finally, as stated in 3.6.1, the steering mechanism has been eliminated in order to prevent vibrations. Figure 3.18 shows the physical prototype of DORI.

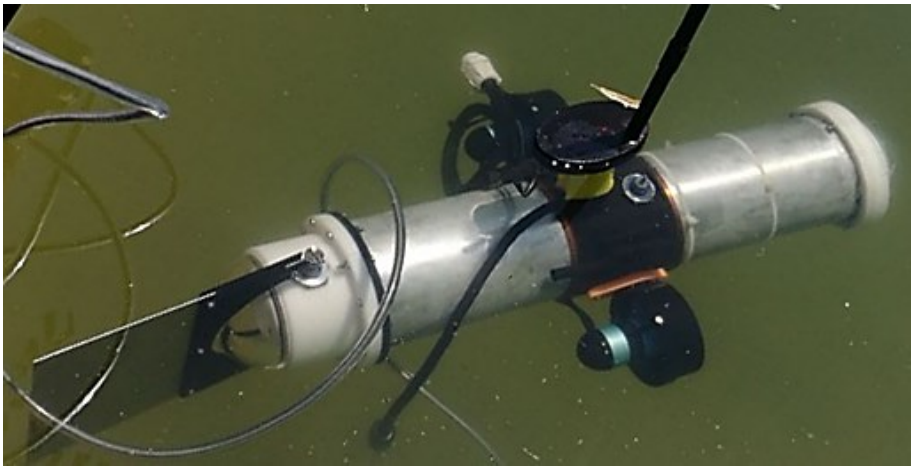

Figure 3.18: DORI physical prototype [69].

Pertaining to the targeted swimming performances, the authors conducted various tests, in and out of the water, in order to calibrate the ACS712 current sensor they used to measure the current absorbed by the DC motor and thus estimate the total torque acting on it. The following experimental set-up was then arranged: the vehicle was immersed into a 2 m depth pool and a 100 rpm constant angular velocity was imposed to the drive by means of a PID controller, corresponding to the prescribed 1.67 Hz fin oscillation frequency. The inertial measurement unit recorded a 0.42 BL/s average forward speed, while the targeted swimming velocity, predicted by the model in [63], was 0.5 BL/s. A possible explanation was found by analysing the motor current absorption and its angular velocity: when it spins at 100 rpm, the continuous torque provided is 0.47 Nm, which is higher than the maximum torque sensed by the motor when dynamic friction is not applied to the joints, as shown in Figure 3.10. Still, the maximum torque required to the drive, when friction is computed into the model, rises close to 0.5 Nm, which is higher than the maximum available torque at 100 rpm. This evidence is supported by the angular velocity read by the encoder: the motor actually slows

down near the angular positions corresponding to the maximum values of the torque inside a cycle. Therefore, since propulsive thrust depends on the square of the drive angular speed, it is reasonable to expect a decrease in the robot average swimming velocity. However, since the aforementioned drop is limited to a small portion of the oscillation cycle, namely ±5° around the angular positions corresponding to the maximum torque, and the adopted dynamic model only predicts the average forward speed according to the average propulsive power, it is tough to formulate a quantitatively relationship between the drive angular velocity drop and the swimming performances. This prediction will be the object of the multi-body analysis detailed in Chapter 5, where a more precise hydrodynamic model is employed to solve the robot dynamics. A further explanation could lie in an overestimated *ostraciiform* swimming efficiency value, which also depends from the fish body shape and not only by the fin. Since the vehicle tail external shape is not optimized like the body of a boxfish, it is reasonable to assume that the incoming flow is disturbed by the shape corners of the hull joining elements (flanges, screws) with a resulting reduction of propulsive efficiency.

3.7 Further optimization of the actuation system

As previously stated in Section 2.4, besides the inspiration to fish locomotion, other strategies developed by biological system to optimize their motion capability can be imitated: animals can, in many cases, temporarily store and release mechanical energy by means of elastic internal structures which are strained in certain phases of the motion and then relaxed in other phases with a recovery of energy [75]. This capability has been deeply proved for terrestrial animals and invertebrate swimmers; dealing with vertebrate swimmers, tests conducted on their locomotion apparatus demonstrated that some fishes (e.g. shark, eel, marlin, dolphin, cetaceans) possess skin, tendons and axial skeleton that behave like springs, able to store and release energy thus improving the efficiency of the propulsion. Furthermore, a detailed model proposed in [27] demonstrates that the elasticity associated to the muscles acting on the tail of many fishes is characterized by a stiffness which is near to the optimum value that would guarantee a power positive at any time during the motion. The latter property is fundamental in a propulsion system which is not equipped with an energy recovery device: as it will be explicated more in detail in the following of this Section, even if the work required to generate the fin oscillation is always the same, the addition of springs in the propulsion mechanism influences the shape of the power law. An optimal value of the spring stiffness can be found in order to make the power always positive, and, at the same time, to obtain a lower peak of maximum power. The result is that the positive work in an oscillation cycle is lower than in the case without the spring, thus, being not possible to recover energy during the negative power phase, an energy saving effect is obtained.
Inspired to biological systems, several examples can be mentioned where the addition of one or more elastic component is exploited in order to improve the energetic efficiency of robotic fish with oscillating plate thrusters. The dynamics of a two degrees of freedom spring-driven oscillating foil propulsion is studied in [28]; it is demonstrated that the use of springs, one for the lateral motion, the other for the rotation of the fin, contributes to increase the energy efficiency. The use of a flexible tail is proposed in [76-77]; in this case the tail itself acts as a spring. As the optimum elasticity of the fin is not constant and changes with the velocity of the motion and with the oscillating frequency, the same authors designed a system able to

vary dynamically the effective length of the elastic fin, in a way that the stiffness of the tail can be adjusted in real-time to comply the optimal conditions.
Guided by the aforementioned results, it is here presented a simple procedure to optimize the *ostraciiform* thruster of the biomimetic vehicle introduced in 3.6.2, in its maximal efficiency navigation condition identified in Sections (3.4) and (3.5). Therefore, the propulsive system will be re-designed to integrate a torsional spring acting on the driven shaft of the oscillating fin in order to replicate the effect of elastic internal structures on the locomotion of biological systems, thus avoiding negative power at the motor during motion. By adopting this solution, in absence of an energy recovery system, the machine efficiency is expected to increase. An improvement in the energy efficiency results in an increased autonomy of the AUV, which allows for more enduring missions (e.g., survey of underwater pipelines) and allows also to launch the vehicle from a base which is farther from the region of interest of the task. Furthermore, although *ostraciiform* locomotion is the least efficient among other types of fish swimming modes, the design of more complex and efficient thrusters (such as multi-segmented flapping foils) can be conceived as a serial combination of simple oscillating mechanisms, i. e. of the same type of the one used on DORI. Thus, the optimization of the *ostraciiform* biomimetic thruster represents a fundamental issue in order to achieve a global efficiency even in more complex swimming mechanics.
After the integration of the torsional spring on the driven shaft, equation (3.15) modifies as:

$$\begin{gathered} T_{total} = T_{damp} + T_{fin} + T_{am} + T_k \\ T_k = k\theta \end{gathered} \tag{3.18}$$

where T_k is the elastic contribution given by a linear torsional spring with constant stiffness k. Equation (3.18) can be rewritten by using the coefficient T_{am} from expression (3.12), β and I_{fin} from (3.16), whose values have been reported in Table 3.2. Then, considering that from equation (3.4) derives

$$\ddot{\theta} = -(2\pi f)^2\theta \tag{3.19}$$

then equation (3.18) can be reformulated in:

$$\begin{gathered} T_{total} = \left(I_{am} + I_{fin}\right)\ddot{\theta} + \beta\dot{\theta}\left|\dot{\theta}\right| + k\theta = \\ = \beta\dot{\theta}\left|\dot{\theta}\right| + \left[k - (2\pi f)^2\left(I_{am} + I_{fin}\right)\right]\theta \end{gathered} \tag{3.20}$$

From the previous equation arises the role of the torsional spring in the design of the actuation system: by assigning a proper value to the stiffness of the spring it is possible, at a given condition of motion, to counterbalance the torque due to inertial terms. In other words, being f^* the steady state oscillating frequency at which the propulsion system is expected to have the optimal behavior, the optimal stiffness of the spring results:

$$k^* = (2\pi f^*)^2\left(I_{am} + I_{fin}\right) \tag{3.21}$$

In this case, in fact, the torque T^*_{total} at the driven axis can be obtained by imposing $k = k^*$ into equation (3.20):

$$T^*_{total} = \beta\dot{\theta}|\dot{\theta}| + \left[4\pi^2\left(I_{am} + I_{fin}\right)\left(f^{*2} - f^2\right)\right]\theta \tag{3.22}$$

It can be observed that the term proportional to θ is null at steady motion ($f = f^*$):

$$T^*_{total}(f = f^*) = \beta\dot{\theta}|\dot{\theta}| \tag{3.23}$$

Thus, only the damping force act as a resistance. Torque C and power P_m at the motor shaft can be found by imposing the power flow through the transmission system in order to supply the resistant power P_r; the mechanical efficiency of the spatial-cam kinematic joint calculated in Section 3.5 has been used in order to take into account the energy dissipation due to friction forces acting on the actuation system:

$$\begin{aligned} \eta_m P_m &= P_r \\ \eta_m C\omega &= T_{total}\dot{\theta} \end{aligned} \tag{3.24}$$

where the subscript "m" has been used to characterize the mechanical efficiency η_m due to the integration of the transmissione mechanism, from the propulsive efficiency η, also called *Froude* efficiency, introduced in 3.2 and expressed from equation (3.2). Thus, in the case of optimal stiffness of the torsional spring, it is:

$$\begin{aligned} P^*_m &= \frac{T^*_{total}}{\eta_m}\dot{\theta} \\ C^* &= \frac{T^*_{total}\dot{\theta}}{\eta_m\omega} \end{aligned} \tag{3.25}$$

That leads, at steady motion at the optimal oscillation frequency:

$$\begin{aligned} P^*_m(f = f^*) &= \beta\frac{|\dot{\theta}^3|}{\eta_m} = \frac{\beta}{\eta_m}\left(\frac{h}{L}\right)^3 \omega^3|\sin^3(\omega t)| \\ C^*(f = f^*) &= \beta\frac{|\dot{\theta}^3|}{\eta_m\omega} = \frac{\beta}{\eta_m}\left(\frac{h}{L}\right)^3 \omega^2|\sin^3(\omega t)| \end{aligned} \tag{3.26}$$

Table 3.4 summarizes the parameters used in equations (3.26).

h	L	η_m	f^*	k^*
8 mm	30 mm	0.79	1.67 Hz	6.98 Nm

Table 3.4: Parameters of mechanical power and torque at $f = f^*$.

The optimal oscillation frequency f^* in Table 3.4 has been identified in Sections 3.4 and 3.5, resulting equal to 1.67 Hz.
The previous equation has been expressed in terms of the angular velocity of the driven axis $\dot{\theta}$ or, by substituting the second equation in (3.9), in terms of the motor velocity ω. In both formulations it can be observed that the motor power and torque are always positive or null. Therefore, at the optimal frequency, the motor provides a torque always in the same direction and the power flow is unidirectional, from the motor to the driven axis. This is noticeable since a negative motor power would mean that the motor is working as a brake; in this case, in absence of an energy recovery system, an amount of energy would be dissipated. With the optimized law of the resistant power, even if the theoretical work necessary to generate a cycle of oscillation of the fin remains the same, it is accomplished with a power law that is always positive and that gives the minimum positive peak. These results are shown in Figure 3.19 and 3.20.

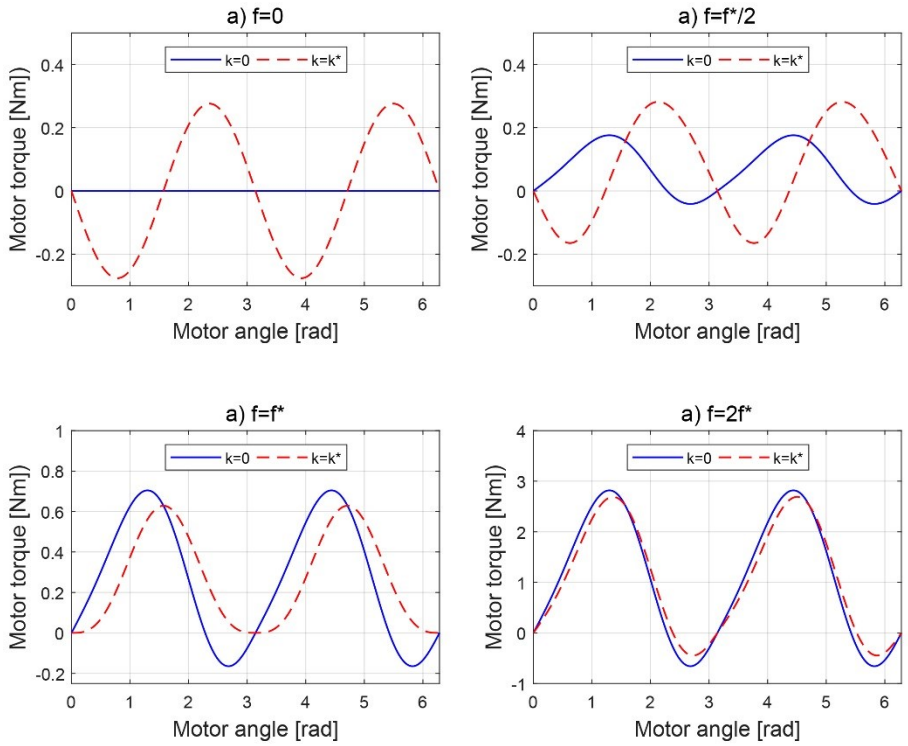

Figure 3.19: Plot of C (with $k = 0$) and C^* (with $k = k^*$) at four different oscillation frequencies: a) f = 0 Hz, b) $f = f^*/2$, c) $f = f^*$, d) $f = 2f^*$, being f^* the optimal frequency resulting from Sections 3.4 – 3.5.

Motor torque and power have been plotted as a function of the rotation angle of the motor at four different oscillation frequencies, from 0 Hz to twice the optimal frequency f^*. Dashed lines refers to a propulsion system equipped with a torsional spring with stiffness $k = k^*$, while

solid lines refers to a system without the spring ($k = 0$). From the comparison between the two scenarios, the optimal condition is observable in plots c): at the optimal speed, the spring equipped system presents the aforementioned advantages, which contribute to increase the energy efficiency and the range of tasks of the vehicle. As a drawback, the duty of the motor results greater at low speeds, which are typical of transient phases; nevertheless, it sounds reasonable to expect that the task of the vehicle will be executed in the optimal condition for the major part of the mission time. Furthermore, if the peak values of torque and power at $f = 2\,f^*$ and $k = 0$ are considered as reference values to size the motor, it can be seen that the system with $k = k^*$ never overcomes those picks, neither at speeds lower than f^*. This means that the addition of the spring does not involve an increase in the motor size.

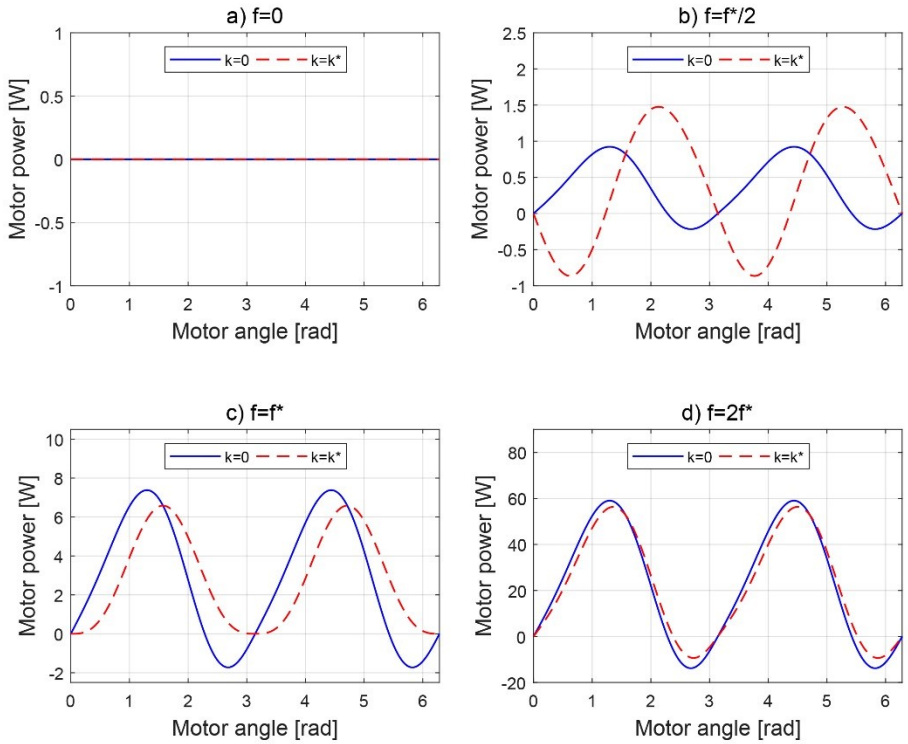

Figure 3.20: Plot of P_m (with $k = 0$) and P_m^* (with $k = k^*$) at four different oscillation frequencies: a) $f = 0$ Hz, b) $f = f^*/2$, c) $f = f^*$, d) $f = 2f^*$, being f^* the optimal frequency resulting from Sections 3.4 – 3.5.

Table 3.5 is a further demonstration of the benefits obtained: for three different oscillating frequencies of the fin, from a half to twice the optimal speed, it is computed the positive work L^+ done by the motor in a cycle (in absence of an energy recovery system the positive work corresponds to the energy consumption). The comparison between the two scenarios, with or without the spring effect (i.e. $k = k^*$ or $k = 0$), states that at the optimal frequency the energy consumption can be reduced by 10%, while at a double speed still occurs an energy saving,

even if lower (4%). On the other hand, at an oscillating frequency lower than f^*, the energy consumption increases. Similar effects can be noticed also on the peak values of the motor power ($P_{m\ max}$ in Table 3.5).

	$f = f^*/2$	$f = f^*$	$f = 2f^*$
L^+ ($k = 0$)	0.46 J	1.86 J	7.44 J
L^+ ($k = k^*$)	0.68 J	1.68 J	7.14 J
Δ%	+46%	-10%	-4%
$P_{m\ max}$ ($k = 0$)	0.92 W	7.38 W	59.05 W
$P_{m\ max}$ ($k = k^*$)	1.48 W	6.59 W	56.36 W
Δ%	+60%	-11%	-5%

Table 3.5: Positive work for cycle (L^+) and peak power ($P_{m\ max}$) at different oscillation frequencies.

Figure 3.21 shows a CAD model of the propulsive section after the integration of the torsional spring on the fin shaft: two flanged ball bearings built to operate in a corrosive environment are mounted on the fin shaft and then attached to a couple of reinforced bended sheet metal supports. The fork-shaped torque transmitter has a rectangular groove where the drive-sphere engages. The same component is used to connect the fin to the output shaft, thus eliminating any possibility of misalignment between the fin neutral configuration and the robot vertical plane of symmetry. Indeed, the whole mechanism is flooded in the water, while the only sealed component is the motor, waterproofed by a dynamic sealing used in pumps design. Finally, the whole section will be housed inside a streamlined bulb manufactured by high-resolution Streolitography. The physical prototype is actually under construction.

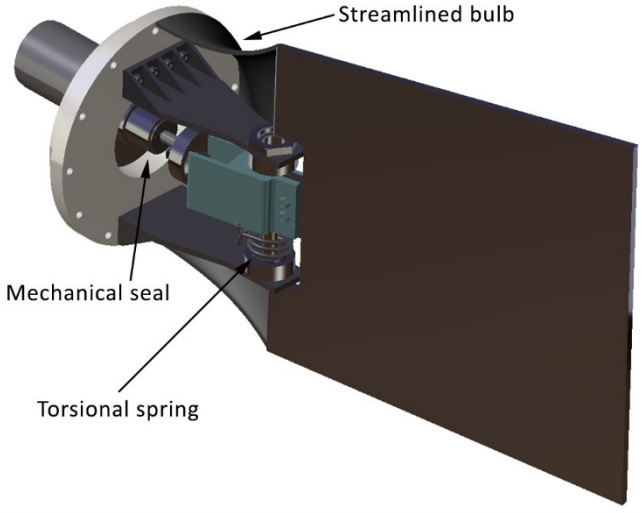

Figure 3.21: Virtual prototype of the tail section after the integration of the torsional spring.

3.8 Navigation Guidance and Control System

The type of mission that the prototypes presented in Section 3.6 have to perform at this stage of development is the execution of a well-defined task expressed as a list of points of interest to reach and actions to perform. Thus, the robot does not need complex planning capabilities. AUVs typically proceed by dead reckoning for long intervals, relying only on the information provided by on-board sensors. Allotta [78-79] proposed an underwater navigation system, developed inside the ARROWS project, that exploits the measurements from various sensors and relies on an unscented Kalman filter (UKF) or an extended Kalman filter (EKF) for the state estimation. The measured quantities are processed while the vehicle navigates in dead reckoning to calculate its dynamics. These results are then used to compute the motor control signals: the thrusts produced by the motors allow the vehicle to follow the desired dynamics while the sensor suite provides the real physical outputs to be used in the navigation system. In order to perform the specified type of mission, the designed vehicle must be able to manage different type of payloads, such as sensors, underwater communication devices and actuators. Thus, the robot mechatronic architecture has been designed as a system characterized by a high degree of modularity and abstraction. Briefly, the intelligent control architecture can be summarised by its three main components: the Low Level, the Communication Level (i.e. Implemented by Wire) and the High Level, while the union of these two is the NGC system, as shown in Figure 3.22. The NGC system communicates with the base station, which has two main purposes: to create, modify and upload a mission (the mission creator) and to remotely control the AUV through a custom-made interface (the Remote User Interface marked with an orange continuous line). The custom-made interface is used to perform tests, initiate the mission and gather data.

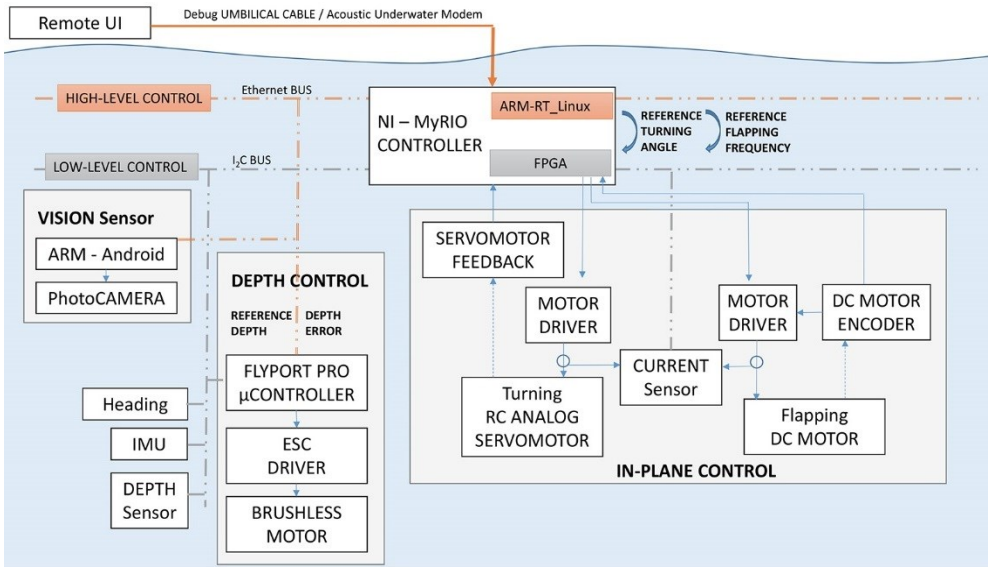

Figure 3.22: Navigation Guidance and Control hardware [68-69].

The Low Level is made up by an array of devices connected with the High Level through the industrial I^2C bus, indicated in Figure 3.22 by the grey dashed line. Two types of devices are present: commercial off-the-shelf (COTS) devices, like the Inertial Measurement Unit (IMU) the Global Positioning System (GPS) and the depth sensor, and custom-made, such as the energy and thruster manager. The custom-made devices have a minimum degree of autonomy in case of emergency, which involves taking the system into a safe steady state with a faster and predictable response to malfunctions (such as low battery or water leaks inside the hull). This approach avoids single point failures in the NGC system if there is a major fail related to the High Level. When a new device is attached to the shared bus, a High Level module is able to discover it and communicate with it in a transparent way.
The High-Level component of the NGC system is based on techniques frequently adopted in AUVs and in remotely operated vehicles navigation [80-83]. As stated before, a Linux Real-Time device (NI MyRIO) has been chosen as the system hardware platform. The High-Level has been coded according to the Multi Agents System characterization theory (MAS). This type of approach allows to increase the system abstraction and modularity in order to design distributed entities (agents) able to fulfil different tasks autonomously. The agents (coded as LabVIEW *.VI files) can read data and interact with the Low Level components through a Blackboard-type information share modality that maintains synchronized all the data of the NGC system. In the present work, these techniques are simplified in order to make the vehicle components purely reactive according to the intelligent agent definition provided by Wooldridge [84]. The developed agents, in fact, lack on proactiveness and social capabilities. Cognitive capabilities are not required either for the type of missions performed by the present robot but the control architecture is ready to consider it as to connect with ROS compatible robot agencies.
The software architecture comprises five threads (one for each agent): navigation, guide, low level, communication manager and log manager. Each thread manages a specific section of the entire vehicle autonomy. The modules are synchronized with each other in order to allow for the exchange of messages and information, as shown in Figure 3.23. The navigation thread manages the different functioning modalities: manual, automatic and emergency. The system starts in manual mode, where the user can manually control and monitor the status of the robot like a ROV. If necessary, it is also possible to enable or disable the auto-depth and auto-heading algorithms. The system changes from manual mode to automatic mode when the start command is received. Once the automatic mode is active, the mission executor processes the loaded mission. The latter is described by many tasks and a mission timeout. When the mission timeout is reached, the mission is over. Each task has its own timeout and is arranged as a finite state machine. A state is composed of a series of elements that allow the system to perform cyclically repeatable actions, as well as actions conditioned by the system status and its global variables, like depth and heading, along with battery and thrusters operative status. For example, one element of the state structure represents a single vehicle moving action to be sent to the guide module. Before processing the following element, the mission executor waits for the end signal from the guide module. The mission is editable and loadable to the vehicle through a proper graphical user interface (GUI) and it is exchanged and stored as a JavaScript Object Notation (JSON) string. When all the states of a task have been executed or the task timeout is reached, the mission executor processes the following task. When the mission reaches a timeout or all the tasks have been handled, the automatic mode manages the surfacing action of the vehicle. Once the vehicle is out of water, the system

switches to manual mode. If a critical condition is experienced, such as low battery or a hardware failure, the mission terminates. When the external emergency switch is triggered, the entire system enters in emergency mode and any thruster is shut down until the external switch is triggered again. This module is executed with a period of 100ms. The guide module performs the commands sent from the navigation module while sending a feedback. It also manages the auto-depth and auto-heading algorithms with an execution period equal to 100 ms. The low level module communicates with the systems connected with the low level bus (I^2C) and keeps the system status information up-to-date. In addition, the low level module updates the status of all the connected devices that the guide module has access to. This module is executed every 10ms. Each device attached to the bus has a proper read/write period that is a multiple of that of the module, and is arranged to avoid overlapping with other requests generated within a single module execution. Indeed, the code is developed with non-blocking criteria on a software Real-Time operative system (Linux Real Time – NI RTOS) The communication manager communicates with the base station mainly. Specifically, it transforms the information received and transmitted through Wi-Fi or acoustic modem and the real-time telemetry data in a file format that can be handled by other software threads. Finally, the log manager writes the log files in different formats and saves them in a USB pen-drive every 100ms.

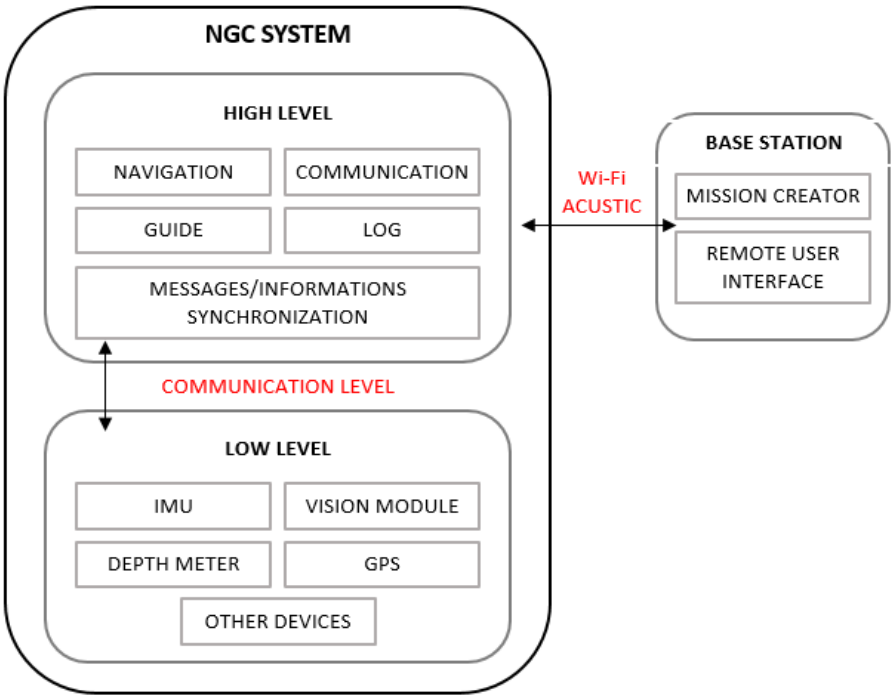

Figure 3.23: Multi-agent architecture [68-69].

Chapter 4.

Experimental validation

4.1. Introduction

The possibility to replicate successfully the swimming modes that fish evolved in thousands of years, depends from the deep understanding of the fluid mechanics principles exploited by marine animals' locomotion. By using advanced simulation and measurement techniques, engineers are trying to quantify the propulsive performances of biological swimmers, such as thrust and efficiency. Particularly, extensive work has been conducted both on fin-shaped oscillating foils separated from the fore body [26], [85] and on fully assembled bio-inspired underwater robots as well [19-20], [86-88].
According to literature, two alternative experimental setups have been devised to investigate the performances of flapping-based propulsion. In the former, the swimming robot is either towed at known speed through a water tank or, equivalently, placed in a freestream at a given velocity in a water tunnel [86-87]. The propulsive force produced by the thruster is then easily measured by sensors attached to the towing structure or to the flapper shaft. When such setup is used, the flapper actuating kinematics is completely decoupled from the speed of towing or from the oncoming flow velocity, a condition dissimilar from what occurs in biological locomotion. On the other hand, in the alternative setup, the robot swims at a passively self-propelled speed on a low-friction rail using undulatory motion [20], [88]. An average steady velocity is reached when thrust balances the drag force exerted by the fluid on the self-propelled vehicle. However, the increase in inertia due to the presence of the additional parts (strut, slide blocks, etc.) results in a difference of acceleration between the robot and the biological swimmer, hindering the measurement of the forces acting on the robot. A review of recent advances on self-propelled bodies is given in [89].
This Chapter presents the experimental setup devised by the author to validate the numerical predictions, presented on Section 3.2, on the propulsive performances of an oscillating foil and its driving mechanism. Here, the foil spins around its rotation axis following a harmonic law of motion as a function of time, a kinematic condition that closely matches the caudal fin pendulum-like oscillation in *ostraciiform* locomotion. *Ostraciiform* swimming robots have already been tested in other works: in [90], a pulley and weight system was used to generate a constant pull force on the robotic fish. The experiments were conducted with four different fin shapes at various oscillating frequencies, while the measured added mass and drag forces were compared to a theoretical model. An alternative setup was devised in [54], where the oscillating flapper was placed in an oil tank. A beam deflection-based force sensor was built to measure both the lateral and normal, i.e. thrust, force components generated by the foil. Results were finally used to design and fabricate a robotic boxfish.

Compared to the aforementioned works, this Chapter presents the experimental setup suitably designed to obtain a complete dynamic characterization of the oscillating fin as a function of the *Strouhal* and *Reynolds* numbers of the flow-structure interaction phenomena. Mainly, the aim of the present work is to measure the force components and the torsional moment acting on the fin shaft by means of a custom force sensor designed according to the computational fluid dynamics analysis already presented in Chapter 3. While the oscillating fin is placed in a constant velocity freestream in a water flume, the actuation and transmission systems – by which the required harmonic motion is generated – are placed above the free surface. After a brief description of the water tunnel characteristics, the following sections detail the control and acquisition platform for the experimental setup, the force sensor design and fabrication, the system assembly and calibration, flow visualization, then finally the preliminary and final tests results.

4.2 Tests overview

The numerical predictions presented in Section 3.2 have been performed on an oscillating flat plate geometrically identical to the fin thruster employed on the *ostraciiform* swimming robot shown in Section 3.6.2, whose dimensions have been reported on Table 3.1. The flow *Reynolds* number in the simulations has been calculated according to a swimming speed of the order of 0.5 BL/s, corresponding to 0.4 m/s, which is the expected cruising velocity for the aforementioned robotic fish. Therefore, *Re* results equal to 10^5. Then, in order to validate the computational fluid dynamic analysis performed on the vehicle *ostraciiform* thruster, two alternative approaches could have been followed, where the first consisted in the application of a force sensor on the fin shaft of the vehicle while the second is the use of a water flume suited to cointain the thruster alone. However, encumbrance limits on the robot propulsive compartment have denied the pursuit of the former approach, while the latter have resulted unfeasible due to the unavailability of a water flume of the required size. Therefore, the only option remaing has been to work on a scale model of the oscillating fin and thus apply the fluid dynamics similitude principle.
According to the Buckingham theorem, if there is a physically meaningful equation involving a certain number n of physical variables, then the original equation can be rewritten in terms of a set of $p = n - k$ dimensionless parameters π_1 ..., π_p constructed from the original variables, where k is the number of the primary dimensions in the aforesaid variables. In the present case, the psysical quantities characterizing fish swimming are the water density and viscosity, a characteristic length (i.e. the fin chord), the incoming flow velocity (which is equivalent to the swimming speed) and a force (or pressure). Since the associated primary dimensions are mass, length and time, then Buckingham theorem states that the dynamics of swimming can be described by two dimensionless parameters, namely the *Reynolds* and *Strouhal* numbers, as results from dimensional analysis. Thus, in order to validate the numerical predictions, it is necessary that both *Re* and *St*, set in the simulations and in the experimental tests, are equal. However, it results easy to prove that this requirement cannot be satisfied: in fact, take λ_c as the scale ratio, which is the ratio between the characterist lengh used in the numerical analysis and the fin chord in the scale model of the experimental tests. Moreover, the fluid properties in both scenarios are the same, in the first case because the author's aim was to compute the propulsive forces acting on the manufactured robot DORI, while in the second because the

available flume can only be filled by water. Then, remembering expressions (2.1), the ratio between the flow velocities in the simulated and test case λ_U can be calculated as:

$$\lambda_c = \frac{c_{CFD}}{c_{test}} > 1$$
$$1 = \frac{Re_{CFD}}{Re_{test}} = \frac{U_{CFD}}{U_{test}} \frac{\nu_w}{\nu_w} \frac{c_{CFD}}{c_{test}} = \frac{U_{CFD}}{U_{test}} \lambda_c \tag{4.1}$$
$$\frac{U_{CFD}}{U_{test}} = \frac{1}{\lambda_c} = \lambda_U < 1$$

where ν_w is the dynamic viscosity of water and c is the chord length of the simulated foil and of the scale model. The available water flume is a 10 meters long, straight channel provided with a recirculating pump and a rectangular section measuring 330 mm wide and 300 mm high, too narrow to cointain the prototype thruster. The flow velocity can be set between 120 and 180 mm/s: then, since the maximum available speed in the water flume is lesser then the flow velocity in the simulated scenario, it results impossible to satisfy the requirement stated by the third equation in (4.1). In other words, the equality between the *Reynolds* number of the numerical simulations and the experimental tests cannot be respected.
However, the computational fluid dynamic analysis proved that the propulsive performances of an oscillating foil faintly depend from the *Reynolds* number when the latter is greater than 10^4. This is physical, since the aforementioned value is close to the critical *Reynolds* number that predicts the transition point between laminar and turbolent flow for an airfoil. In other word, past the critical *Re*, the boundary layer around the fin becomes fully turbolent and the propulsive forces generated by the oscillating foil stabilize close to the regime values. This last evidence has allowed the author to neglect the requirement on the *Reynolds* number and proceed with the tests on a scale model, provided that its *Re* is greater than the critical value.
As stated above, the present experimental setup consists of an oscillating foil suspended in a constant velocity freestream in a water flume. The foil shaft is connected to the transmission mechanism (which is placed above the water level) in a cantilever configuration, as displayed in Figure 4.1. The available water flume is a 10 meters long, straight channel provided with a recirculating pump, with a rectangular section measuring 330 mm wide and 300 mm high. The flow velocity can be set between 120 mm/s and 180 mm/s by varying the inclination of the channel. However, since the water flow rate must remain constant due to the principle of mass conservation, its hydraulic head subsequently varies: 220 mm at 120 mm/s and 180 mm at 180 mm/s. This condition imposes a geometric constraint to the maximum size of the tested foil and a compromise choice has to be taken. Particularly, the aim to validate the numerical predictions using the similitude principle, implies that the force coefficients obtained by CFD analysis must coicide with the dimensionless forces and torque measured in the experiments. Thus, their expected values in the scale model of the oscillating fin can be computed as:

$$F_{test} = 0.5\, \rho_w\, U_{test}^2\, S_{test}\, c_{F\,CFD}$$
$$M_{test} = 0.5\, \rho_w\, U_{test}^2\, S_{test}\, c_{test}\, c_{T\,CFD} \tag{4.2}$$

where F_{test} and M_{test} are the dimensional forces and torque measured in the experiements, S_{test} is the surface of the scale fin, U_{test} is the water flume velocity while $c_{F\,CFD}$ and $c_{T\,CFD}$ are the forces and torque coefficients predicted by the numerical analysis.

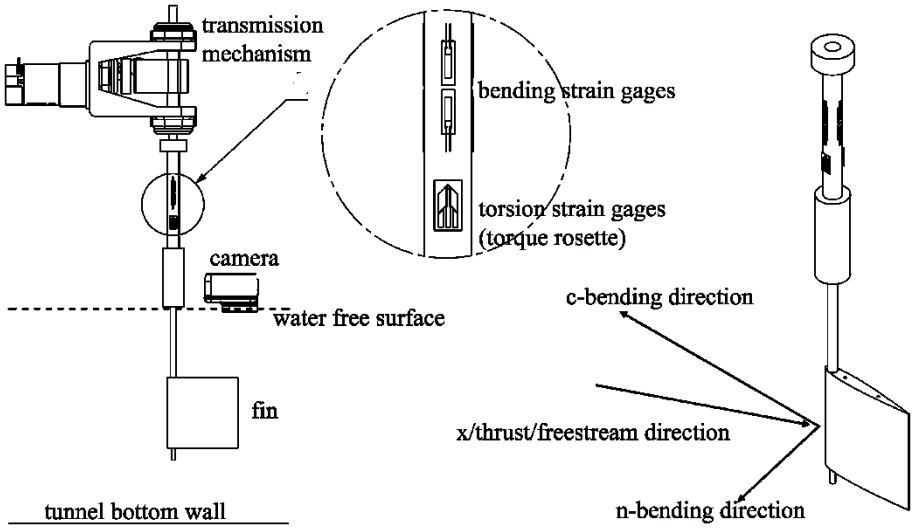

Figure 4.1: Experimental setup layout and forces decomposition.

Since the propulsive force and torque depend from the square of the flow velocity in the water flume, it is convenient to set the freestream speed equal to the maximal available value in the channel, which is 180 mm/s; thus, the hydraulic head has been set to 180 mm. The next step then is the choice of the scale model chord length: a proper sizing would require the analysis of the interferences of the free surface and tunnel bottom wall with the flow around the fin. However, this type of 3D simulation requires expensive and long-lasting numerical analysis currently unavailable at the author's lab. Further considerations regards the *Strouhal* number requirement previously discussed: Table 4.1 shows the oscillation frequencies corresponding to the *Strouhal* number values in the performed CFD analysis.

St_{CFD}	0.2	0.4	0.5	0.7	0.9	1.1
f_{CFD}	0.77 Hz	1.54 Hz	1.92 Hz	2.69 Hz	3.46 Hz	4.23

Table 4.1: Fin oscillation frequencies corresponding to the Stroual numbers set in CFD analysis presented in Section 3.2 (U_{CFD} = 0.4 m/s, c_{CFD} = 200 mm).

Since the *Strouhal* numbers must be equal both in the tests and in the numerical analysis, as required by the similitude principle, then from expression (3.3) it results that:

$$f_{test} = f_{CFD}\,\lambda_c/\lambda_U \tag{4.3}$$

Therefore, in order to replicate the numerical simulation at the highest value of *St* (i.e. 1.1), the scale model must be capable to oscilalte at a maximum frequency computed according to equation (4.3) once a proper value of λ_c has been chosen. Regarding this parameter, a higher valued of λ_c would imply a shorter chord of the scale model, thus reducing the interferences created by the water free surface and tunnel bottom wall. On the other hand, the greater λ_c, the faster the motor must spin in the scale model, as predicted by equation (4.3), with possible vibrations arising on the flume structure which could impede the regular conduct of the tests. That said, a lower bound still exists for λ_c, because a smaller value of the chord consequntly reduces the propulsive forces that the experiments aim to measure.
Guided from the necessity to compromise between two opposite requirements, a value of λ_c equal to 3.33 has been chosen as the geometric scale ratio: the fin chord in the experimental tests results thus equal to 60 mm. The same value has been chosen for the fin height, in order to leave a chord length between the fin upper surface and the water free surface and a chord length between the fin lower surface and the tunnel bottom wall, as show in Figure 4.1. By using the aforementioned quantities, the expected proplulsive forces, that the experimental tests aim to measure, have been calculated according to equation (4.2). Finally, these values have been used to size the force sensor as it will be shown in the following Section.

4.3 Force sensor design and manufacturing

The layout of the experimental setup devised in the present work has been displayed in Figure 4.1. In order to validate the numerical predictions performed in Section 3.2 and thus provide a complete characterization of the propulsive performances of the oscillating fin, the forces and torque acting on the scale model must be properly measured. Particularly, the thrust force is the resultant component always aligned in the freestream direction, while the lateral force is always normal to the former; finally, the hydrodynamic torque direction coincides with the fin rotation axis. The force sensor proposed by the author exploits the deflection and twisting of the fin shaft to indirectly measure the loads, i.e. the propulsive forces, applied to the fin. Thus, in order to achieve this result, a flexible element must be inserted along the rigid shaft: the ideal position is then between the transmission system and the fin, as far as from the latter as possible in order to maximize the moment arm and thus amplify the effect of the applied loads. The indirect measurement of the propulsive forces and torque is obtained by means of three independent groups of strain gages attached to the flexible element: particularly, two groups individually measure the strains due to the bending moments, while the last one deals with the twisting, as it will be detailed in the following. In summary, the proposed sensor will be composed by the flexible element and the attached strain gages.
Regarding the flexible element, the cantilever beam configuration adopted in the setup allows to calculate the strains due to the bending and twisting moments and then to size the sensor, once the type and measurement range of the strain gages have been chosen. The first step, though, is the evaluation of the propulsive forces and torque resulting from the applied loads predicted by the CFD analysis: Table 4.2 shows the corresponding values as a function of the fin oscillation frequency, calculated by means of expressions (4.2). Particularly, the *"T"* and "*L"* subscripts in the forces labels refer respectively to the thrust force (that is always aligned with the freestream velocity) and to the lateral force. The force decomposition is shown in Figure 4.2. Specifically, the *x* and *y* directions represents the axis of the *ground* frame, i.e. a

reference frame attached to the water flume. Furthermore, the subscripts *aver*, *max* and *min* refer to the values of the associated forces and torque at a given frequency: particularly, since the curves of the lateral force and torque have the symmetric behaviour charted in Figure 4.3 with respect to the fin angle, their average value is null and their maximum and minimum coincide apart from their sign. On the other hand, the average value of the propulsive thrust is obviously different from zero, as shown in Figure 4.3; thus, the maximum and minimum values at different frequencies are reported.

f_{test}	1 Hz	2 Hz	3 Hz	4 Hz	5 Hz	6 Hz
$F_{T\,aver}$	-0.00056	0.01799	0.04906	0.09265	0.14875	0.21736
$F_{T\,min}$	-0.01315	-0.01966	-0.03223	-0.05085	-0.07553	-0.10627
$F_{T\,max}$	0.01203	0.05566	0.13036	0.23615	0.37303	0.54100
$F_{L\,max}$	0.12014	0.36943	0.79864	1.40776	2.19680	3.16576
$M_{Z\,max}$	0.00358	0.01204	0.02740	0.04962	0.07873	0.11472

Table 4.2: Expected propulsive forces and torque on the fin scale model computed by means of expression (4.2) at six different oscillation frequencies.

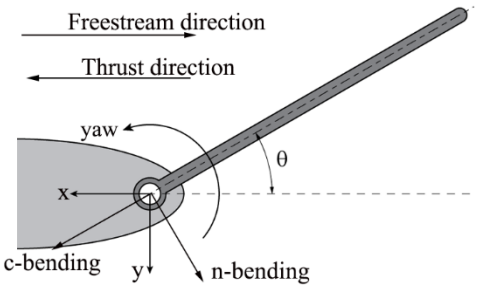

Figure 4.2: Propulsive force decomposition. The *x* and *y* directions represent the axis of the *ground* frame, meaning a reference frame attached to the water flume; c-bending and n-bending refer to the axis of the *moving* frame, i. e. a reference frame attached to the oscillating fin.

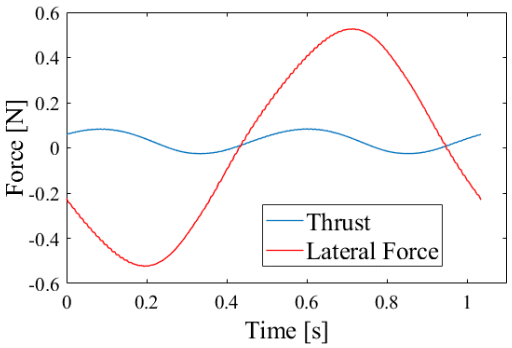

Figure 4.3: Propulsive forces charted as a function of the fin angle in an oscillation cycle at $St = 0.5$.

As stated before, the assembly composed by the flexible element and the fin shaft is attached to the transmission system in a cantilever beam configuration. The side pressure distribution on the fin has been approximated with a resultant force and moment acting on its mid-section, corresponding to the symmetry plane normal to the span direction, by means of expressions (4.2). In other words, since three-dimensional flow effects are neglected, the force and torque resultants are calculated as the integrals of the numerically predicted coefficients of force and torque over the fin surface, multiplied to the flow dynamic pressure. According to the stated hypotheses, it results immediate to solve the statically determined problems of bending and twisting. Once the loads on the shaft are known, the following step is the sizing of the sections of the flexible element and the choice of its material: the tubular, thin-walled section is the best solution in terms of stress solving, simmetry and manufacturing. Then, in order to size properly its dimensions, the following considerations need to be made: the lower bound of deformation for the commercial strain gages is 100 microstrains $\mu\varepsilon$, equal to 10^{-4} mm/mm. In fact, a deformation lower than the prescribed value would be severely affected by noise disturbances. Secondly, since the order of magnitude of the loads applied to the centimeter-scale fin varies from 0.01 to 1 N as a function of the foil oscillation frequency, a sufficiently compliant material, such as plastics, must be selected. Finally, the outer surface of the sensor must be wide enough to house the necessary strain gages, as shown in the following.

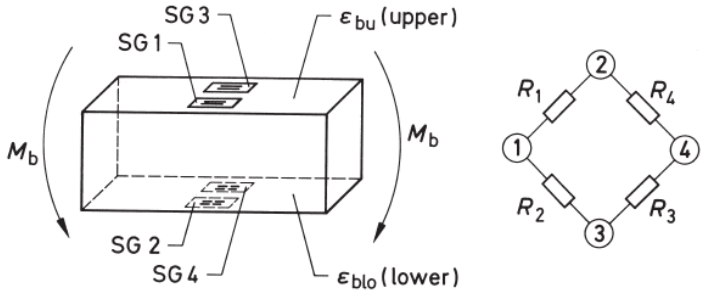

Figure 4.4: Strain gages arrangement in a bending beam and in the Wheatstone bridge circuit [91].

Figure 4.4 shows a possible arrangements of the strain gages in a bending beam [91]; indeed, bending produces positive strain on one side of the bent beam and a negative strain on the opposite side. With mirror-imaged cross-sections, the positive and negative strains have the same magnitude. It is therefore possible to use the features offered by the Wheatstone bridge for the addition of the strain signals: in fact, the bridge equation states that:

$$\varepsilon_1 - \varepsilon_2 + \varepsilon_3 - \varepsilon_4 = \varepsilon_i \tag{4.4}$$

where $\varepsilon_1 \ldots \varepsilon_4$ are the strains signals while ε_i is the indicated strain, i.e. the measure resulting from the addition of the various terms. If a full bridge configuration is chosen, meaning that all four arms of the circuit in Figure 4.4 are actually occupied by strain gages, then the normal strains due to pure tensile and compressive loads applied to the beam are totally compensated,

while thermal strains are compensated to a high degree even without the use of temperature-compensated strain gages. Indeed, equation 4.4 modifies as:

$$\varepsilon_i = 4\,\varepsilon_b \tag{4.5}$$

where ε_b is the bending strain measured by four identical strain gages attached to two opposite sides of the beam as shown in Figure 4.4.
As stated before, the purpose of the proposed sensor is to measure the propulsive forces acting in the x and y directions: i.e. the thrust and lateral force components of the hydrodynamic resultant. However, the strain gages are attached to the outer surface of the sensor, which is fixed to the rotating fin shaft. Thus, if n is the axis of the moving frame which is perpendicular to the faces of Figure 4.4, then the measured bending strains are due to the projection of the aforementioned loads in the n direction. Thus, in order to recompose the propulsive forces acting on the fin, it necessary to measure the bending strains in two perpendicular directions, called n and c, as in Figure 4.3 and in the assembly of Figure 4.1. As a consequence, eight strain gages – four for each direction of the moving reference frame identified by the c and n axis – are required to solve the static problem of the applied propulsive loads once the relative orientation of the fin with respect to the freestream direction has been determined. That's the purpose of the camera in Figure 4.1, as it will be shown in the following Sections.

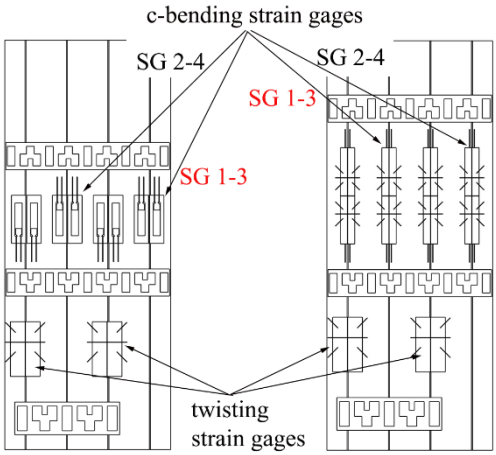

Figure 4.5: Strain gages alternative layouts. Parallel (left), aligned (right)

Figure 4.5 shows two alternative layouts for the bending strain gages: the cylindrical surface of the tubolar sensor has been projected on a plane while the vertical lines identify four faces, spaced by a 90 degrees rotation, which correspond to the sides of the beam in Figure 4.4. As a consequence and according to the previous considerations, two strain gages must be fixed close to a line, representing the couple SG1 and SG3 of Figure 4.4, while the remaining SG2 and SG4, necessary to complete the full bridge, will be attached to the line corresponding to a 180 degrees rotation from the first. By adopting the arrangement on the left, the four strain

gages of the bridge are parallel: thus, the bending strain is measured in the same section of the sensor. On the other hand, the layout on the right is more compact; moreover, since each strain gage is attached in the farthest point from the section neutral axis, then it measures the maximum bending strain due to the associated moment. Therefore, the necessity to minimize the section diameter in order to obtain a compliant sensor suited to measure the small forces in Table 4.2, the aligned arrangement has been chosen for the strain gages of the sensor.
The strain gages displayed in the layout of Figure 4.5 belong to the uniaxial type, meaning that they measure the strain only in the direction of their grid. Although more complex types actually exist, the uniaxial ones are the most compact and narrow, thus perfectly suited for the present application. Particularly, the linear uniaxial KFG 120 manufactured by Kyowa have been selected for the bending moments: their grid is just 1.4 mm wide, 2.8 considering their bonding base. Thus, projected on a circe, the circumferential encumbrance of four strain gages of the aforementioned type, arranged as shown in Figure 4.5 (right), is just 11.2 mm. Regarding the section of the tubolar sensor, manufacturing issues advise against reducing the diameter below 10 mm, particularly critical for the bonding phase. Then, the associated circle measures 31.4 mm, more than enough to host four strain gages of the selected type.
The last step of the sizing procedure is the computation of the sensor thickness and the length of the fin shaft: a first guess for the internal diameter of the tubolar sensor is 9 mm, which is easy to achieve by means of a simple machining performed by lathe. The resulting thickness is then 0.5 mm. Regarding the material choice, both Nylon and PVC are valid candidates due to their low modulus of elasticity. However, PVC is slightly more fragile than Nylon, and that could be an issue given the high number of load cycles that the sensor has to sustain in the tests. Once the material and the section dimensions have been chosen, it results easy to compute the distance between the foil mid-section, which is the point where the propulsive loads are supposed to be applied, and the mid-section of the sensor, which is the point where the bending strains are measured with the aligned arrangement of Figure 4.5. By using the known expression for the bending strain:

$$\varepsilon_b = \frac{M}{EJ} = \frac{Pb}{EJ} \tag{4.6}$$

where M is the bending moment on the measured section, which is equal to the applied load P times the moment arm b, E is the Young's modulus and J is the moment of inertia of the tubolar cross-section. By setting the bending strain ε_b equal to the lower bound of deformation for commercial strain gages, 10^{-4} mm/mm, expression (4.6) can be transformed in order to calculate the moment arm:

$$b = \frac{EJ}{P}\varepsilon_b = \frac{EJ}{P}10^{-4} \tag{4.7}$$

By means of equation (4.7) it results that a moment arm equal to 215 mm is suitable for the measurement of the propulsive forces in Table 4.2; particularly, the smallest force measurable by the designed sensor is equal to 0.01 N with the given moment arm.
Regarding the twisting moment, the possibility to measure the applied torque does not depend from the length of the moment arm. Then it is suffient to verify that the shear strains due to the twisting moment are greater than 10^{-4} for the sized cross-section. By applying the known

expression of the shear stresses and strains due to pure twisting, it results that the defomation at 2 Hz is $1.71 \cdot 10^{-4}$, which is acceptable to validate the torque predictions for positive thrust generation, i.e. for f_{test} greater or equal than 2 Hz, as results from Table 4.2. The strain gages adopted to measure the twisting moment due to the propulsive torque are two torque rosettes, series 062uv 350 by Vishay Group, arranged as in Figure 4.5.

4.3.1 Sensor fabrication and calibration

Specifications on bending strain gages installation suggests that the clamping sections of the sensor, meaning the sections where the flexible element is attached to the fin rigid shaft and to the transmission system, should be distant at least three times the measurement area, which is the length of the surface occupied by the grid of the strain gage, in order to avoid that stress concentrations due to the clampig force affect the measurement. The grid of the uniaxial KFG 120 measure 5 mm: thus, the total length of the designed force sensor is 70 mm, 10 mm for the aligned strain gages, and 30 mm over and below the measurement area. Regarding the clamping sections, they have twice the diameter of the sensor but the same internal diameter, with chamfered edges where the wider section joins the narrower one, in order to avoid stress concentrations. Table 4.3 summarizes the sensor geometry and the mechanical properties.

Material	Section	Lenght	Diameter	Thickness
Nylon	Tubolar	70 mm	10 mm	0.5 mm

Table 4.3: Force sensor geometry.

The strain gages installation sequence consists of three steps: once the flexible element has been manufactured by lathe according to the required geometry, see Table 4.3, a preliminary simulation of the strain gages placement on the cylindrical section is performed. The layout of Figure 4.5 is printed, in a 1:1 scale, on adesive paper and then attached to the manufactured tube, as shown in Figure 4.6. The preliminary simulation is also conducted to familiarize with the narrow spaces available between the strain gages during the bonding phase.

Figure 4.6: Preliminary simulation of the strain gages placement on the cylindrical surface.

In the second step, an alignment grid, i.e. the black lines displayed in Figure 4.7, is drawn on the outer surface of the sensor by means of the special template shown in Figure 4.6, printed by high-resolution stereolithography (SLA). A second template, namely the planar projection of the cylindrical surface of the sensor with the strain gages arranged in their positions, as in Figure 4.3, is laser-printed on transparent paper and attached on glass: such last template is used to position the real strain gages correctly in their own slots, Figure 4.8.

Figure 4.7: Tracement of the aligneament grid. A torque rosette is visible on the left.

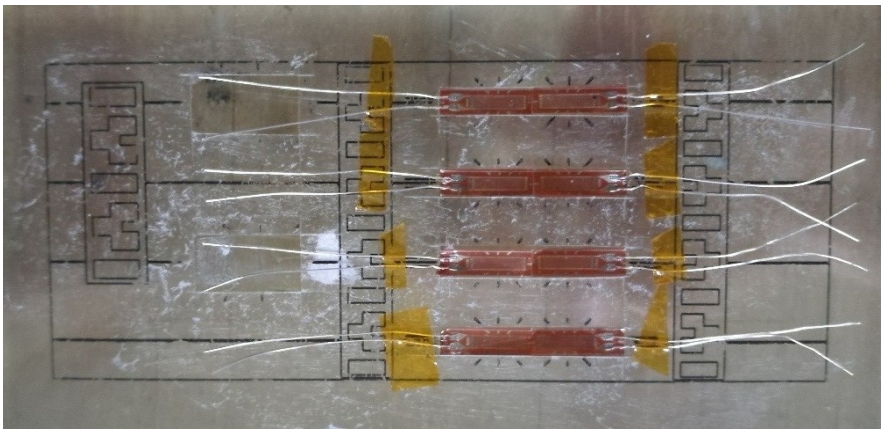

Figure 4.8: Strain gages arrangement on the paper dime. The black marks sorrounding the strain gages are used to match the correct aligneament of the grid.

Once this last preparation step is finished, the strain gages are collected from the transparent paper all at once, by means of a special adhesive tape, the same orange tape visible in Figure 4.7 over the torque rosette. The tape is then positioned on the sensor using the drawn grid as a reference. Finally, the tape is removed from one strain gage in order to bond it to the surface by using a cyanoacrylate-based adhesive, while the others are still maintained in position by the tape. When the bonding procedure is finished, the same operations are repeated for the next strain gage until all of them have been properly bonded to the sensor surface.
Regarding the installation of the torque rosettes, the full bridge configuration suggested for the measurement of the shear strain due to a pure twisting moment is shown in Figure 4.9.

The same arrangement has been adopted for the proposed force sensor, as already diplayed in Figure 4.5.

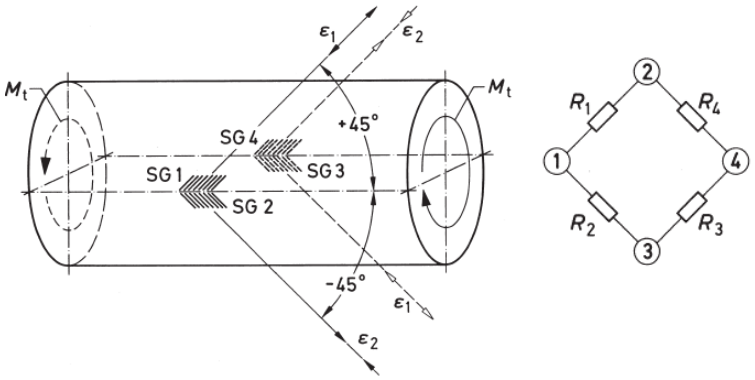

Figure 4.9: Torsion shaft with strain gages mounted in the principal stress directions and their position in the bridge circuit whit the application of two special torque rosettes [91].

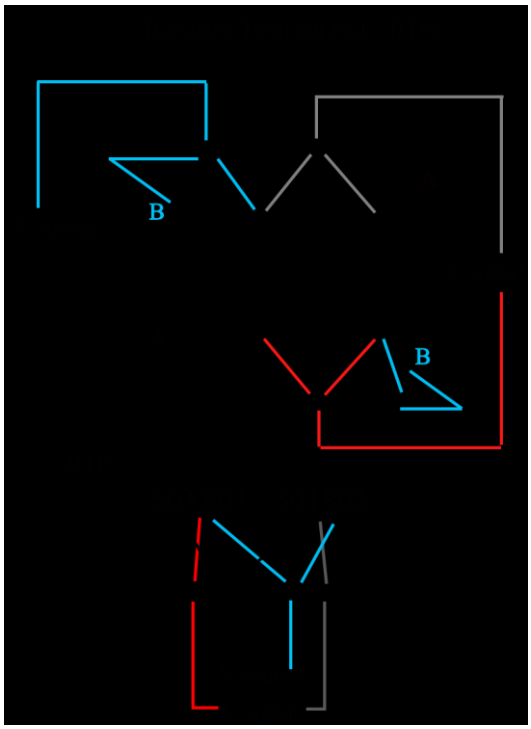

Figure 4.10: Full bridge circuits for a group of bending strain gages and for the twisting strain gages.

Figure 4.10 shows the full Wheatstone bridge circuits for a group of bending strain gages and for the two torque rosettes as well. It is common practice to employ bondable printed-circuit terminals, also known as bondable terminal pads (BTPs), between the main leadwire and the relatively small and delicate jumper wires of the strain gage. Here, their primary purpose is to provide an anchor for both sets of leads, and to prevent forces transmitted along the main leadwire system from damaging the strain gages or degrading their performance. The electric scheme in Figure 4.10 precisely match the wires color actually used in the physical sensor (see Figure 4.11, below). Please also note that the torque rosette possess three jumpers: this is due to the fact that a rosette is composed by two grids arranged at an angle of about 45°; indeed, each rosette in Figure 4.10 has been labeled with a couple of strain gages: SG1-2 and SG3-4; the electrical connection between the grids of each couple is provided by the rosette manufacturer, which is Vishay group for the present application. Finally, the labels V_{source} and V_{signal} refer respectively to the bridge excitation voltage and to the bridge output voltage, i.e. the measuring signal. In conclusion, Figure 4.11 shows the final assembly of the designed force sensor.

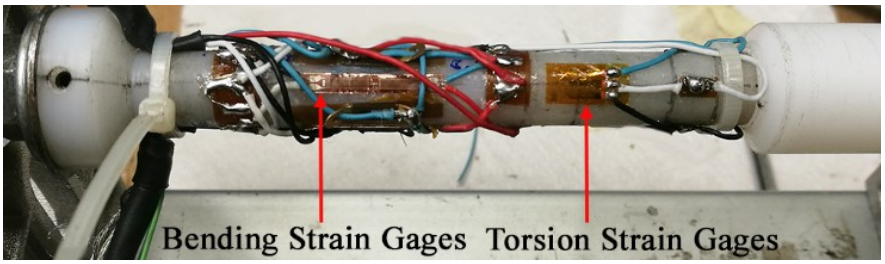

Figure 4.11: Final assembly of the proposed force sensor. The strain gages have been installed according to the arrangement in Figure 4.5.

Before starting the experiments, the sensor has been calibrated for pure bending and twisting using known weights. Particularly, a small support has been attached to one of the clamping sections in order to position the weights at a known distance from the bending measurement area. Then, their values have been calculated by multiplying the loads value of Table 4.2 to the moments arm ratio, meaning the ratio between the propulsive forces moment arm *b* used in equation (4.7) and the aforementioned known distance between the weights and the sensor mid-section. The same procedure has been followed to calibrate the torque rosettes by using the propulsive torque values presented in Table 4.2. Particularly, this phase allowed to set the amplification factor of the adopted amplifier, in order to obtain a measurement signals suited to the ± 10 V differential analog input channels of the employed acquisition platform. Figure 4.12 shows the calibration curves for the bending groups and for the torque rosettes: the linear trend followed by the calibration points confirms the accuracy of the strain gages installation. Please also note that different sets of weights have been used to calibrate the bending groups: with reference to Figure 4.2 and considering that the fin oscillation amplitude is set to 14°, it is easy to show that a group of bending strain gages will be subjected to higher loads than the other. Particularly, the group attached to the surface which is perpendicular to the axis labeled as n-bending in Figure 4.2, will be subjected to the lateral forces of Table 4.2 – which are 5-

6 times higher than the thrust ones – multiplied by the cosinus of the oscillation angle, which is 0.97 when the fin is inverting its motion; on the other hand, the lateral forces projection on the c-bending direction is 0.24 at most, four times lower than the former. Furthermore, since the purpose of the c-bending associated group is to measure the thrust force, it is necessary to bound the range of measured strains to the values of interest in order to amplify the measurement signal. The calibration setup is shown in Figure 4.13.

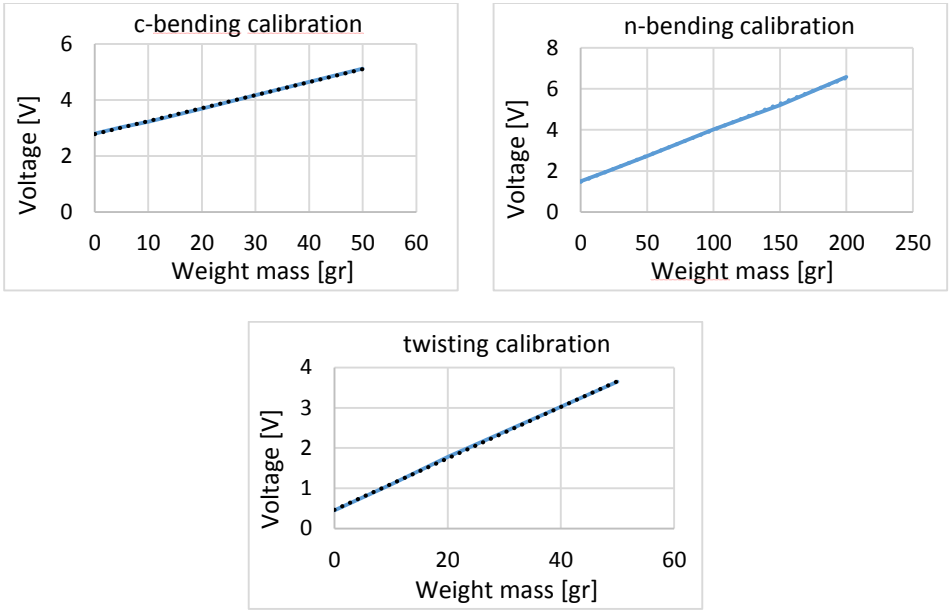

Figure 4.12: calibration curves for the strain gages bending groups and torque rosettes.

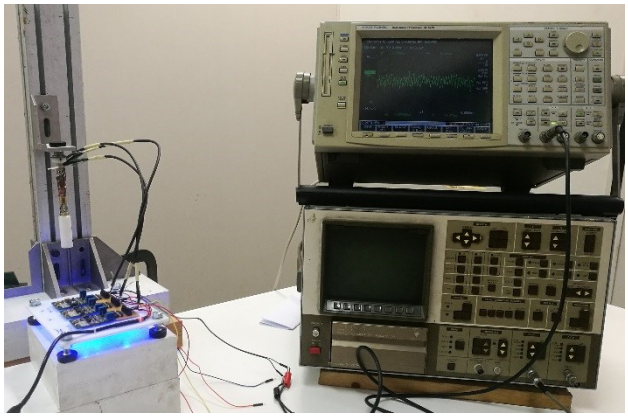

Figure 4.13: Calibration setup: the board with the blue lights is the strain gages amplificator.

4.4 Mechatronic system design

As displayed in Figure 4.1, the oscillating fin is suspended inside the water flume, while the measurement, actuation and transmission systems – by which the required harmonic motion is generated – are placed above the water free surface. The adopted transmission mechanism is based on the spatial-cam kinematic joint already discussed in Chapter 3: the system frame, driving and driven members have been manufactured by FDM 3D-printing techniquques, as shown in Figure 4.14. In addition to the transmission mechanism, the mechatronic system is composed by a 12 V Pololu DC motor, its driver and a National Instruments MyRIO board, a Linux real-time System on Module (SOM) with an embedded dual core ARM Cortex-A9 processor and a Xilinx Z-7010 FPGA Module. The motor, connected to a 19:1 gearbox, can spin up to 500 revolutes per minute. The driver is a dual channel Dimension Engineering 2x32 Sabertooth that is able to supply up to 32 A per motor. Finally, the MyRIO SOM is employed both as the system controller and as its data acquisition device: in fact, it allows to set the motor rotation frequency within the range indicated by Table 4.2 and to synchronize the video recording device, which consists of a GoPro Hero 5 camera, with the acquisition platform. At the same time, the MyRIO-1900 Expansion Port (MPX) connectors allows the board itself to act as the system acquisition device. The necessity to syncronize the recording system with the measurement signals acquired from the force sensor is due to the need to project the loads measured in the c-bending and n-bending directions, in the x and y ones, in order to compute the propulsive thrust and lateral forces, as discussed in Section 4.3. The combination of the recorded video and a dedicated software permits to associate each force and torque measurement to the corresponding angular position of the fin, thus allowing the reconstruction of the propulsive loads.

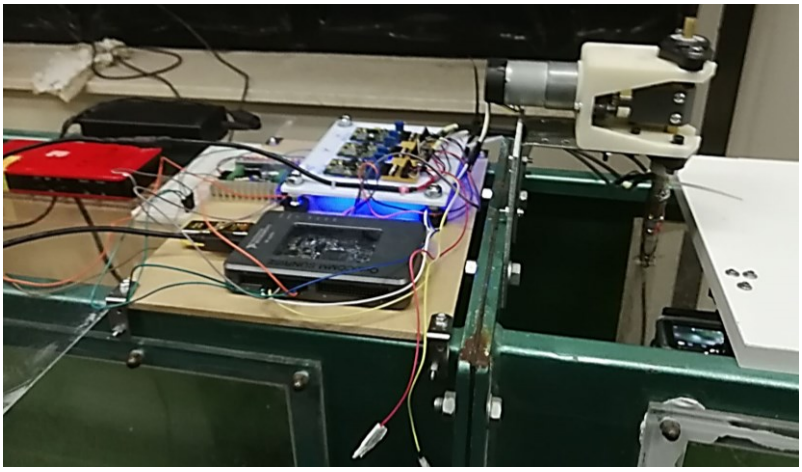

Figure 4.14: Mechatronic system assembled over the water flume. The major components are the red battery pack which powers the whole system, the gray MyRIO board, the strain gages amplificator (with the blue lights), the motor driver (behind the MyRIO), the transmission mechanism with its Pololu drive, the force sensor and finally the recording device inside its underwater case.

All the software has been developed in NI LabVIEW, as shown in the Appendix: particularly, it is composed by two real-time while loops running in parallel and dedicated to two different purposes: the control loop and the acquisition loop. The control loop has the classical state-machine architecture; its main function is to control the motor in order to adjust its frequency to the value set from the user, by means of a PI controller. The control loop is executed every 10 ms, ten times faster than the highest oscillation frequency planned in the test. On the other hand, the acquisition loop has the producer and consumer architecture: data gathered through the analogue input channels at high speed, once every 10 ms, are stored in a queue from the producer loop and then are passed to the slower consumer loop in order to be processes and saved in an external memory storage unit. The acquisition loop starts when a trigger button is pushed by the user: this very action simultaneously activates a dedicated subVI through which the *record start* command is sent, through the Wi-Fi connection, to the GoPro camera.

Figure 4.15: Frame captured by the recording device when the oscillation frequency has been set at 6 Hz. The white marks and their trajectory (drawn in blue) have been obtained by using Kinovea.

4.5 Preliminary tests and flow visualizations

Functional tests have been performed on the various components of the experimental setup. First, the performances of the PI controller implemented in LabVIEW have been investigated within the prescribed frequency range, resulting at most in 0.4 % error between the adjusted motor speed and the value set by the user by using the controls on the Front Panel. The camera synchronization trigger and its dedicated subVI have also been successfully verified. The last test conducted on the setup regards the quality of the videos recorded by the GoPro Hero 5 camera at the highest oscillation frequencies. Several pictures have been acquired by setting the camera to 240 frame rates per second, as shown in Figure 4.15. Despite the darkness due to the low exposure time, the author has been able to reconstruct the fin angular position by tracing the trajectory of a couple of white spots drawn on the foil upper surface. The videos have been processed using an open source software named Kinovea: the curves presented in Figure 4.16 shows the fin angular position as a function of time obtained from the processed videos, at five different frequencies. The trends follow the sinusoidal law of motion exhibited by the oscillating fin an acceptable approximation even at the highest frequencies.
As a further verification, the flow behind the oscillating fin has been visualized by means of dye injections techniques. Dye can be used to mark and visualize particular regions of flow

or individual fluid streamlines. When the purpouse is to mark streamlines adjacent to a test body, dye is injected from small ports on the surface of the object. On the other hand, dye can be released from a thin needle aligned to the local flow in order to mark the streamlines within the fluid. In the latter case, care must be taken to minimize disruption to the existing flow field: for example, the injection velocity should match the local velocity. The injection velocity can be controlled either with a syringe pump or a constant head reservoir, such as the Mariotte bottle. In onder to ensure that the tracer actually follows the undisturbed flow field, its density must match that of the experimental fluid. Since most dyes are heavier than water, they must be mixed with alcohol to achieve neutral density. Contrast is also required in order to achieve a clear visualization.

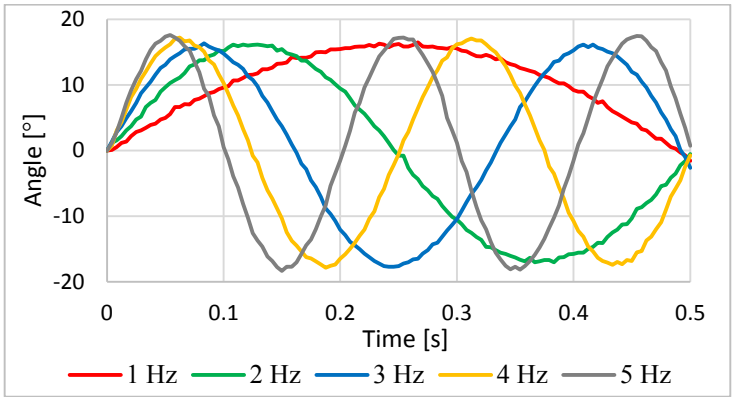

Figure 4.16: fin angular position charted as a function of time, at five oscillation frequencies. The trends approximate a sinusoidal motion law with acceptable approximation.

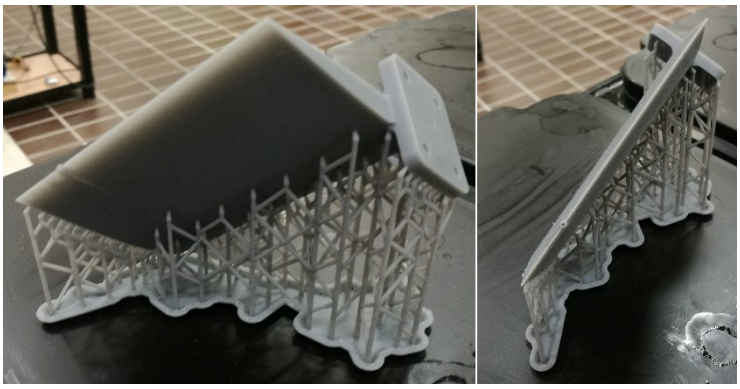

Figure 4.17: Airfoil-shaped noozle manufactured by SLA 3D printing technique and used to inject dye tracers in the flow. The noozle diameter measures 0.8 mm.

In the present setup, the author has used a red dye, commonly employed in the food industry. The tracer has been injected by means of an airfoil-shaped noozle, manufactured by high-

resolution stereolithography (SLA), in order to minimize the disturbances to the freestream. Finally, the injection velocity has been controlled by using a Mariotte bottle.
Flow visualizations and the adopted tools are shown in Figure 4.17 and 4.18: the wake left behind the fin consists of a staggering array of trailing discrete vortices of alternating sign, generated as the foil spins back and forth. The structure of the wake is of a thrust-type, which means that the rotational direction is reversed compared to the drag-producing Karman vortex street seen in the wake of bluff objects. The flow behind the fin has the same kinematic layout of the wake observed behind the Robotuna [6], as shown in Figure 4.19. This last evidence confirms that the proposed setup is capable of generating the motion law of a swimming fin.

Figure 4.18: Thrust-type (Reversed Karman Vortex Street) wake behind the oscillating fin.

Figure 4.19: Thrust-type wake observed behind the RoboTuna [6].

4.6 Experimental tests

Figure 4.20 shows a frontal picture of the proposed experimental setup fully assembled [92]. The fin and other components of the transmission system described in the previous Sections are printed by stereolithography. Particularly, the adopted 3-D printing technique allows the fabrication of hollow parts: this option has been exploited to manufacture statically balanced fins by removing the material behind the rotation axis (where the majority of the foil mass is distributed) and by adding metal parts near the fin leading edge. In this way, the rotation axis

passes through the fin centre of mass and thus the effect of the inertial forces on the bending moments is null. Furthermore, since the aim of the author is to investigate the propulsive performances of an *ostraciiform* swimming robot, the fish model shown in Figure 4.21 has been manufactured in order to be placed in the flume in front of the oscillating foil. This particular configuration represents a bio-inspired vehicle where the recoil on the robot fore body is restrained through the installation of vibration absorbers [93].

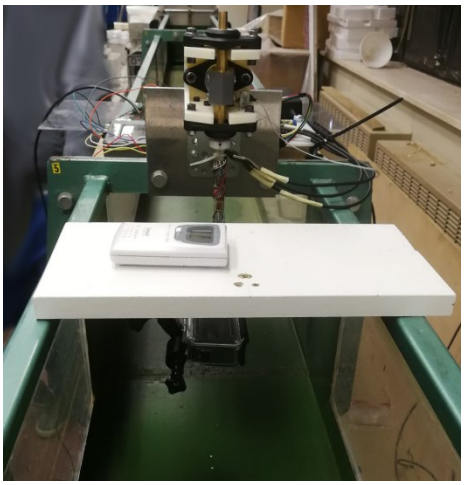

Figure 4.20: Frontal view of the experimental setup.

Figure 4.21: Fish model positioned in front of the fin during the second part of the test.

The test have been conducted at three different oscillation frequencies as shown in Table 4.4, together with corresponding value of the Strouhal number, computed using the scale model fin chord and the water flume freestream velocity:

Frequency	2 Hz	3 Hz	3.5 Hz
Strouhal	0.32	0.48	0.56

Table 4.4: Oscillation frequencies during the test and corresponding St values for the scale model.

At higher frequencies, the deflection of the shaft due to the lateral force has been too large to approximate the fin motion as a pure oscillation. For this reason, the highest frequency value has been limited to 3.5 Hz.
Once the measurement value have been saved in the external storage unit, the reconstruction phase of the force values has begun. As a first step, the voltage values have been converted in force units by means of the calibration curves showed in Figure 4.12; then the fin angular positions have been computed from the frames captured by the recording device by using the software Kinovea, as stated before. The corresponding angular velocities and accelerations have been thus calculated in order to subtract the contribution of the inertial forces and torque from the measured quantities. The resulting values have been finally projected in the thrust and lateral directions.

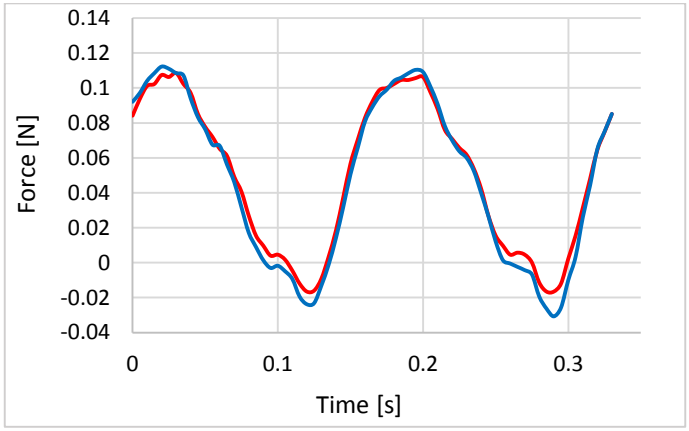

Figure 4.22: Thrust in an oscillation cycle at 3 Hz. Red: freestream; blue: behind the fish.

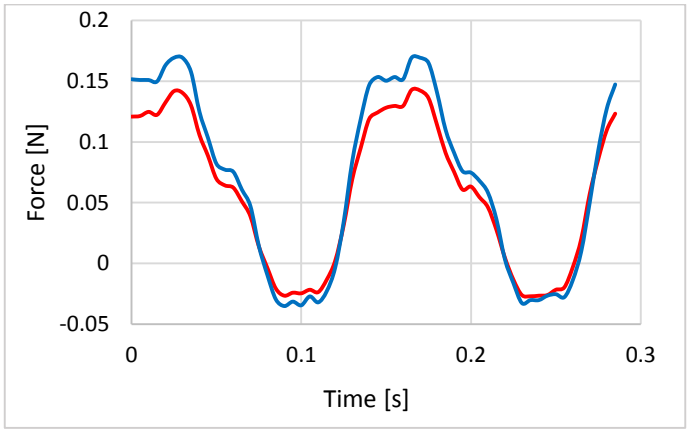

Figure 4.23: Thrust in an oscillation cycle at 3.5 Hz: Red: freestream; blue: behind the fish.

Figure 4.22 and 4.23 shows the measured thrust force at 3 Hz and 3.5 Hz. The trends closely resemble the ones displayed in Figure 4.3; particularly, it can be observed that the frequency of the thrust force is double with respect to the fin motion law, as predicted by the numerical predictions and from airfoil theory. Two different sets of test have been performed: while the red curves refer to the fin positioned in a freestream, the blue cuve shows the thrust force that has been measured when the fish model has been placed in front of the fin. A slight beneficial effect can be noticed from the figures. Regarding the values, the maximum thrust value is comprised between 0.10 and 0.11 N at 3 Hz, compared to the expected value of 0.13 N as in Table 4.2. This has been expected and due to the disturbances created by the tunnel bottom wall and the water free surface. Finally, noise has affected the measurement signals acquired at 2 Hz so the corresponding curves have not been reported by the author.

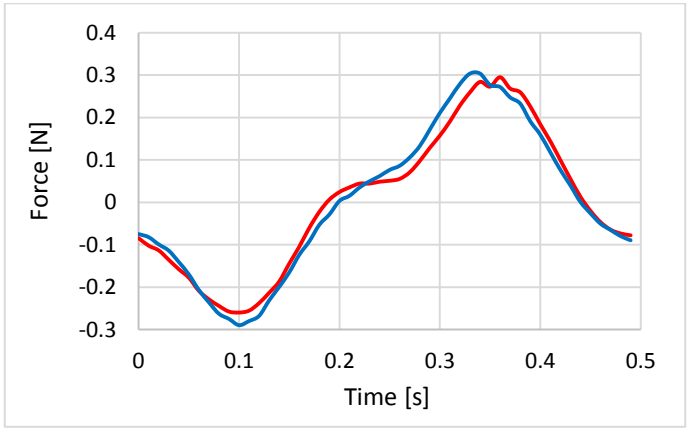

Figure 4.24: Lateral force in an oscillation cycle at 2 Hz: Red: freestream; blue: behind the fish.

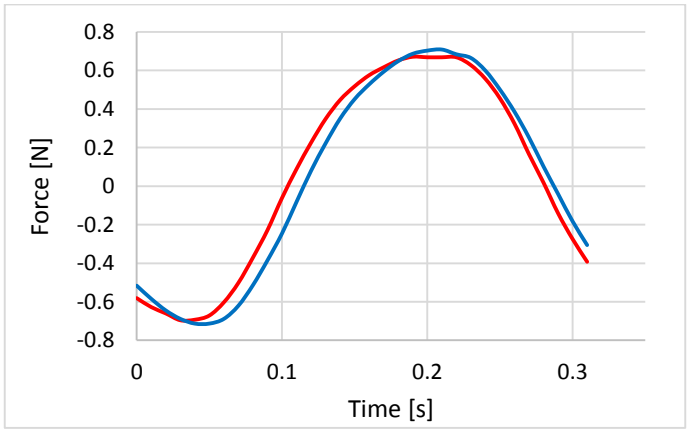

Figure 4.25: Lateral force in an oscillation cycle at 2 Hz: Red: freestream; blue: behind the fish.

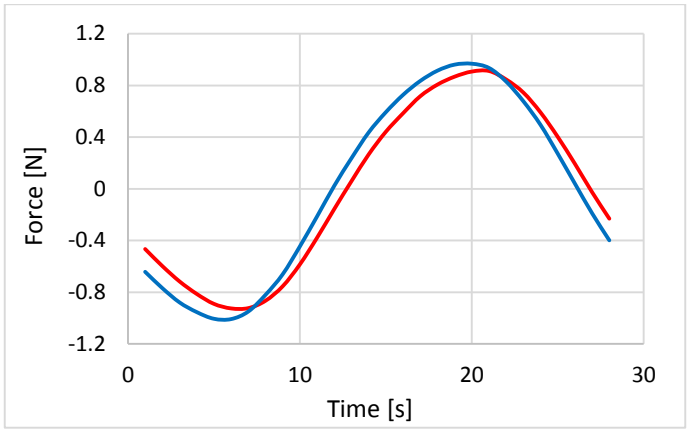

Figure 4.26: Lateral force in an oscillation cycle at 2 Hz: Red: freestream; blue: behind the fish.

Figure 4.24, 4.25 and 4.26 show the measured lateral force respectively at 2, 3 and 3.5 Hz. The curves closely resemble the lateral force trend displayed in Figure 4.3 and the maximum of the red curve, corresponding to the fin oscillating in a freestream, is near (even if lower) to the expected value of Table 4.2. Still a minor benefit is achieved by the fish model in front of the spinning foil.

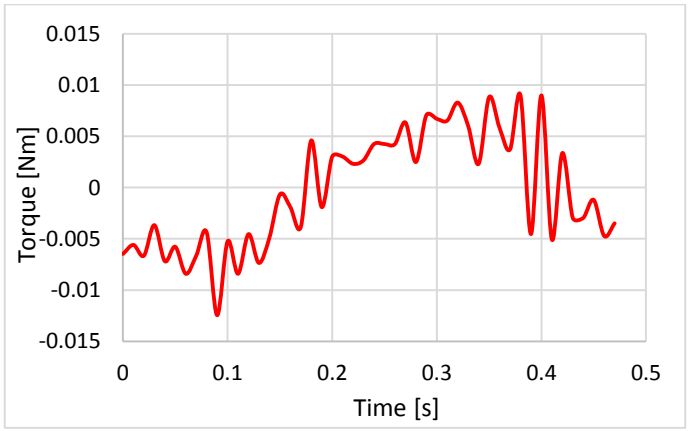

Figure 4.27: Propulsive torque in an oscillation cycle at 2 Hz in a freestream.

Figure 4.27 shows the propulsive torque acting on the fin at 2 Hz oscillation frequency. The measured values are severely affected by noise and therefor the curve is reported just for completeness, although the trend closely resemble the one showed in Figure 3.9, while the maximum value is near to the expected one.
The propulsive torque at 3 and 3.5 Hz are respectively showed in Figure 4.28 and 4.29. Noise still affects the measurement, most of all at the lower frequency. Still, the trends are correct

while the maximum values of the measured torque accectably approximate the expected ones of Table 4.2.

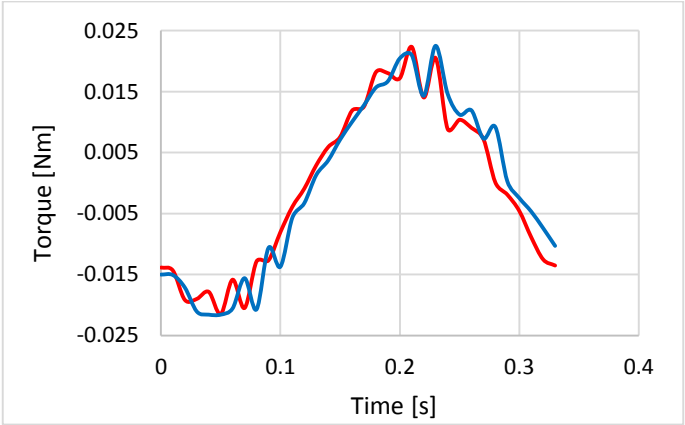

Figure 4.28: Propulsive torque in an oscillation cycle at 3 Hz. Red: freestream; blue: behind the fish.

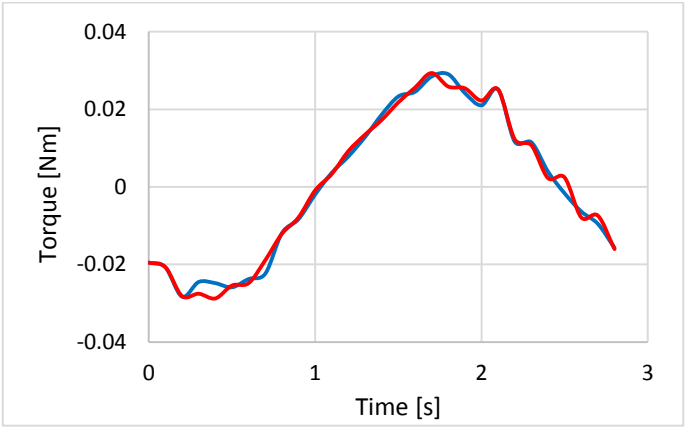

Figure 4.29: Propulsive torque in an oscillation cycle at 3.5 Hz. Red: freestream; blue: behind the fish.

In conclusion, the performed experimental tests have showed an acceptable agreement with the expected values of the propulsive forces and torques predicted by CFD analysis. Even if the frequency range has been narrower then the expected due to the deflections of the shaft, the measurements have been obtained around the maximum efficiency condition, expressed by the *Strouhal* number, which constitutes the region of highest interest in the present research.

Chapter 5.

Development of a multiphysics environment for biomimetic robots

5.1. Introduction

The design method employed in Chapter 3 to size the propulsive system of two *ostraciiform* swimming robots is based on a simple power balance: hydrodynamic drag power compared to propulsive power, where the latter is obtained as the work per time unit of the added mass torque acting on the fin, times a propulsive efficiency. The main advantage of the method is its simplicity and the possibility to size a vehicle in a parametric way. However, the procedure doesn't take into account the drag power of the hydrodyamic forces acting on the body of the robotic fish (it considers only the resistance force due to its frontal surface), nor the damping effect due to recoil. Furthermore, the propulsive torque acting on the fin is approximated by considering the added mass contribution only.
A more complete method is presented in this Chapter: here, the computational fluid dynamics characterization of the robot bio-inspired thruster, is integrated in a multi-body model, which accounts both for the vehicle mass distribution and for the hydrodynamic effects, like added mass and viscous damping, applied to the swimmer fore body. Multi-body techniques can be used to simulate the dynamics of biomimetic underwater robots, due to their rigid forebody and multi-joint robotic tails: indeed, their propulsive performance can be calculated under different kinematic conditions, i.e. thrusters undulating frequency, and the obtained data can be exploited to improve the vehicle design in terms of mass distribution. At the same time, the dynamic equations of the model can be coupled with trajectory planners and advanced control techniques in order to compute the effort required by the robot guidance system in order to perform a given mission. Furthermore, the multi-body model can be imported in a simulation environment (i.e. Simulink) suited to couple advanced control techniques to the dynamics equations.
The latter application is beyond the scope of the present dissertation. Indeed, the aim of the author here is to prove that the the long-lasting and thus off-line fluid dynamics simulations and their results can be integrated in a multi-body simulator, and that the provided results are reliable. CFD and multi-body simulation techniques can thus become the backbone of a framework usable to test the swimming performances of a given robot, optimize its internal mass distribution and propulsive system and also provide a detailed sizing method for a bio-inspired underwater robot possessing the "oscillating plate" or "flapping wing" architectures described in Chapter 2. Multi-body analysis is not applicable to the "travelling wave" desing style because the flexible bodies of such robots are more suited to finite elements simulation

techniques. Flexibility can be actually integrated in a multi-body analysis by using advanced software like ADAMS, developed by MSC. However, this extension is left to future work.
The following Sections will show how the multi-body model has been created by the author: the numerical predictions of Section 3.2, partially validated by the experimental tests of the previous Chapter, have been coupled to a well-known hydrodynamic model suited to AUVs underwater navigation at low speed. The results of the simulations are then presented as well as a further optimization suggested for the whole vehicle. Lastly, a sizign method, alternative to the preliminary design procedure detailed in Chapter 3, is presented in the last Section.

5.2 Framework development

Anderson adopted a multi-body technique to analyze the stability and manoeuvrability of the famous Vorticity Control Unmanned Undersea Vehicle (VCUUV) manufactured at Draper Laboratory [31]. A few years later, Hu *et al.* developed a simulator to study the autonomous navigation of a robotic fish [94]; simplified hydrodynamics models were proposed by the authors, and the presence of obstacles and sensor systems was taken into account. Likewise, Morgansen [95] applied the geometric non-linear control theory on the dynamic model of a free-swimming robotic fish in order to follow a given trajectory. A multi-body analysis was performed by Liu [93] to compute the swing of a fish body propelled by a two-joint robotic tail while in [96] they employed multi-body techniques to predict the propulsive performance of a bio-inspired underwater robot. Finally, the same method was employed by Wen [97] to study the kinematics of Body and Caudal Fin locomotion (BCF).
In those works, the authors adopted known analytic models, like those in [22-23], to express the propulsive forces genetated by the tails and fins, while here the same quantities have been computed by using the numerical predictions resulting from a CFD analysis.

5.2.1 Thruster characterization

As stated before, the numerical techniques allow to compute the force and torque coefficients in terms of a single dimensionless parameter, expressed by equation (3.3), which accounts both for the fin properties (geometry, motion) and for the whole vehicle kinematics as well (swimming velocity U). Thus, in order to characterize the propulsive performances of the biomimetic thruster of a swimming robotic fish, it is necessary to integrate the dimensionless predictions of a CFD simulation with a dynamic analysis of the whole vehicle in motion.
In Section 3.2, the propulsive forces and torque generated by an *ostraciiform* thruster, i.e the oscillating caudal fin, have been expressed as a function of the *Strouhal* number, particularly in the range [0.2 – 1.1], where the lowest value corresponds to a negative thrust generation and the largest to approximately a half of the maximum propulsive efficiency, as shown in Figure 3.2; in other words, the range identifies two opposite swimming conditions: minimum and maximum thrust generation, while the most efficient condition stands among them. The numerical analysis also provided the trends of the hydrodynamic forces and torque within an oscillation period, as a function of the fin angular position θ, expressed by (3.4), where θ_0 has been set equal to 14° while f is the foil oscillation frequency. Therefore, by means of data interpolation, the following expressions have been computed:

$$
\begin{aligned}
F_T &= \frac{1}{2}\rho_w U^2 S\,[(a_0 + a_1 St + a_2 St^2) + (b_0 + b_1 St + b_2 St^2)\sin(4\pi f t + \varphi_T)] \\
F_L &= \frac{1}{2}\rho_w U^2 S\,[\sin(2\pi f t + \varphi_L)] c_2 St^2 \\
M_Z &= \frac{1}{2}\rho_w U^2 Sc\;\,[\sin(2\pi f t + \varphi_Z)] d_2 St^2 \\
U^2 &= u^2 + v^2 + w^2 \\
St &= f\frac{2c\sin\theta_0}{U}
\end{aligned}
\tag{5.1}
$$

where F_T is the propulsive thrust, F_L is the lateral force and M_Z is the yawing torque; S is the fin area, ρ_w is the water density and the angles φ_T, φ_L, φ_Z are the relative phase differences between the sinusoidal functions used to approximate the symmetric trends of the propulsive forces and torque generated by the fin motion. Their values are reported in Table 5.1.
Equation (5.1) states that the amplitudes of the propulsive forces and torque depend from the *Strouhal* number squared. This property is consistent with the following consideration: the side pressure acting on the fin depends on the oscillation frequency squared, as confirmed by several fluid dynamics models [70].

	S	θ_0	φ_T	φ_L	φ_Z		
	0.036 m^2	14°	0.59	0.44	0.53		
a_0	a_1	a_2	b_0	b_1	b_2	c_2	d_2
-0.163	-0.026	3.604	-0.012	-0.359	8.952	51.81	33.01

Table 5.1: Geometric and dynamic parameters in equation (5.1).

5.2.2 Robot modelling

Figure 5.1 shows the body reference frame Σ_b, O_b - $x_b y_b z_b$, which is attached to the robot. The velocity of the origin O_b, with respect to the ground frame Σ_i, is expressed in the body frame Σ_b, by the vector $\boldsymbol{\nu}_1$ [98]:

$$
\boldsymbol{\nu}_1 = [u \quad v \quad w]^T = {}^{B}_{I}\mathbf{R}\,\dot{\boldsymbol{\eta}}_1 \tag{5.2}
$$

where $\boldsymbol{\eta}_1$ is the vector of the robot position coordinates in the ground frame Σ_i and ${}^{B}_{I}\mathbf{R}$ is the rotation matrix that expresses the transformation from the inertial frame Σ_i to the body-fixed frame Σ_b. In the nautical field, the rotation matrix in equation (5.2) is expressed in terms of the roll, pitch and yaw Euler angles. Finally, vector $\boldsymbol{\nu}_2$ represents the angular velocity of the robot with respect to Σ_i and is related to the Euler-angles and their derivatives by a Jacobian matrix:

$$
\boldsymbol{\nu}_2 = [p \quad q \quad r]^T = \mathbf{J}(\boldsymbol{\eta}_2)\dot{\boldsymbol{\eta}}_2 \tag{5.3}
$$

where $\boldsymbol{\eta}_2$ is the vector of the Euler-angles. As stated before, the *ostraciiform* swimming robot modeled in this Chapter by means of multi-body techniques consists of a rigid hull and an oscillating plate connected to the fore body through a revolute joint. Since almost all of the vehicle mass is due to its hull, the robotic fish has been approximated with its rigid fore body, subject to the hydrodynamic forces due to the thruster-fluid interaction. According to such hypothesis and to the usual Newton-Euler formulation, the dynamics of the robot can be described by the following equations:

$$\begin{aligned} m(\dot{u} - vr + wq) &= X \\ m(\dot{v} - wp + ur) &= Y \\ m(\dot{w} - uq + vp) &= Z \\ I_x\dot{p} + (I_z - I_y)qr &= K \\ I_y\dot{q} + (I_x - I_z)pr &= M \\ I_z\dot{r} + (I_y - I_x)pq &= N \end{aligned} \tag{5.4}$$

where m is the robot mass and I_x, I_y, I_z are the principal moments of inertia, computed under the hypothesis that the body frame Σ_b is coincident with the fore body central frame. Besides, in Figure 5.1, the axis of the body frame Σ_b have been labeled according to the nomenclature commonly adopted in the nautical field: particularly, the surge direction coincides with the longitudinal axis of the vehicle.

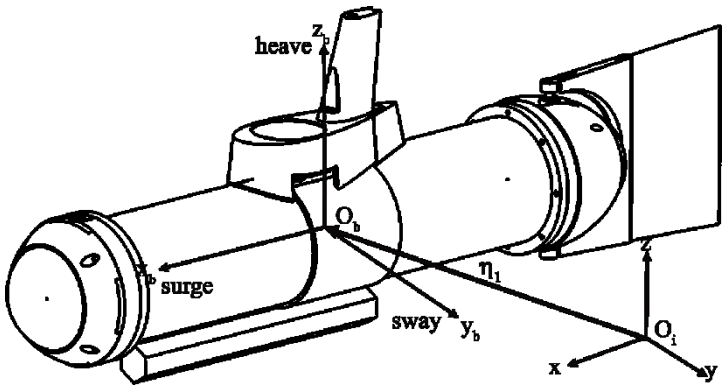

Figure 5.1: Ground and body reference frames Σ_i and Σ_b. The x_b, y_b and z_b axis of the body frame coincide with the surge (roll), sway (pitch) and heave (yaw) directions commonly used in marine environment and applicatications.

The right side of equation (5.4) accounts both for the propulsive forces and torques due to the fin motion and for the hydrodynamic effects on a rigid body moving in a fluid. A rigorous analysis of an incompressible flow would require the solution of the Navier-Stokes equations: indeed, the motion of an underwater vehicle moving in six degrees of freedom at high speed is generally non-linear and coupled. However, if the robot velocity is reasonably low, most

of the hydrodynamic effects have no significant influence on the resulting motion; moreover, if the vehicle features three planes of symmetry, then the terms in right side of equation (5.4) can be decoupled and linearized [98-99], leading to the following expression:

$$
\begin{aligned}
X &= -X_{\dot{u}}\,\dot{u} - (-Z_{\dot{w}}\,wq + Y_{\dot{v}}\,vr) - X_{u|u|}\,u|u| + F_T\cos\alpha_i - F_L\sin\alpha_i \\
Y &= -Y_{\dot{v}}\,\dot{v} - (Z_{\dot{w}}\,wp - X_{\dot{u}}\,ur) - Y_{v|v|}\,v|v| + F_L\cos\alpha_i + F_T\sin\alpha_i \\
Z &= -Z_{\dot{w}}\,\dot{w} - (-Y_{\dot{v}}\,vp + X_{\dot{u}}\,uq) - Z_{w|w|}\,w|w| \\
K &= -K_{\dot{p}}\,\dot{p} - (-Z_{\dot{w}} + Y_{\dot{v}})vw - \left(-N_{\dot{r}} + M_{\dot{q}}\right)qr - K_{p|p|}\,p|p| + \\
M &= -M_{\dot{q}}\,\dot{q} - (Z_{\dot{w}} - X_{\dot{u}})uw - \left(N_{\dot{r}} - K_{\dot{p}}\right)pr - M_{q|q|}\,q|q| + \\
N &= -N_{\dot{r}}\,\dot{r} - (-Y_{\dot{v}} + X_{\dot{u}})uv - \left(-M_{\dot{q}} + K_{\dot{p}}\right)pq - N_{r|r|}\,r|r| + M_{z,tot}
\end{aligned}
\tag{5.5}
$$

$$
M_{z,tot} = M_z + (F_L\cos\alpha_i + F_T\sin\alpha_i)\,L/2
$$

$$
\tan\alpha_i = \frac{v}{u}
$$

where the subscripts with the velocity derivatives belong to the added mass coefficients while the velocity subscripts refer to the damping coefficients. Table 5.2 summarizes the values of the constant coefficients in equation (5.5) for a cylinder with radius R, length L and mass m. Written as (5.5), the system can be actually integrated in time and the final average swimming velocity U effectively computed at different oscillation frequencies f. Regarding the angle α_i, Figure 5.2 shows the *ostraciiform* swimming robot presented in Chapter 3: here, the velocity vector $\boldsymbol{U}$ has been decomposed, with respect to the moving frame Σ_b, in its components u and v. Since the thrust force in *ostraciiform* locomotion is due to lift forces, it is always aligned with the freestream direction or, by applying the relative velocity theorem, to the swimming velocity. In the same way, the lateral force is normal to the thrust vector. Then, defined α_i as the angle between $\boldsymbol{U}$ and the surge axis, it is easy to project the forces as in system (5.5).

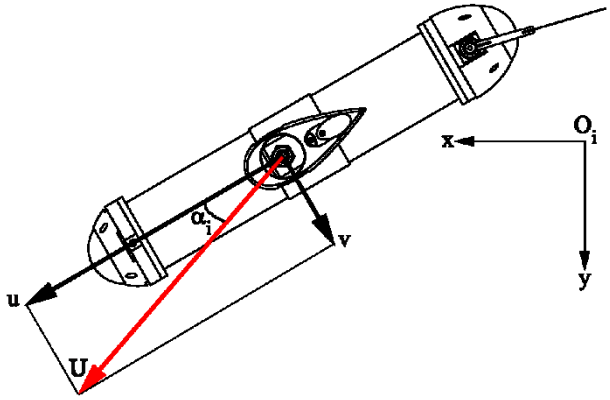

Figure 5.2: projections of the velocity vector $\boldsymbol{U}$ in the surge and sway directions of the moving frame.

$X_{\dot{u}}$	$Y_{\dot{v}}, Z_{\dot{w}}$	$K_{\dot{p}}$	$M_{\dot{q}}, N_{\dot{r}}$	$X_{u\|u\|}$	$Y_{v\|v\|}, Z_{w\|w\|}$
0.1 m	$\pi\rho_w R^2 L$	0	$\pi\frac{\rho_w R^2 L^3}{12}$	$\frac{\rho_w A_f c_{D,f}}{2}$	$\frac{\rho_w A_l c_{D,l}}{2}$
$K_{p\|p\|}$	$M_{q\|q\|}, N_{r\|r\|}$	A_f	A_l	$c_{D,f}$	$c_{D,l}$
0	$\frac{\rho_w A_l c_{D,l} L^3}{16}$	πR^2	$2\pi R$	0.5	[0.8 -1.2]

Table 5.2: Added mass and damping coefficient for a cylinder [98-99].

5.3 Multi-body analysis

The multi-body analysis has been performed by using MSC Adams View. The vehicle rigid fore body has been approximated with a 600 mm long cylinder having a 60 mm radius. As for the robot mass distribution, two separate contributions have been considered to compute the vehicle inertia moments: a constant component due to the hull, the onboard electronics, the actuators and the payload; a variable component due to the ballast rod fixed to bottom of the vehicle as shown in Figure 5.1. Although this element has a constant mass value, it can be split in two identical parts and then fixed to the hull in two specular positions with respect to the vertical plane of symmetry, i.e. the *sway-heave* plane, of the robotic fish. In this way, the moments of inertia I_y and I_z vary according to the ballast configuration, while the position of the center of mass remains unchanged. Those values have been calculated for five different ballast configurations and then introduced in the multi-body model by means of a dedicated Design Variable. As for the hydrodynamic effects, they have been integrated in the model as single-component forces and torques by means of Adams Function Builder: particularly, the various kinematic components of equation (5.5) have been multiplied by the coefficients stated in Table 5.2. The same procedure has been followed to model the propulsive forces and torques: here, the amplitudes have been expressed as a function of the *Strouhal* number as prescribed by the numerical predictions in equation (5.1).

Up to now, the author has focused on planar motion, meaning on the surge-sway plane. Thus, the multi-body model has been constrained by means of the planar joint shown in Figure 5.3. Attitude variations and depth-changing maneuvers will be introduced in the model as future work.

Figure 5.4 shows the analysis result for a straight forward navigation: the robot surge velocity is plotted as a function of time at different fin oscillation frequencies. Here, a constant speed is reached only on averages, because the thrust force varies with the fin angular position in an oscillation cycle. However, the multy-body analysis prove that a mean swimming velocity is reached when the propulsive force is balanced from the viscous resistance. It is worthy to observe that the *Strouhal* number computed when the robot has reached the regime speed is nearly constant regardless of the frequency variation. In other words, the maximum surge speed and the thruster oscillation frequency are linearly dependent. Those statements can be proved by considering the force balance in the surge direction: when the terms containing the velocity derivatives are neglegible, because the solution has almost reached its regime values,

and v is reasonably small due to an optimal mass distribution inside the vehicle, then the first line of system (5.5) states that:

$$-X_{u|u|}\, u|u| + F_T = 0$$
$$\frac{1}{2}\rho_w U^2 S\, \Pi^2(St^2) = \frac{\rho_w A_f c_{D,f}}{2}\, u|u| \tag{5.6}$$

where $\Pi^2(St^2)$ is a second order polynomial of St. By applying the aforementioned hypothesis, the velocity terms can be simplified and the resulting equation states that the regime *Strouhal* number is independent from the oscillating frequency of the thruster. However, even if the previous result is true and the propulsive efficiency (which is related to the St value as showed in Chapter 3) is independent from the oscillating frequency, the total efficiency still depends from the fin motion because the motor performances (which corresponds to the muscles of a biological swimmer) are strictly related to the spin velocity. This conclusion will be verified with experimental tests in future work.

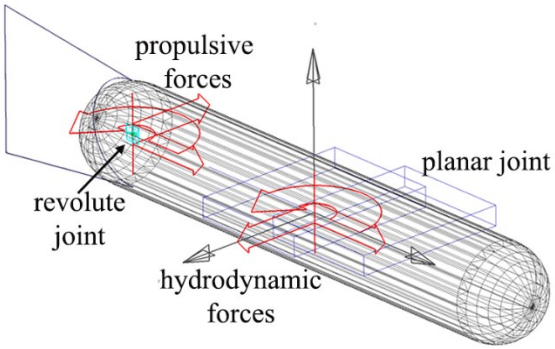

Figure 5.3: Multi-body model of the *ostraciiform* swimming robot, created on Adams VIEW.

Regarding the linear dependency of the maximal surge speed from the oscillation frequency, consider again equation (5.6): if the *Strouhal* number expression is substitued on its left side, the factor U^2 is simplified and the remaing terms states that:

$$u^2 \propto \Pi^2(f^2) \tag{5.7}$$

Where $\Pi^2(f^2)$ is a second order polynomial where the coefficients a_0 and a_1 are much smaller then a_2, as shown in Table 5.1.
Figure 5.5 shows the effect of the mass distribution: the highest value of the principal moment of inertia I_z is reached when the ballast is split in two parts, fixed at the opposite ends of the hull. The dashed line represents the robot oscillation amplitude (*recoil*) about the heave axis due to the propulsive torque $M_{z,total}$ of system (5.5): the diagram shows that the amplitude is reduced by one third as the moment of inertia increases as a function of the mass distribution. On the other hand, the continuous line of Figure 5.5 represents the maximum surge velocity

at *f* equal to 2 Hz: the diagram shows that the inertia variation due to the ballast configuration has a minor influence on the maximum speed reached by the vehicle [100].

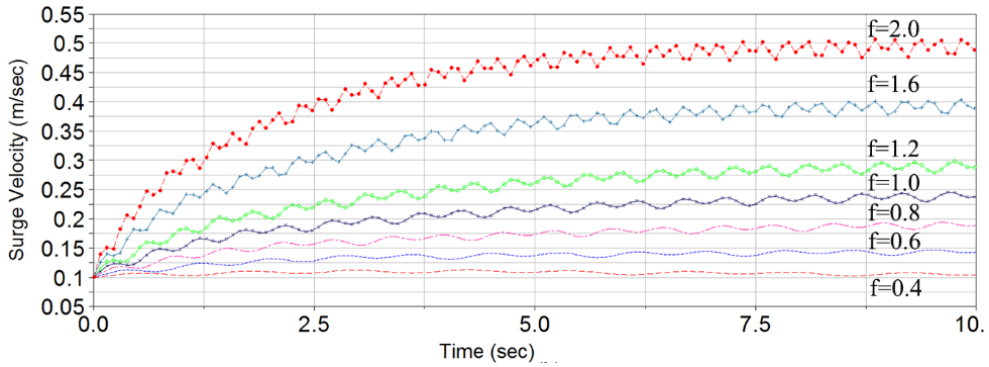

Figure 5.4: Multi-body analysis results. Surge velocity at different fin oscillation frequencies *f* [Hz].

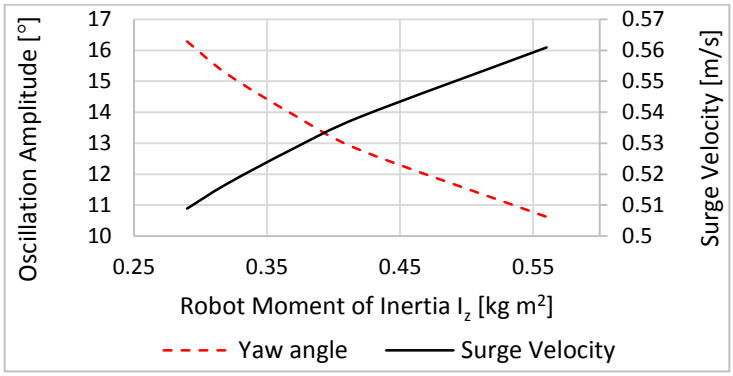

Figure 5.5: Multi-body analysis results. Effect of mass distribution on maximum surge velocity and heave oscillation amplitude (*recoil*) [100].

5.4 A sizing method for *ostraciiform* swimming robots

The multi-body analysis confirmed that the average swimming speed at 1.67 Hz oscillation frequency is about 0.4 m/s, corresponding to 0.5 BL/s. This value has been set as the target cruising speed for the designed ostraciiform swimming robot presented in Chapter 3. If the aforementioned frequency and regime velocity are inserted in the expression of the *Strouhal* number (3.3) together with the fin chord *c* and oscillation amplitude θ_0, the obtained result is about 0.41, close to the maximal efficiency condition corresponding to *St* equal to 0.42. This evidence has suggested the following sizing method, best suited to *ostraciiform* swimming robots, as it will be explained below, and outlined in Figure 5.6: as a first step, the required autonomy, stated in terms of mission duration, target speed and payolod description (onboard electronics, sensors, communication and positioning devices) must be properly stated. At the

same time, a navigation condition has to be chosen, like the maximum efficiency propulsion. In the second step, the forebody volume, necessary to house the payload and the battery pack as well as, together with the resulting mass and inertia distribution, are estimated. At the same time, the fin geometry is drawn by comparing the robotic fish with a natural swimmer of the same type (or possibly with a similar biomimetic underwater vehicle). Then, as the third step, a multi-body analysis of the robot is performed: the propulsive performances of the thruster, i.e. the drawn fin, are integrated in the multi-body model by interpulating the results obtained with a numerical analysis of the aforementioned propulsive system, as has been shown in the previous Section. Then, if the maximum efficiency navigation condition is achieved for some oscillation frequency, at the target speed, the actuation system design and optimization can be performed: the required motor torque is computed, at the obtained frequency, by applying the propulsive forces predicted by the CFD analysis, to the driven member of the transmission system, or directly to the motor if a direct drive is employed. At the same time, a torsional spring is sized, according to the optimization procedure presented in Chapter 3, in order to save the negative power fraction and increase the vehicle autonomy. On the other hand, if the results of the multi-body-CFD analysis does not consent to achieve the optimal navigation condition, then the fin and possibly the robot frontal section must be redrawn again until the requirements are satisfied by the designed propulsion system.

The main advantage of this method is the possibility to exploit the expensive and long-lasting CFD analysis, by integrating their results in the fast multi-boby simulations. In other words, it is sufficient to perform the complex numerical predictions only in few, representative cases. Then, their results can be integrated in a large number of multi-body simulations.

As stated before, the present method best suits to *ostraciiform* swimming robots because their forebody constitutes about 80% of the robot total length and more than 90% of the total mass. This feature allows to approximate the hull as a cylinder, a volume possessing a high degree of simmetry, and apply the hydrodynamic loads only to the vehicle forebody. Furthermore, the kinematic structure of this particular class of robotic fish is simple when compared to the other architectures described in Chapter 2. The possibility to extend the presented method to the “flapping wings” of *thunniform* swimming robots is left to future work.

Finally, further computational fluid dynamics analysis will allow to predict the influence of the rigid forebody recoil to the propulsive performances of the biomimetic thruster, both for *ostraciiform* and *thunniform* locomotion. Once the propulsive forces and torques would have been updated to the new boundary conditions, more accurate multi-body simulations would be performed, both in straight-forward navigation conditions and while manoeuvring.

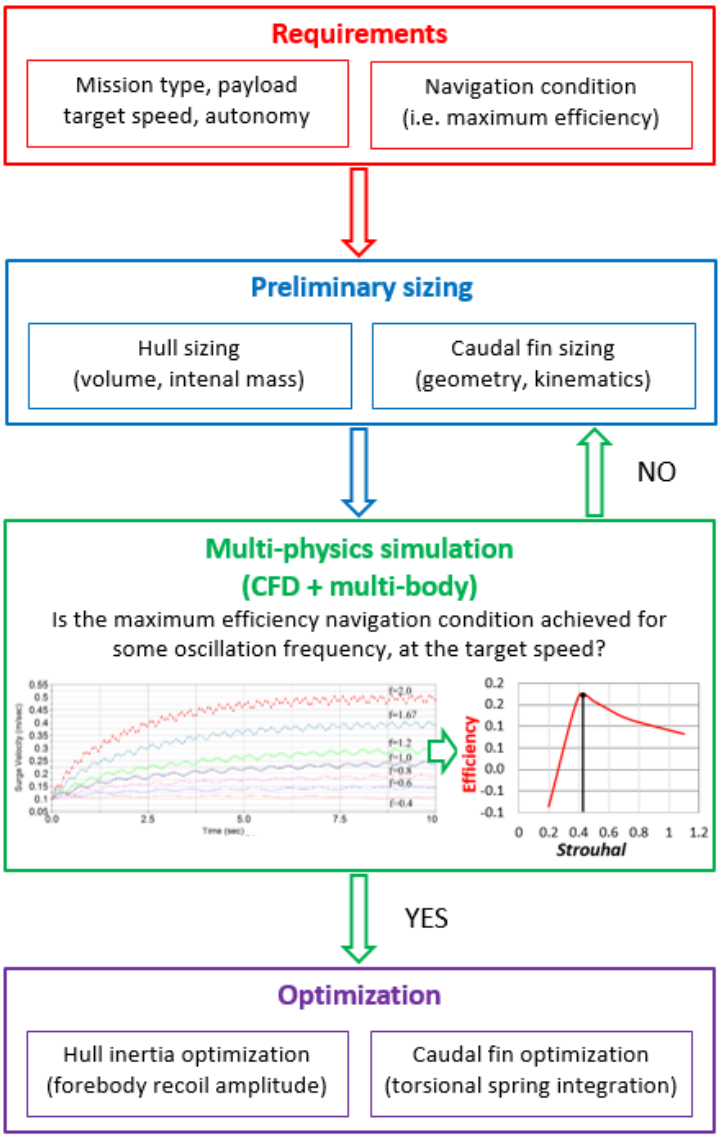

Figure 5.6: Outline of the sizing method proposed for ostraciiform swimming robots.

Chapter 6.

A transmission mechanism for *thunniform* locomotion

6.1. Introduction

As stated in Chapter 3, the necessity to pursue the highest possible propulsive efficiency in order to maximize the robot autonomy has driven the author of the present paper to improve the robotic fish design by moving from *ostraciiform* to *thunniform* locomotion. Indeed, even if the driving system has been optimized by the implementation of the proposed transmission mechanism, the propulsive efficiency of *ostraciiform* locomotion is still too low – the highest value obtained by means of the CFD analysis described in Section 3.2 in about 17% - if the final purpose is to replace the conventional screw-propellers employed on AUVs with a more efficient bio-inspired thruster.
In *thunniform* locomotion, the rigid caudal fin (also called "lunate") performs a combination of pitching and heaving motions [12], tracing an undulating path as the fish moves forward in order to adjust the fin angle of attack with respect to its trail and thus avoid flow separations in order to obtain the maximal thrust during the whole of a beat cycle. The fin trajectory and orientation has been already displayed in Figure 2.15: from a kinematic point of view, the fin motion can be described as a roto-translation: both the rotatory and translatory components of the resulting motion follow harmonic laws sharing the same frequency and characterized by a constant phase difference between them.
Many *thunniform* swimming robots have been presented in Chapter 2, most of them designed according to the "flapping foil" architecture. This class of robotic fish is characterized by an anterior rigid head and a piecewise flexible tail driven by an N-joint serial mechanism. Here, each revolute joint of the assembly is directly actuated by a dedicated servomotor installed on the links forming the kinematic chain. Hence, in order to comply with the required roto-translatory motion of the fin, each link must oscillate following an harmonic law. Position control of the servomotors is then required also to maintain the constant angular position difference between the links. Finally further issues may arise since each motor installed along the serial chain must be properly sealed, while leading to an increase of the structure inertia and encumbrance.
According on the previous discussion, the author of the present dissertation has designed a transmission mechanism that converts the continuous rotation, at constant angular speed, of a single drive in the harmonic roto-translation of the system output, i.e. the robot thruster, shaped like a caudal fin. The phase difference between the rotary and translational sinusoidal motion laws is maintained constant by a kinematic constraint. Furthermore, the stated phase

value can be properly set by means of an off-line regulation, in order to test the performances of the *thunniform* thruster in different kinematic configuration and thus measure the maximal efficiency during a beat-cycle. When compared to a N-joint serial mechanism actuated by servomotors, the inertia and encumbrance of the proposed solution are reduced because the transmission actuator is installed on the robot frame, while waterproofing issues are minimal because a single motor needs to be sealed [101].
The first part of this Chapter shows the numerical analysis performed on a roto-translating foil, which will be called "the flapper" in the following. Computational fluid dynamics results have allowed to identify the relationship between the kinematic coefficients characterizing the motion of a flapping foil and the corresponding propulsive performances. The second part of this Chapter is dedicated to the functional analysis of the transmission mechanism, by using both analytic models and multi-body techniques. Finally, the last Section shows the physical prototype of the proposed solution and briefly discuss results and future work.

6.2 CFD analysis of a flapping thruster

The motion law of a flapping foil can be described by the following expression:

$$\begin{aligned} s(t) &= s_0 \cos(2\pi f t) \\ \alpha(t) &= \alpha_0 \cos(2\pi f t + \Delta) \end{aligned} \tag{6.1}$$

where angle α quantifies the rotation of the foil while s is its translation; then, α_0 and s_0 are the amplitudes of the harmonic functions in (6.1), f is their common frequency and Δ is the phase difference between the two components of the flapping motion, Figure 6.1.

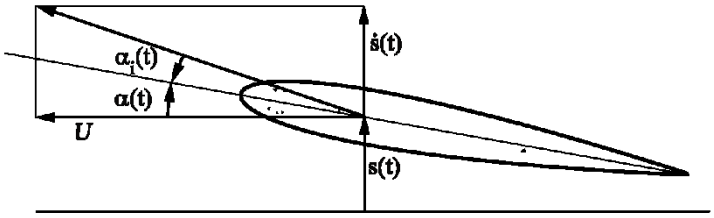

Figure 6.1: Kinematics of a flapping foil. Translation component *s* and rotation component *α*.

When dealing with *ostraciiform* locomotion, the thruster motion law depends from only two parameters: oscillation amplitude and frequency. Therefore, a numerical investigation on the propulsive performances of an *ostraciiform* thruster, requires a small number of simulations where the aforementioned parameters vary whitin a prescribed range. This method has been followed to perform the numerical prediction described in Section 3.2.
In *thunniform* locomotion, the flapper kinematics depends from four parameters: rotation and translation amplitude, frequency and phase difference of the associated harmonic functions. A fifth parameter is the position of the trace of the rotation axis along the foil chord, as shown in Figure 6.1. Therefore, a large campaign of numerical analysis is required to investigate the relative importance of the aformentioned quantities on the flapper propulsive performances.

A similar but less extensive analysis has been performed by Triantafyllou in [102], where the influence of the *Strouhal* number and the rotation amplitude has been investigated by means of an experiemental setup.
In the present work, the fluid dynamics simulations have been performed using the same code already adopted for *ostraciiform* locomotion, meaning the in-house developed research code MIGALE, whose characteristics have been reported in Chapter 3. The same strategy already adopted to predict the propulsive forces generated by an oscillating foil, has been employed here: particularly, computational time has been largely reduced by replacing a dynamic mesh buondary condition with a simple roto-translation of the mesh reference frame, where the required phase difference between the components of the resulting motion can be opportunely set. In order to save time, the analysis have been run by using a multi-core parallel simulation approach; particularly, the solution of the flow surrounding a flapping foil has been computed by 16 cores working in parallel on as many mesh partitions.
The first set of numerical simulations has regarded the influence of the *Reynolds* number on the flapper propulsive performances. The aforementioned dimensionless parameter has been varied between $6 \cdot 10^4$ and $6 \cdot 10^5$, which coincides with the swimming range of a robotic fish of small or medium size, like those presented in Chapter 2. For example, DORI swims at *Re* equal to 10^5. On the other hand, all the other parameters have been kept constant, meaning the motion amplitudes, the phase difference, the freestream velocity, the position of the rotation axis and finally the *Strouhal* number. Regarding *St*, since expression (3.3) doesn't account for the fin translation, the original definition (2.2) of *St* is adopted for *thunniform* locomotion, where the wake width is commonly approximated with the tail-beat peak-to-peak amplitude, meaning twice the maximum displacement of the fin trailing edge.
Table 6.1 summarizes the values of the parameters in the first set of numerical analysis and their results: the predicted propulsive efficiency and thrust coefficient as a function of the *Reynolds* number.

Strouhal	α_0	s_0	Δ	R.A.	*U*
0.2	20°	1	75°	0%	10

Reynolds	$6 \cdot 10^4$	$1.8 \cdot 10^5$	$3 \cdot 10^5$	$6 \cdot 10^5$
Efficiency	0.677	0.695	0.701	0.704
Thrust	0.258	0.264	0.265	0.267

Table 6.1: Propulsive efficiency and thrust coefficient as a function of the Reynolds number.

The geometric and kinematic parameters in Table 6.1 are expressed in a dimensionless form, meaning that they have been divided by the fin chord length. For example, a unitary value of s_0 means that the translation amplitude is equal to the fin chord. In the same way, the position of the rotation axis along the chord is expressed as the distance from the leading edge of the trace of the rotation axis, divided by the chord length. Finally, freestream velocity *U* is equal to the stated number of chord length per unit time.
Table 6.1 shows that both the efficiency and thrust coefficient faintly depend from the value of the *Reynolds* number as already observed for *ostraciiform* locomotion. In other words, the numerical predictions confirmed that, past the critical *Re* for a flapping foil, the flow around

the moving fin becomes turbolent and the propulsive forces generated by the oscillating foil stabilize close to the regime values. Still, a slight growing trend is observed both for the thrust and for the efficiency, as the *Reynolds* number increases. Again, this is physical: indeed, the higher *Re*, the stronger is the turbolent boundary layer sorrounding the fin, thus preventing that separation occurs while keeping the flow attached to the moving wall even at the highest incidence angles. The lower dependency from the *Reynolds* number of the performances of a flapping foil, once the critical value has been passed, allows to apply the similitude principle as shown in Chapter 4. In other words, the propulsive forces computed on a flapping thruster can be extended to a scale model of the same type, provided that the condition on the minimal *Re* value is satisfied.
The second set of numerical analysis has regarded the sensibility of the propulsive efficiency and thrust coefficient from the rotation amplitude α_0. Here, the *Reynolds* number has been set constant to $3 \cdot 10^5$ in order to obtain a fully developed turbolent flow; in the same way, all the other parameters have been maintained constant. Particular attention has been reserved to the *Strouhal* number: since the displacement of the fin trailing edge grows with the rotation amplitude, frequency *f* in expression (2.2) must be accordingly reduced in order to maintain *St* constant. Table 6.2 details the value of the parameters adopted in the simulations and their results, while Figure 6.2 shows the trends of the propulsive efficiency and thrust coefficient as a funcion of the fin rotation amplitude.

Strouhal	s_0	Δ	R.A.	*U*	*Reynolds*
0.2	1	90°	0%	10	$3 \cdot 10^5$

α_0	1°	5°	10°	15°	20°	25°
Efficiency	0.532	0.666	0.725	0.757	0.759	0.633
Thrust	0.454	0.463	0.389	0.295	0.187	0.070

Table 6.2: Propulsive efficiency and thrust coefficient as a function of the rotation amplitude. Parameters value are indicated in the first two rows of the table.

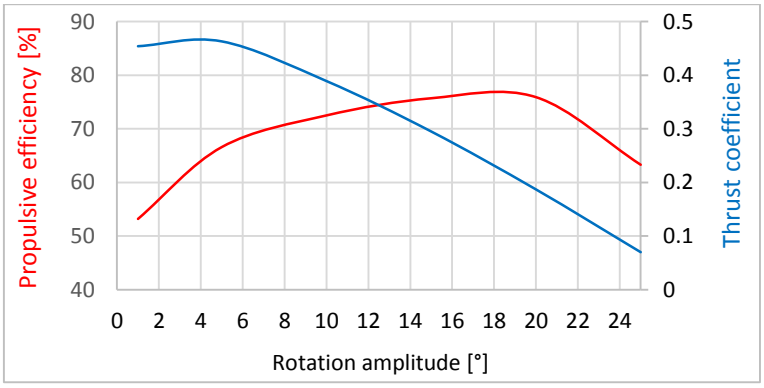

Figure 6.2: Propulsive efficiency and thrust coefficient as a function of the rotation amplitude.

Figure 6.2 shows that the optimal rotation amplitude is comprised between 18 and 19 degrees, at least for what concerns the propulsive efficiency. The presented trends closely resemble those in Figure 3.1 regarding *ostraciiform* locomotion, although the curves are translated in the positive ordinate direction.
The third set of numerical simulations has regarded the sensibility of the efficiency and thrust coefficient from the *Strouhal* number, at four different values of the translation amplitude s_0.

s_0	α_0	Δ	R.A.	U	*Reynolds*
0.75	15°	90°	0%	10	$3 \cdot 10^5$

Strouhal	0.1	0.2	0.3	0.5	0.7
Efficiency	0.236	0.709	0.614	0.435	0.256
Thrust	0.006	0.288	0.756	2.238	3.806

Table 6.3 a: Propulsive efficiency and thrust coefficient as a function of *St* at s_0 equal to 0.75.

s_0	α_0	Δ	R.A.	U	*Reynolds*
1	15°	90°	0%	10	$3 \cdot 10^5$

Strouhal	0.1	0.2	0.3	0.5	0.7
Efficiency	0.363	0.752	0.656	0.415	0.254
Thrust	0.01	0.321	0.833	2.108	3.509

Table 6.3 b: Propulsive efficiency and thrust coefficient as a function of *St* at s_0 equal to 1.

s_0	α_0	Δ	R.A.	U	*Reynolds*
1.25	15°	90°	0%	10	$3 \cdot 10^5$

Strouhal	0.1	0.2	0.3	0.5	0.7
Efficiency	0.439	0.782	0.678	0.373	0.242
Thrust	0.013	0.350	0.902	1.969	3.393

Table 6.3 c: Propulsive efficiency and thrust coefficient as a function of *St* at s_0 equal to 1.25.

s_0	α_0	Δ	R.A.	U	*Reynolds*
1.5	15°	90°	0%	10	$3 \cdot 10^5$

Strouhal	0.1	0.2	0.3	0.5	0.7
Efficiency	0.485	0.803	0.669	0.332	0.220
Thrust	0.016	0.374	0.957	1.834	3.164

Table 6.3 d: Propulsive efficiency and thrust coefficient as a function of *St* at s_0 equal to 1.5.

Tables 6.3 (a) – (d) details the values of the parameters adopted in the simulations and their results, while Figure 6.3 shows the trends of the efficiency and thrust coefficient as a function of the *Strouhal* number and fin translation amplitude. Again, the *Reynolds* number has been set constant to $3 \cdot 10^5$ in order to obtain a fully developed turbolent flow, while the rotation amplitude has been fixed to 15°, which represents a good compromise between the optimal values displayed in Figure 6.2.

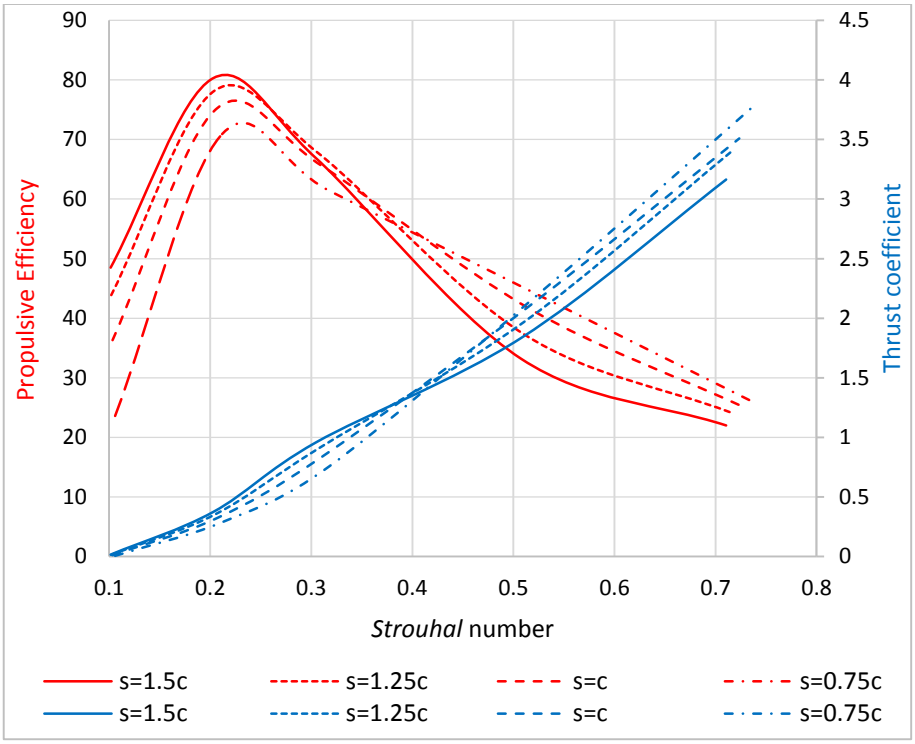

Figure 6.3: Propulsive efficiency and thrust coefficient as a function of the Strouhal number at four different translation amplitudes [0.75; 1; 1.25; 1.5].

By observing Figure 6.3, it results clear that the greater s_0, the higher the efficiency, at least when *St* is lower than about 0.35. A possibile explanation of this behaviour can be formulated by computing the instantaneous angle of attack α in terms of the kinematic parameters of Figure 6.1:

$$\alpha_i(t) = \alpha(t) - \tan^{-1}\left(\frac{\dot{s}(t)}{U}\right) \tag{6.2}$$

In Chapter 3, it has been observed that the propulsive efficiecy of an *ostraciiform* thruster is maximal when the attack angle is small enough to prevent flow separation occurring near the fin leading edge. Past the optimal value of *St*, the oscillation frequency becomes too high for

the flow to remain attached to the moving fin: then separation occurs, which cause the thrust force to rise slower than the lateral component, resulting in an efficiency reduction. A similar behaviour can be observed in *thunniform* locomotion, although – as shown by equation (6.2) - the presence of the translation velocity adjusts the fin total angle of attack. However, as *St* rises, the term containing the derivative of the heave component $\dot{s}$, which is proportional to the oscillation frequency times the translation amplitude, rise in turn, until the resulting angle of attack become so large that separation occurs, generating an efficienct drop despite thrust is still rising, as also observed on *ostraciiform* locomotion. This trend would explain why – past a certain value of *St*, the curves corresponding to a lower translation amplitude ($s_0 = 0.75$ or 1) have an higher efficiency than the other ($s_0 = 1.25, 1.5$).
The fourth set of CFD analysis has regarded the sensibility of the propulsive efficiency and thrust coefficient from the phase difference Δ between the rotation and translation motion laws of the fin. Still, the *Reynolds* number has been set constant to $3 \cdot 10^5$ in order to obtain a fully developed turbolent flow, while *St* has been fixed close to the optimal value; in the same way, all the other parameters have been maintained constant.

Strouhal	s_0	α_0	R.A.	*U*	*Reynolds*
0.2	1	15°	0%	10	$3 \cdot 10^5$

Δ	75	80	85	90	95
Efficiency	0.726	0.738	0.749	0.757	0.763
Thrust	0.275	0.280	0.286	0.295	0.306
Δ	100	105	110	115	120
Efficiency	0.767	0.767	0.765	0.76	0.751
Thrust	0.318	0.332	0.348	0.365	0.384

Table 6.4: Propulsive efficiency and thrust coefficient as a function of the phase difference between the rotation and translation components of the flapping motion.

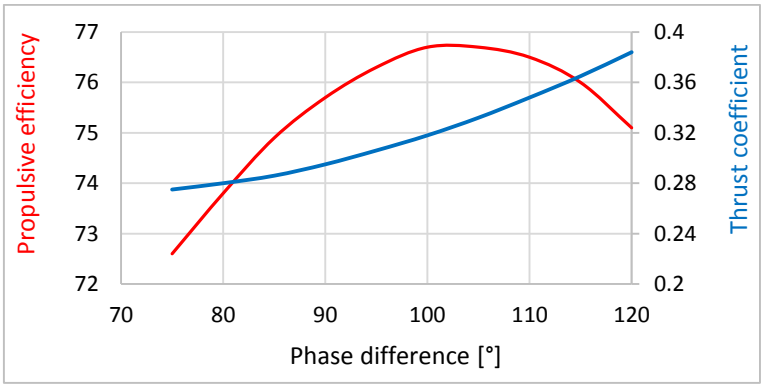

Figure 6.4: Curves of the propulsive efficiency and thrust coefficient as a function of the phase difference between the rotation and translation components of the flapping motion.

Tables 6.5 details the values of the kinematic parameters in the simulations and the results of the latter, while Figure 6.3 shows the trends of the propulsive efficiency and thrust coefficient as a function of the phase difference Δ. It results that the optimal value of the latter belongs to the interval [100-110°]. These values are 15°-20° larger that those found in litterature about the RoboTuna. However, the efficiency shows a quite constant trend past Δ equal to 60° and before Δ equal to 140°, while outside this last range the curve falls quickly to lower values. This behaviour may depend from the type of the foil, here a NACA 0015 has been used, and it will be investigated in future analysis.
The last set of numerical analysis regarded the sensibility of the foil propulsive performances from the position of the rotation axis along the fin chord. Table 6.5 and Figure 6.5 show the trends of thrust and efficiency as a funcion of the aforementioned pivot point position. Here, positive values of A.R. indicate a point downstream from the leading edge, meaning inside the foil, between its leading and trailing edge; on the other hand, a negative A.R. indicates a point upstream from the fin leading edge.

Strouhal	s_0	α_0	Δ	*U*	*Reynolds*
0.2	1	20°	105°	10	$3 \cdot 10^5$

A.R	-150	-100	-75	-50	-25	5
Efficiency	0.678	0.723	0.748	0.770	0.786	0.801
Thrust	0.169	0.174	0.183	0.195	0.211	0.243
A.R.	15	25	33	40	50	60
Efficiency	0.801	0.802	0.803	0.803	0.802	0.801
Thrust	0.243	0.252	0.26	0.266	0.276	0.286

Table 6.5: Sensitivity to the position along the chord of the trace of the rotation axis. Positive values of A.R. refer to points downstream from the leading edge, while negative values refer to point upstream from the leading edge.

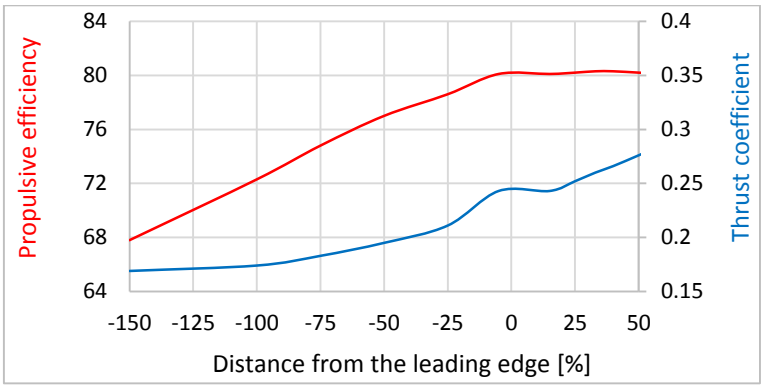

Figure 6.5: Propulsive efficiency and thrust coefficient as a function of the position along the chord of the trace of the rotation axis.

The trends shown in Figure 6.5 show that the propulsive efficiency is maximal when the foil rotation axis is placed between 33% and 40% of the chord, as confirmed by litterature [24]. Figure 6.5 shows the thrust coefficient decreases as the rotation axis moves upstream from the leading edge: this is consinstend with the observation regarding the rotation amplitude. Indeed, if the pivot point moves backwards but α_0 remains constant, the global effect on the fin trailing edge is to increase its peak-to-peak amplitude in a tail-beat; this factor has been considered in order to mantain constant the *Strouhal* number in this set of numerical analysis. However, even with a constant *St*, a rise of the peak-to-peak amplitude results in an apparent increase of the rotation amplitude, with a corresponding decrease of the thrust force as shown in Figure 6.2.

6.3 Functional design of a flapping mechanism

The performed numerical analysis provided great insight on the propulsive performances of a flapping foil. The superiority of *thunniform* locomotion compared to the *ostraciiform* mode is obvious: besides the maximum efficiency values, which is nearly 80% for a roto-translating fin compared to the 17% of pure oscillation, it is witnessed also by plotting the trend of the thrust force in a cycle. In Figure 4.3, the author has shown that the propulsive force generated from an *ostraciiform* thruster is partially negative inside an oscillation cycle, resulting in a lower value of the mean thrust force. On the contrary, the corresponding curve for a flapping foil, which is shown in Figure 6.6 at three difference values of the phase difference Δ, has always positive values, except for a minor part of the curve at Δ = 75°, which disappears for greater values of the phase difference.

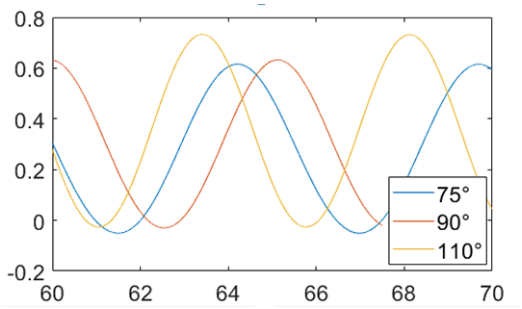

Figure 6.6: Thrust force in a flapping cycle at three different values of the phase difference Δ between the rotation and translation components of the resulting motion.

The possibility to exploit the superior propulsive performances of *thunniform* locomotion has driven the author to improve the transmission mechanism designed for an oscillating foil, in order to generate an harmonic roto-traslation. The solution presented in the following has the same layout of a 2R serial mechanism, as shown in Figure 6.7. Here, revolute joint R_1 connects link 1 to the robot frame, while R_2 connects links 1 and 2: each joint is actuated by the spatial-cam kinematic joint presented in Chapter 3. Then, the driven member C_1 of the first joint corresponds to link 1 of the 2R mechanism, while driven member C_2 of the second

joint acts as link 2 and coincides with the whole transmission output. A single motor installed on the robot frame drives both joints: in other words, both driving disks A_1 and A_2 of the spatial-cams are connected to the motor shaft. In this way, both A_1 and A_2 spin with the same constant angular velocity. However, in order to allow the motor shaft to follow link 2 during its rotation around revolute joint R_1, the shaft itself must bend around R_1 while rotating. This means that the shaft must be flexible in any direction contained in its section plane and stiff in the torsional direction. In order to satisfy these requirements, the driving shaft is composed by two rigid parts connected by a flexible joint in the proximity of revolute joint R_1, as shown in Figure 6.7. Finally, driving disk A_2 is rotated by a known quantity δ around the driving shaft with respect to driving disk A_1. This angular displacement is set when the transmission systems is assembled and is responsible of the phase shift between the translation and rotation motions of the fin.

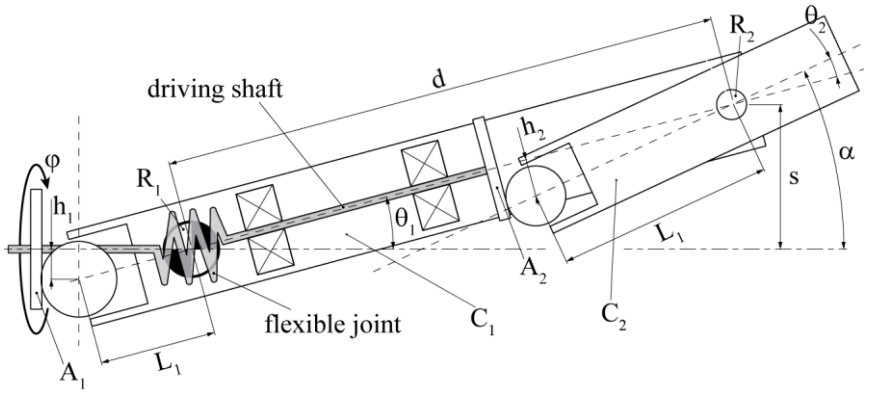

Figure 6.7: Functional scheme of the proposed transmission mechanism [101].

If the ratios between the geometric parameters h_1/L_1 and h_2/L_2 in Figure 6.7 are reasonably smaller than one, the spatial-cam joint output angles θ_1 and θ_2 can be approximated by the following expressions:

$$\begin{aligned} \theta_1 &\approx \frac{h_1}{L_1}\cos(\varphi) = \lambda_1 \cos\varphi \\ \theta_2 &\approx \frac{h_2}{L_2}\cos(\varphi+\delta) = \lambda_2 \cos(\varphi+\delta) \end{aligned} \tag{6.3}$$

where λ_1 and λ_2 are the functional dimensionless parameters characterizing the spatial-cam joints. The translation displacement s and the rotation angle α of the transmission output can then by be expressed by means of equation (6.3) as follows:

$$\begin{aligned} \alpha &= \theta_1 + \theta_2 = \lambda_1 \cos\varphi + \lambda_2 \cos(\varphi+\delta) \\ s &= d \sin\theta_1 = d \sin(\lambda_1 \cos\varphi) \approx d\lambda_1 \cos\varphi \end{aligned} \tag{6.4}$$

where d is the distance between revolute joints R_1 and R_2. The approximation in the final expression of s is valid because λ_1 is chosen sufficiently smaller than one as stated before. Expression (6.4) can be rearranged in order to show that the oscillation angle α and the translation displacement s of the transmission output are expressed by the same harmonic function, with different amplitudes but equal frequencies and with a constant phase difference between the arguments of the cosine functions:

$$\begin{aligned} s &= s_0 \cos\varphi \\ \alpha &= \alpha_0 \cos(\varphi + \Delta) \\ \varphi &= 2\pi f t \end{aligned} \tag{6.5}$$

where s_0 and α_0 are the aforementioned amplitudes while φ is the driving shaft rotation angle and f is its constant rotation frequency. The expressions of α in equation (6.4) and (6.5) can be equated and transformed by using trigonometric formulas:

$$\begin{aligned} \lambda_1 \cos\varphi + \lambda_2 \cos(\varphi + \delta) &= \alpha_0 \cos(\varphi + \Delta) \\ (\lambda_1 + \lambda_2 \cos\delta)\cos\varphi - (\lambda_2 \sin\delta)\sin\varphi &= (\alpha_0 \cos\Delta)\cos\varphi - (\alpha_0 \sin\Delta)\sin\varphi \end{aligned} \tag{6.6}$$

It results:

$$\begin{aligned} \lambda_1 + \lambda_2 \cos\delta &= \alpha_0 \cos\Delta \\ \lambda_2 \sin\delta &= \alpha_0 \sin\Delta \end{aligned} \tag{6.7}$$

Finally, equation (6.8) can be rearranged to express the relative rotation δ between driving disks A_1 and A_2 as a function of the desired phase difference Δ between the harmonic functions of α and s:

$$\tan\delta = \frac{\alpha_0 \sin\Delta}{\alpha_0 \cos\Delta - \lambda_1} \tag{6.8}$$

Equation (6.9) shows that once a desired value of the rotation amplitude α_0 and the phase difference Δ are chosen according to the output system requirements, namely the motion of biomimetic thruster connected to the transmission mechanism, the relative rotation angle δ can be properly set. Please also note that the value of δ depends from the geometric parameters h_1 and L_1 of the first spatial-cam joint. As it will be showed in the next Section, the choice of those parameters is constrained by the mechanical properties of the flexible joint that connects the rigid parts of the driving shaft displayed in Figure 6.7.

6.4 CAD model and prototype of the flapping mechanism

Figure 6.8 shows the CAD model of the devised transmission system: the flat plate connected to the driven member C_2, which coincides with the system output member, represents the biomimetic thruster, particularly a caudal fin, of a *thunniform* swimming robot. The displayed

prototype has been sized according to the following considerations: the rotation amplitude α_0 is equal to 16°, a value chosen according to the numerical predictions showed in Section 6.2. Furthermore, the value of λ_1 is set by the mechanical properties of the flexible joints installed on the driving shaft: in fact, the maximal axial misalignment admitted by commercial flexible joints in order to maintain negligible torsional deformations is normally a few degrees. Particularly, the component chosen for the displayed CAD model can rotate up to 6 degrees due to bending. Then, according to equation (6.3), this value is equal to the rotation amplitude of the first spatial-cam joint, which is approximated by the ratio $h_1/L_1 = \lambda_1$. Once the former parameter is chosen, the translation amplitude s_0 depends only on the distance d between revolute joints R_1 and R_2.

$$s_0 = d\lambda_1 \tag{6.9}$$

Therefore, distance d can be properly chosen on the basis of the desired value of s_0 expressed as a multiple of the chord length according to the numerical predictions. Regarding the phase difference, Δ has been fixed to $\pi/2$ in the proposed prototype. However, as displayed in Figure 6.8, the proposed transmission system allows to set the relative rotation δ between driving disks A_1 and A_2 by means of an offline regulation: particularly, driving disk A_2 can be easily rotated in the desired position once removed the grab screw used to tight the disk to its driving shaft. The value of δ is calculated as a function of Δ by means of expression (6.8). As it concerns the geometric parameters of the second cam joint h_2 and L_2, equation (6.7) can be rearranged again to obtain the value of λ_2. In fact, it results:

$$\lambda_2^2 = \lambda_1^2 + \alpha_0^2 - 2\alpha_0\lambda_1 \cos\Delta \tag{6.10}$$

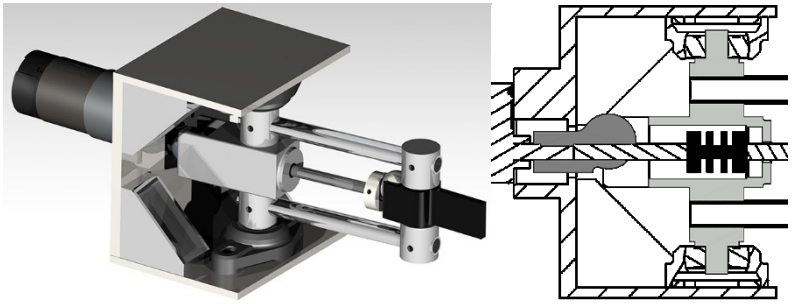

Figure 6.8: CAD model of the proposed flapping mechanism.

λ_1	h_1	L_1	λ_2	h_2	L_2	d	s_0	α_0	Δ	δ
0.1	4	40	0.316	5	16	100	10	16°	90°	-111°

Table 6.6: Geometric parameters of the CAD prototype. All lenghts are in mm.

Table 6.6 summarizes the geometric parameters of the CAD prototype displayed in Figure 6.8: h_1, L_1, h_2 and L_2 are chosen to match closely the values of their respective ratios λ_1 and λ_2. Please note that λ_2, which is computed according to equation (6.10), is sufficiently smaller than one to allow the approximation expressed by expression (6.3).
In conclusion, Figure 6.9 shows the values of α and s calculated according to system (6.4): the chart displays both the exact solutions, computed using equation (3.6) to express θ_1 and θ_2, as well as the approximated functions obtained by means of expression (6.3). As shown by the figure, the difference is negligible. The charts also show that the phase difference between the translation and rotation motion remains constant during the whole cycle.

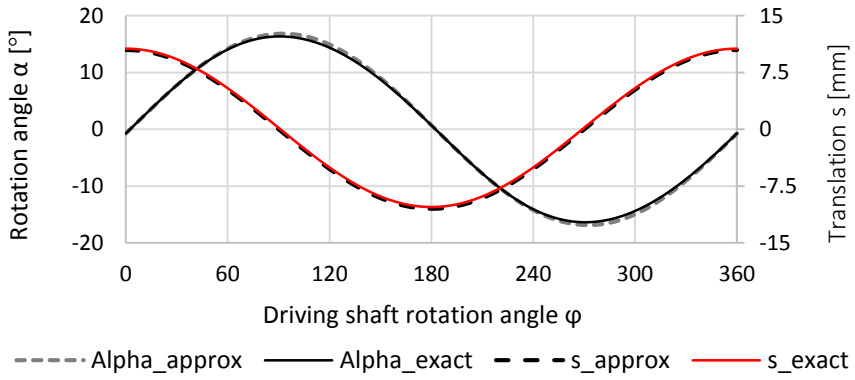

Figure 6.9: Exact and approximated solutions of the output motion.

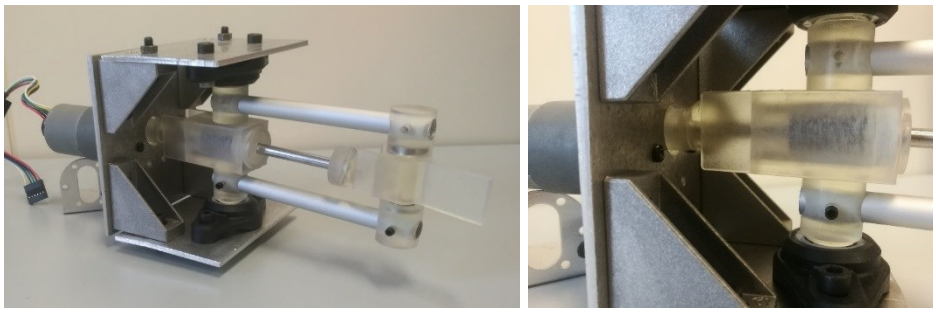

Figure 6.10: Physical prototype of the flapping mechanism.

The physical prototype of the proposed transmission mechanism is shown in Figure 6.10: the mechanical system has been assembled by using commercial components (ball bearings, flexible joints, metallic rods, etc) as well as funcional parte manufactured by high-resolution SLA 3-D printing techniques.

Chapter 7.

Concluding Remarks

7.1. Conclusions

The present dissertation is focused on the pursue of the maximal propulsive efficiency for a bio-inspired AUV. The vision, shared by researchers all around the world, is to replace the screw propellers commonly adopted by conventional underwater vehicles. In order to achieve this very ambitious aim, the fluid dynamics principles of marine animals' locomotion must be solidly understood, as novel mechatronic systems are developed in order to attain the highest mechanical efficiency and control robustness. Despite the manufactured robotic fish showed promising results, much is still to be done in order to match the propulsive performances of aquatic animals.

According to data collected by biologists and provided by literature, *thunniform* locomotion is the most efficient swimming mode in nature and many robotic fish have been prototyped following the flapping wing design style: here, the traditional architecture is composed by an open-chain N-joint mechanism assembled to generate the tail undulation, where each link is directly driven by a dedicated servomotor providing alternate motion. Since these actuators are not designed to be operated with continuous direction changes due to the power loss through heat, a possible source of efficiency improvement for the propulsive system of a *thunniform* swimming AUV, is the replacement of the aforementioned servomotors with the more performing DC brushed or brushless motors. This objective has been achieved in the first part of the research performed by the author of this dissertation: indeed, two transmission systems have been designed, both capable to convert – with an acceptable engineering approximation – the continuous rotation, at constant angular velocity, of the drive in the harmonic oscillation of the driven member. Particularly, the solution based on the spatial-cam kinematic joint has proved to be very solid, cheap, easy to manufacture and suited to vehicles of different size. Furthermore, the introduction of the proposed transmission mechanism has allowed to replace the non-linear position control required to a direct drive, with the constant angular velocity setting of the DC motor, thus incrementing the efficiency and reducing the control effort of the onboard NGC system.

Being new to the field of biomimetics applied to the marine field, the proposed solution has been integrated in the propulsive system of an *ostraciiform* swimming robot, where the latter is the easiest form of biological locomotion in terms of fin motion law, which simply consists in a pendulum-like harmonic oscillation. In order to predict the sensitivity of the thrust force and efficiency from the geometry and kinematics of the oscillating fin, a numerical analysis has been performed by using computational fluid dynamics techniques, whose results have been then exploited in the preliminary sizing of the aforementioned biomimetic AUV: despite the simplicity of the adopted method, it has allowed to manufacture a swimming robot whose

finals velocity, at the prescribed fin oscillation frequency, closely resembled the target speed. CFD analysis also permitted to verify the analytic model used to size a torsional spring suited to further optimize the mechanical efficiency of the robot driving system.
Numerical predictions offer a huge potential due their versatility and capability to compute the trends of the propulsive forces generated by the oscillating thruster. However, in order to confirm their trustworthiness, experimental tests must be performed to validate their results. Moreover, force measurements performed in the marine environment require watertight and expensive load cells or towing structures sliding above a water tank. Due to the unavailability of these equipments at the author's lab, a recirculating-flow water flume has been used, while a dedicated estensimetric force sensor, carefully sized to measure the loads in the prescribed range, has been successfully manufactured: the tests confirmed the accuracy of the performed numerical analysis, although the frequency range has been narrowed because the deflections at the highest oscillation pulse were too large to be neglected. Nevertheless, the tests allowed to validate the numerical predictions in the range on highest interest, i.e. close to the maximal efficiency condition.
CFD techniques allow to characterize the propulsive performances of the biomimetic thruster as a function of a sole, dimensionless parameter: the *Strouhal* number. Then, by applying the similitude principle, the computed force coefficients can be extended to underwater vehicles of different size. However, in order to obtain a complete model, the aforementioned trends must be coupled to the dynamic equations of the whole robot. The resulting system represents a multiphysics development environment, which integrates the results of CFD analysis in a proper multi-body model. In the present PhD dissertation, this method has been followed to compute the cruising speed of the *ostraciiform* swimming robot manufactured by the author and the obtained results closely approximated the forward velocity exhibited by the physical prototype. Moreover, the multiphysics approach has been also proposed as the platform for a sizing procedure applied to simple biomimetic robots.
Finally, a transmission mechanism has been developed to generate the fin flapping motion of *thunniform* swimmers. The mechanical systems devised by the author employs the spatial cam kinematic joint, already used for *ostraciiform* locomotion, as the basic module of a multi-segmented tail. The adoption of a single motor driving the kinematic chain allows to reduce the system inertia and encumbrance while eliminates the necessity to synchronize the various servomotors as frequently done in other biomimetic projects according to the state of the art. After a proper functional design, the proposed solution has been successfully prototyped and it's finally ready to be integrated in a fully-functional *thunniform* swimming robot.

7.2 Future work

Two robotic fish prototypes have been manufactured by the author of the present dissertation. Although their propulsive systems proved to be capable of generating enough thrust to drive the vehicles in straight forward navigation, their steering capability has not been addressed yet: indeed, both robots may adjust their heading by means of two horizontal screw propellers attached to the rigid forebody. Therefore, future developments of the aforesaid prototypes will be aimed to design biomimetic solutions exploiting the locomotion principles of Medium and Paired Fin (MPF) swimmers. The same purpose will be pursued about depth changing maneuvers in order to replace the vertical thruster with a mechanical system capable to adjust

the position of the vehicles center of mass, which in turn allows to modify the pitch attitude and thus to perform immersion and surfacing maneuvers. A second mechanical system will be integrated in the robot in order to adjust their buoyancy and thus exploit gravity to change its depth in a passively and energy-saving way.
Regarding the multi-body simulations, more accurate analysis will be performed in order to compute the vehicles turning radius in a turnabout maneuver. Particularly, the same method adopted for straight forward navigation will be followed both for heading and depth changing maneuvers to assess their sensitivity from the robots mass and inertia distributions, and from the thruster oscillation frequency as well. Moreover, the multiphysics dynamic environment developed for *ostraciiform* propulsion will be updated with numerical predictions accounting for the presence of the rigid forebody in front of the fin, with and without the effect of recoil; at the same time, the multi-body model will be coupled with trajectory planners and advanced control techniques in order to compute the effort required by the robot guidance system in a given mission. Finally, the resulting model will be imported in a simulation environment (i.e. Simulink) suited to couple advanced control techniques to the dynamics equations.
Further computational fluid dynamics analysis are currently underway, both to account for the presence of the rigid forebody in front of the fin, as already stated before, and to compute three-dimensional flow effects. However, the transition from in-plane analysis to a finite span foil denies the possibility to use the MIGALE research code already exploited in the present dissertation, while severely increasing the required computational time. Consequently, a few representative cases will be chosen before actually starting the 3-D numerical analysis.
Further experimental tests are also scheduled to validate the effectiveness of torsional spring integrated in the fin shaft. As a simple testing procedure, the duration of the battery pack used to power the propulsive system will be measured both with and without the presence of the torsional spring. Besides, the experimental setup already used to characterize the oscillating fin will be exploited to test the propulsive performances of a flapping foil, sized according to the resolution and sensitivity of the manufactured estensimetric force sensor. The obtained results will be also used to validate the numerical predictions performed on a roto-translating foil.
In conclusion, the primary objective of the present PhD dissertation has been the pursue of the maximal efficiency for a biomimetic thruster and a solution has been proposed for both the concurring factors in the computation of the aforementioned quantity. Particularly, the mechanical efficiency of the driving system has been improved by replacing the servomotors usually employed in robotic fish design, with a high-performing DC brushed and getting the system ready for a future brushless motor option. The core of the proposed solution is a novel transmission mechanism capable to generate flapping motion law optimized by the numerical predictions performed of its driven member. In this way, the most efficient swimming mode in nature has been adopted. Whether the resulting propulsive system matches the expected performances, it will be verified in future experimental test.

7.3 Contributions

At the best of the author's knowledge, the transmission mechanisms designed to generate the fin motion law respectively exhibited by *ostraciiform* and *thunniform* swimmers have never been used to in the driving systems of robotic fish.

The same consideration stands for the multiphysics environment developed by the author to predict, design and validate the solutions devised for bio-inspired propulsion.
Finally, this dissertation can also be seen as a handbook for researchers who aim at the design and realization of a prototype: as a matter of fact, all the aspects that concern the kinematic and dynamic analysis of a simple class of robotic fish are considered and a helpful approach to the structural design and sealing of such vehicles is presented, with the support of a small CAD library. Furthermore, the tests performed on the manufactured *ostraciiform* swimming prototypes demonstrate the effectiveness of the decisions made.

7.4 Publications arising from the research

- D. Costa, G. Palmieri, M-C. Palpacelli, M. Callegari, and D. Scaradozzi, "Design of a bio-inspired underwater vehicle". IEEE/ASME International Conference on Mechatronic and Embedded Systems and Applications (MESA), pp. 1-6, 2016.
- Caiti, E. Ciaramella, G. Conte, G. Cossu, D. Costa, S. Grechi, D. Scaradozzi, R. Nuti and A. Sturniolo, "OptoCOMM: introducing a new optical underwater wireless communication modem". IEEE Third Underwater Communications and Networking Conference (UComms), pp. 1-5, 2016.
- Bartolini, A. Caiti, E. Ciaramella, G. Conte, G. Cossu, S. Grechi, D. Costa, D. Scaradozzi, R. Nuti and A. Sturniolo, "OptoCOMM: Development and experimentation of a new optical wireless underwater modem". MTS/IEEE OCEANS, pp. 1-5, 2016.
- D. Costa, M. Franciolini, G. Palmieri, A. Crivellini, and D. Scaradozzi, "Computational fluid dynamics analysis and design of an ostraciiform swimming robot". IEEE International Conference on Robotics and Biomimetics (ROBIO), pp. 135-140, 2017.
- D. Scaradozzi, G. Palmieri, D. Costa, and A. Pinelli, "BCF swimming locomotion for autonomous underwater robots: a review and a novel solution to improve control and efficiency". Ocean Engineering, Vol. 130, pp. 437-453, 2017.
- D. Scaradozzi, G. Palmieri, D. Costa, S. Zingaretti, L. Panebianco, N. Ciuccoli, A. Pinelli, and M. Callegari, "UNIVPM BRAVe: A Hybrid Propulsion Underwater Research Vehicle", International Journal of Automation Technology, IJAT, Vol. 11(3), pp. 404-414, 2017.
- D. Costa, G. Palmieri, M. C. Palpacelli, L. Panebianco, and D. Scaradozzi, "Design of a Bio-Inspired Autonomous Underwater Robot". Journal of Intelligent & Robotic Systems, pp. 1-12, 2017.
- Bartolini, A. Caiti, E. Ciaramella, G. Cossu, D. Costa, D. Scaradozzi, S. Grechi, A. Messa and A. Sturniolo, "Sea-trial of Optical Ethernet Modems for Underwater Wireless Communications". Journal of Lightwave Technology, 2018.
- D. Costa, M. Callegari, G. Palmieri, D. Scaradozzi, M. Brocchini, G. Zitti, "Experimental setup for the validation of the bio-inspired thruster of an ostraciiform swimming robot". In IEEE/ASME International Conference on Mechatronic and Embedded Systems and Applications (MESA*)*, pp. 1-6, 2018.
- D. Costa, G. Palmieri, D. Scaradozzi, and M. Callegari, "Multi-body Analysis of a Bio-Inspired Underwater Robot". In The International Conference of IFToMM ITALY, Springer, pp. 240-248, 2018.

D. Costa, G. Palmieri, D. Scaradozzi, and M. Callegari, “Functional Design of a Biomimetic Flapper”. In IFToMM Symposium on Mechanism Design for Robotics, Springer, pp. 302-309, 2018.

References

[1] B. Lantos, and L. Márton, “Nonlinear control of vehicles and robots”. Springer Science & Business Media, 2010.

[2] W. H. Wang, R. C. Engelaar, X. Q. Chen, and J. G. Chase, “The state of art of underwater Vehicles - Theories and Applications”. In Mobile robots: state of the art in land, sea, air, collaborative missions, I-Tech Education, pp. 129-152, 2009.

[3] B. Allotta, A. Caiti, R. Costanzi, F. Fanelli, D. Fenucci, E. Meli, and A. Ridolfi, “A new AUV navigation system exploiting unscented Kalman filter”. Ocean Engineering, Vol. 113, pp. 121-132, 2016.

[4] D. Smallwood, and L. Whitcomb, “Model-based dynamic positioning of underwater robotic vehicles: theory and experiment”. IEEE Journal of Oceanic Engineering, Vol. 29, No. 1, pp. 169-186, 2004.

[5] J. Horgan, and D. Toal, “Review of machine vision applications in unmanned underwater vehicles”. International Conference on Control, Automation, Robotics and Vision (ICARCV), pp. 1-6, 2006.

[6] M. S. Triantafyllou and G. S. Triantafyllou, “An efficient swimming machine”. Science America, Vol. 272, pp. 40–46, 1995.

[7] J. Gray, “Studies in animal locomotion. VI. The propulsive powers of the dolphin”. Journal of experimental biology, Vol. 13, pp. 192–199, 1936.

[8] A. Crespi, B. Andre, G. Andre and A.J. Ijspeert, “AmphiBot I: An amphibious snake-like robot”. Robotics and Autonomous Systems, Vol. 50(4), pp. 163-175, 2005.

[9] T. Salumäe, R. Raag, J. Rebane, A. Ernits, G. Toming, M. Ratas, and M. Kruusmaa, “Design principle of a biomimetic underwater robot U-Cat”. In IEEE Oceans, pp. 1-5, 2014.

[10] C. Laschi, “Octobot-A robot octopus points the way to soft robotics”. IEEE Spectrum, Vol. 54(3), pp. 38-43, 2017.

[11] M. Rufo, M. Smithers, “GhostSwimmer™ AUV: Applying Biomimetics to Underwater Robotics for Achievement of Tactical Relevance”. Marine Technology Society Journal, Vol. 45(4), pp. 24-30, 2011.

[12] M. Sfakiotakis, D. M. Lane, J. B. Davies, "Review of fish swimming modes for aquatic locomotion". Oceanic Engineering, IEEE Journal of, Vol.24(2), pp. 237-252, 1999.

[13] C. M. Breder, "The Locomotion of Fish". Zoologica, vol. 4, pp. 159-256, 1926.

[14] P. W. Webb, "Forms and functions in fish swimming". Science America, Vol 251, pp. 56-68, 1984.

[15] M. J. Lighthill, "Hydromechanics of Aquatic Animal Propulsion". Annual Review of Fluid Mechanics, Vol.1(1), pp. 413-446, 1969.

[16] M. J. Lighthill, “Aquatic animal propulsion of high hydrodynamic efficiency”. Journal of Fluid Mechanics, Vol. 44, pp. 265-301, 1970.

[17] G. S. Triantafyllou, M. S. Triantafyllou, and M. A. Grosenbauch, “Optimal thrust development in oscillating foils with application to fish propulsion”. Journal of Fluids Structure, Vol. 7, pp. 205–224, 1993.

[18] C. Eloy, “Optimal Strouhal number for swimming animals”. Journal of Fluids and Structure, vol. 30, pp. 205-208, 2012.

[19] D. S. Barrett, M. S. Triantafyllou, D. K. P. Yue, M. A. Grosenbaugh, and M. Wolfgang, “Drag reduction in fish-like locomotion”. Journal of Fluid Mechanics, Vol. 392, pp. 183-212, 1999.

[20] L. Wen, J. Liang, G. Wu, and J. Li, "Hydrodynamic experimental investigation on efficient swimming of robotic fish using self-propelled method". International Journal of Offshore and Polar Engineering, Vol. 20(3), pp. 167-174, 2010.

[21] A. J . Murphy, and M. Haroutunian "Using bioInspiration to improve capabilities of underwater vehicles". 17th International Unmanned Untethered Submersible Technology Conference (UUST), pp. 20-31, 2011.
[22] M. J. Lighthill, "Note on the swimming of slender fish". Journal of fluid Mechanics Vol. 9(2), pp. 305-317, 1960.
[23] M. J. Lighthill, "Large-amplitude elongated-body theory of fish locomotion". Proceedings of the Royal Society of London, Series B, Vol. 179(1055), pp. 125-138, 1971.
[24] D. Barrett, M. Grosenbaugh, and M. Triantafyllou. "The optimal control of a flexible hull robotic undersea vehicle propelled by an oscillating foil". Proceedings of the IEEE 1996 Symposium on Autonomous Underwater Vehicle Technology, (AUV'96), pp. 1-9, 1996.
[25] J. M. Anderson and P. A. Kerrebrock, "The vorticity control unmanned undersea vehicle (VCUUV). An autonomous vehicle employing fish swimming propulsion and maneuvering". Proceedings of the International Symposium on Unmanned Untethered Submersible Technology (UUST '97), pp. 189–195, 1997.
[26] J. M. Anderson, K. Streitlien, D. S. Barrett, and M. S. Triantafyllou, "Oscillating foils of high propulsive efficiency". Journal of Fluid Mechanics, Vol. 360, pp. 41-72, 1998.
[27] R. Blickhan, and J. Y. Cheng, "Energy storage by elastic mechanisms in the tail of large swimmers - a re-evaluation". Journal of Theoretical Biology, Vol. 168(3), pp. 315-321, 1994.
[28] K. A. Harper, M. D. Berkemeier, and S. Grace, "Modeling the dynamics of spring-driven oscillating foil propulsion". IEEE Journal of Oceanic Engineering, Vol. 23(3), pp. 285-296, 1998.
[29] D. S. Barrett, "The Design of a Flexible Hull Undersea Vehicle Propelled by an Oscillating Foil". Massachusetts Institute of Technology, Department of Ocean Engineering, 1994.
[30] K. Hirata, "Development of experimental fish robot". Sixth International Symposium on Marine Engineering, pp. 23-27, 2000.
[31] J. M. Anderson, and N. K. Chhabra. "Maneuvering and stability performance of a robotic tuna". Integrative and Comparative Biology, Vol. 42(1), pp. 118-126, 2002.
[32] T. Fukuda, A. Kawamoto, F. Arai, and H. Matsuura, "Mechanism and swimming experiment of micro mobile robot in water". In Proceedings of the 1994 IEEE International Conference on Robotics and Automation, pp. 814-819, 1994.
[33] B. Kim, D. H. Kim, J. Jung, and J. O. Park, "A biomimetic undulatory tadpole robot using ionic polymer–metal composite actuators". Smart Materials and Structures, Vol. 14(6), 2005.
[34] X. Tan, D. Kim, N. Usher, D. Laboy, J. Jackson, A. Kapetanovic, and X. Zhou, "An autonomous robotic fish for mobile sensing". IEEE/RJS International Conference on Intelligent Robots and Systems, pp. 5424-5429, 2006.
[35] X. Ye, Y. Su, S. Guo, and T. Wang, "Infrared motion guidance and obstacle avoidance of an ICPF actuated underwater microrobot." IEEE International Conference on Mechatronic and Automation (ICMA 2007), pp. 1851-1856, 2007.
[36] J. Yu, S. Wang, and M. Tan. "Design of a free-swimming biomimetic robot fish". Proceedings of the IEEE/ASME International Conference on Advanced Intelligent Mechatronics, (AIM 2003), Vol. 1, pp. 95-100, 2003.
[37] J. Yu, M. Tan, S. Wang, and E. Chen, "Development of a biomimetic robotic fish and its control algorithm". IEEE Transactions on Systems, Man and Cybernetics, Part B, Vol. 34(4), pp. 1798-1810, 2004.
[38] J. Yu, and L. Wang, "Parameter optimization of simplified propulsive model for biomimetic robot fish". Proceedings of the IEEE International Conference on Robotics and Automation (ICRA 2005), pp. 3306-3311, 2005.
[39] J. Yu, L. Wang, and M. Tan. "Geometric optimization of relative link lengths for biomimetic robotic fish". IEEE Transactions on Robotics, Vol. 23(2), pp. 382-386, 2007.
[40] L. Zhang, W. Zhao, Y. Hu, D. Zhang, and L. Wang, "Development and depth control of a biomimetic robotic fish". IEEE/RSJ International Conference on Intelligent Robots and Systems (IROS 2007), pp. 3560-3565, 2007.

[41] C. Zhou, M. Tan, N. Gu, Z. Cao, S. Wang, L. Wang “Design and Implementation of a biomimetic robotic fish”. International Journal of Advanced Robotic Systems, Vol. 5(2), pp. 185-192, 2008.
[42] A. Suleman, and C. Crawford, "Studies on Hydrodynamic Propulsion of a Biomimetic Tuna". Underwater Vehicles, pp. 459-486, 2008.
[43] L. J. Garner, L. N. Wilson, D. C. Lagoudas, and O. K. Rediniotis, “Development of a shape memory alloy actuated biomimetic vehicle”. Smart Materials and Structures, Vol. 9(5), 2000.
[44] B. P. Epps, P. Valdivia y Alvarado, K. Youcef-Toumi, and A. H. Techet , “Swimming performance of a biomimetic compliant fish-like robot”. Experimental Fluids, Vol. 47(6), pp. 927–939, 2009.
[45] C. Stefanini, S. Orofino, L. Manfredi, S. Mintchev, S. Marrazza, T. Assaf, L. Capantini, E. Sinibaldi, S. Grillner, P. Wallén, and P. Dario, “A novel autonomous, bioinspired swimming robot developed by neuroscientists and bioengineers”. Bioinspiration & Biomimetics, Vol. 7(2), 2012.
[46] M. Kruusmaa, P. Fiorini, W. Megill, M. De Vittorio, O. Akanyeti, F. Visentin, L. Chambers, H. El Daou, M.-C. Fiazza, J. Jezov, M. Listak, L. Rossi, T. Salumae, G. Toming, R. Venturelli, D. Jung, J. Brown, F. Rizzi, A. Qualtieri, J. Maud, and A. Liszewski, “Filose for svenning: A flow sensing bioinspired robot”. IEEE Robotics Automation Magazine, Vol. 21(3), pp. 51–62, 2014.
[47] Y. Zhong, Z. Li, and R. Du, “A novel robot fish with wire-driven active body and compliant tail”. IEEE/ASME Transactions on Mechatronics, 22(4), pp. 1633-1643, 2017.
[48] J. Liu, and H. Hu. "Mimicry of sharp turning behaviours in a robotic fish". Proceedings of the IEEE International Conference on Robotics and Automation (ICRA 2005), pp. 3318-3323, 2005.
[49] J. Liu, and H. Hu, “Biological inspiration: from carangiform fish to multi-joint robotic fish”. Journal of Bionic Engineering, Vol. 7(1), pp. 35-48, 2010.
[50] P. Nilas, N. Suwanchit, and R. Lumpuprakarn, “Prototypical robotic fish with swimming locomotive configuration in fluid environment”. Proceedings of the International MultiConference of Engineers and Computer Scientists, Vol. 2, 2011.
[51] P. Nilas, “A prototypical multi-locomotive robotic fish parametric research and design”. Proceedings of the World Congress on Engineering and Computer Science, Vol. 1, pp. 19-21, 2011.
[52] D. Korkmaz, U. Budak, C. Bal, G. O. Koca, Z. H. Akpolat, "Modeling and implementation of a biomimetic robotic fish." 2012 International Symposium on Power Electronics, Electrical Drives, Automation and Motion (SPEEDAM), pp.1187,1192, 2012.
[53] A. D. Marchese, “Design, fabrication, and control of soft robots with fluidic elastomer actuators”. PhD dissertation, Massachusetts Institute of Technology, 2015.
[54] P. Kodati, J. Hinkle, A. Winn, and X. Deng, “Microautonomous Robotic Ostraciiform (MARCO): hydrodynamics, design and fabrication”. IEEE Transaction on Robotics, Vol. 24(1), pp. 105-117, 2008.
[55] F. Bassi, S. Rebay, “Numerical evaluation of two discontinuous Galerkin methods for the compressible Navier–Stokes equations”. International journal for numerical methods in fluids, Vol. 40 (1-2), pp. 197-207, 2002.
[56] F. Bassi, A. Crivellini, D. A. Di Pietro, S. Rebay, “An implicit high-order discontinuous Galerkin method for steady and unsteady incompressible flows”. Computers & Fluids, Vol. 36(10), pp. 1529-1546, 2007.
[57] F. Bassi, A. Crivellini, S. Rebay, M. Savini, “Discontinuous Galerkin solution of the Reynolds-averaged Navier–Stokes and k–ω turbulence model equations”. Computers & Fluids, Vol. 34(4), pp. 507-540, 2005.
[58] A. Crivellini, V. D’Alessandro, F. Bassi, “A Spalart–Allmaras turbulence model implementation in a discontinuous Galerkin solver for incompressible flows”. Journal of Computational Physics, Vol. 241, pp. 388-415, 2013.
[59] F. Bassi, L. Botti, A. Colombo, A. Crivellini, N. Franchina, A. Ghidoni, “Assessment of a high-order accurate Discontinuous Galerkin method for turbomachinery flows”. International Journal of Computational Fluid Dynamics, Vol. 30(4), pp. 307-328, 2016.

[60] F. Bassi, S. Rebay, G. Mariotti, S. Pedinotti, M. Savini, "A high-order accurate discontinuous finite element method for inviscid and viscous turbomachinery flows". Proceedings of the 2nd European Conference on Turbomachinery Fluid Dynamics and Thermodynamics, pp. 99-109, 1997.
[61] S. Balay, M. F. Adams, J. Brown, P. Brune, K. Buschelman, V. Ei- jkhout, W. D. Gropp, K. D., M. G. Knepley, L. C. McInnes, F. Barry, K. R. Smith, and H. Zhang, "PETSc Web page." http://www.mcs.anl.gov/petsc, 2014.
[62] D. Costa, M. Franciolini, G. Palmieri, A. Crivellini, and D. Scaradozzi, "Computational fluid dynamics analysis and design of an ostraciiform swimming robot". IEEE International Conference on Robotics and Biomimetics (ROBIO), pp. 135-140, 2017.
[63] D. Tzeranis, E. Papadopoulos, G. Triantafyllou, "On the Design of an Autonomous Robot Fish". Proceedings of the 11th IEEE Mediterranean Conference on Control and Automation (MED), pp. 17-20, 2003.
[64] R. W. Blake, "On *ostraciiform* locomotion". Journal of the Marine Biological Association of the United Kingdom, Vol 57(4), pp. 1047-1055, 1977.
[65] F. D. Jones, H. L. Horton, and J. A. Newell, "Ingenious mechanisms for designers and inventors". Industrial Press Inc., 1930.
[66] D. Costa, G. Palmieri, M-C. Palpacelli, M. Callegari, and D. Scaradozzi, "Design of a bio-inspired underwater vehicle". IEEE/ASME International Conference on Mechatronic and Embedded Systems and Applications (MESA), pp. 1-6, 2016.
[67] D. Scaradozzi, G. Palmieri, D. Costa, and A. Pinelli, "BCF swimming locomotion for autonomous underwater robots: a review and a novel solution to improve control and efficiency". Ocean Engineering, Vol. 130, pp. 437-453, 2017.
[68] D. Scaradozzi, G. Palmieri, D. Costa, S. Zingaretti, L. Panebianco, N. Ciuccoli, A. Pinelli, and M. Callegari, "UNIVPM BRAVe: A Hybrid Propulsion Underwater Research Vehicle", International Journal of Automation Technology, IJAT, Vol. 11(3), pp. 404-414, 2017.
[69] D. Costa, G. Palmieri, M. C. Palpacelli, L. Panebianco, and D. Scaradozzi, "Design of a Bio-Inspired Autonomous Underwater Robot". Journal of Intelligent & Robotic Systems, pp. 1-12, 2017.
[70] L. I. Sedov, Two-dimensional problems of hydrodynamics and aerodynamics, Moscow Izdatel Nauka, 1980.
[71] https://www.pololu.com/product/2824.
[72] A. Caiti, E. Ciaramella, G. Conte, G. Cossu, D. Costa, S. Grechi, D. Scaradozzi, R. Nuti and A. Sturniolo, "OptoCOMM: introducing a new optical underwater wireless communication modem". IEEE Third Underwater Communications and Networking Conference (UComms), pp. 1-5, 2016.
[73] A. Bartolini, A. Caiti, E. Ciaramella, G. Conte, G. Cossu, S. Grechi, D. Costa, D. Scaradozzi, R. Nuti and A. Sturniolo, "OptoCOMM: Development and experimentation of a new optical wireless underwater modem". MTS/IEEE OCEANS, pp. 1-5, 2016.
[74] A. Bartolini, A. Caiti, E. Ciaramella, G. Cossu, D. Costa, D. Scaradozzi, S. Grechi, A. Messa and A. Sturniolo, "Sea-trial of Optical Ethernet Modems for Underwater Wireless Communications". Journal of Lightwave Technology, 2018.
[75] D.A. Pabst, "Springs in swimming animals". American Zoologist, Vol. 36(6), pp. 723-735, 1994.
[76] S. Kobayashi, M. Nakabayashi and H. Morikawa, " Bioinspired propulsion mechanism in fluid using fin with dynamic variable-effective-length-spring". Journal of Biomechanical Science and Engineering, Vol. 1(1), pp. 280-289, 2006.
[77] M. Nakabayashi, R. Kobayashi, S. Kobayashi, and H. Morikawa, "Bioinspired propulsion mechanism using a fin with a dynamic variable-effective-length-spring". Journal of Biomechanical Science and Engineering, Vol. 4(1), pp. 82-93, 2009.
[78] B. Allotta, A. Caiti, L. Chisci, R. Costanzi, F. Di Corato, C. Fantacci, D. Fenucci, E. Meli, A, Ridolfi, "Development of a navigation algorithm for autonomous underwater vehicles". IFAC

Workshop on Navigation, Guidance and Control of Underwater Vehicles (NGCUV 2015), Girona, Vol.28(2), pp. 64-69, 2015.
[79] B. Allotta, R.. Costanzi, A. Ridolfi, M. Reggiannini, M., Tampucci, & D. Scaradozzi, "Archaeology oriented optical acquisitions through MARTA AUV during ARROWS European project demonstration". MTS/IEEE OCEANS 2016, pp. 1-4, 2016.
[80] G. Conte, G.P. De Capua, D. Scaradozzi," Designing the NGC system of a small ASV for tracking underwater targets". Robotics and Autonomous Systems, Vol. 76(1), pp. 46-57, 2016.
[81] G. Conte, L. Gambella, D. Scaradozzi, S. Zanoli, A. Caiti, V. Calabrò, A. Alcocer, J. Alves, B. Cardeira, R. Cunha, F. Curado, P. Oliveira, A. Oliveira, A. Pascoal, M. Rufino, L. Sebastĩo, C. Silvestre, "Underwater vehicle technology in the European research project VENUS". Underwater Technology, Vol.28(4), pp. 175-185, 2009.
[82] G. Conte, D. Scaradozzi, L. Sorbi, L. Panebianco, D. Mannocchi,, "ROS multi-agent structure for autonomous surface vehicles". MTS/IEEE OCEANS, 2015.
[83] D. Scaradozzi, L. Sorbi, and G. Conte, "Assisted guidance system for Micro ROV in underwater data gathering missions". Proceedings of the Mediterranean Conference of Control and Automation (MED), pp. 1373–1378, 2012.
[84] M. Wooldridge, "An introduction to muliagents systems, John Wiley & Sons, 2009.
[85] Y. J. Park, U. Jeong, J. Lee, S. R. Kwon, H. Y. Kim, and K. J. Cho, "Kinematic condition for maximizing the thrust of a robotic fish using a compliant caudal fin". IEEE Transaction of Robotics, Vol. 28 (6), pp. 1216-1227, 2012.
[86] P. Prempraneerach, F. S. Hover, and M. S. Triantafyllou, "The effect of chordwise flexibility on the thrust and efficiency of a flapping foil". International Symposium on Unmanned Untethered Submersible Technology (UUST), Vol. 152, pp. 150-170, 2003.
[87] K. H. Low, C. W. Chong, and C. Zhou, "Performance study of a fish robot propelled by a flexible caudal fin". IEEE International Conference on Robotics and Automation (ICRA), pp. 90-95, 2010.
[88] G. V. Lauder, E. J. Anderson, J. Tangorra, and P. A. Madden, "Fish biorobotics: kinematics and hydrodynamics of self-propulsion": The Journal of Experimental Biology, Vol. 210, pp. 2767-2780, 2007.
[89] S. Wang, G. He, X. Zhang, "Self-propulsion of flapping bodies in viscous fluids: recent advances and perspectives". Acta Mechanica Sinica, Vol. 32 (6) pp. 980-990, 2016.
[90] W. L. Chan, T. Kang, and Y. J. Lee, "Experiments and identification of an ostraciiform fish robot". IEEE International Conference on Robotics and Biomimetics (ROBIO), pp. 530-534, 2007.
[91] K. Hoffmann, "An introduction to stress analysis and transducer design using strain gages". HBM, www.hbm.com, 2012.
[92] D. Costa, M. Callegari, G. Palmieri, D. Scaradozzi, M. Brocchini, G. Zitti, "Experimental setup for the validation of the bio-inspired thruster of an ostraciiform swimming robot". In IEEE/ASME International Conference on Mechatronic and Embedded Systems and Applications (MESA*)*, pp. 1-6, 2018.
[93] Y. X. Liu, W. S. Chen, J. K. Liu, "Research on the swing of the body of two-joint robot fish". Journal of Bionic Engineering, Vol (5), pp. 159-165, 2008.
[94] J. Liu, H. Hu, "A 3D simulator for autonomous robotic fish". International Journal of automation and computing, Vol. 1 (1), pp. 42-50, 2004.
[95] K. A. Morgansen, B. I. Triplett, and D. J. Klein, "Geometric methods for modeling and control of free-swimming fin-actuated underwater vehicles". IEEE Transactions on Robotics, Vol. 23 (6), pp. 1184-1199, 2007.
[96] Q. Liu, "Research on dynamics performance of robotic fish based on ADAMS". International Conference on Measuring Technology and Mechatronics Automation (ICMTM), Changsha, Vol. 3, pp. 61-65, 2010.
[97] L. Wen, J. Liang, Q. Shen, L. Bao, and Q. Zhang, "Hydrodynamic performance of an undulatory robot: Functional roles of the body and caudal fin locomotion". International Journal of Advanced Robotic Systems, Vol. 10 (1), pp. 5-14, 2013.

[98] G. Antonelli, “Underwater robots, motion and force control of vehicle-manipulator systems”. Springer Berlin Heidelberg, 2008.
[99] T. I. Fossen, “Marine Control System-Guidance, Navigation and Control of Ships, Rigs and Underwater Vehicles”. Marine Cybernetics, 2002.
[100] D. Costa, G. Palmieri, D. Scaradozzi, and M. Callegari, “Multi-body Analysis of a Bio-Inspired Underwater Robot”. In The International Conference of IFToMM ITALY, Springer, pp. 240-248, 2018.
[101] D. Costa, G. Palmieri, D. Scaradozzi, and M. Callegari, “Functional Design of a Biomimetic Flapper”. In IFToMM Symposium on Mechanism Design for Robotics, Springer, pp. 302-309, 2018.
[102] L. Schouveiler, F. S. Hover, and M. S. Triantafyllou, “Performance of flapping foil propulsion”. Journal of Fluids and Structures, Vol. 20(7), pp. 949-959, 2005.

Appendix A.

LabVIEW software architecture

A.1. LabVIEW block diagram

As stated in Chapter 4, the software employed in the experimental setup has been developed in NI LabVIEW: particularly, it is composed by two real-time while loops running in parallel and dedicated to two different purposes: the control loop and the acquisition loop. The control loop has the classical state-machine architecture; its main function is to control the motor in order to adjust its frequency to the value set from the user, by means of a PI controller. The control loop is executed every 10 ms, ten times faster than the highest oscillation frequency planned in the test. On the other hand, the acquisition loop has the producer and consumer architecture: data gathered through the analogue input channels at high speed, once every 10 ms, are stored in a queue from the producer loop and then are passed to the slower consumer loop in order to be processes and saved in an external memory storage unit. The acquisition loop starts when a trigger button is pushed by the user: this very action simultaneously activates a dedicated subVI through which the *record start* command is sent, through the Wi-Fi connection, to the GoPro camera. Figures A1-4 show the compoents of the block diagram.

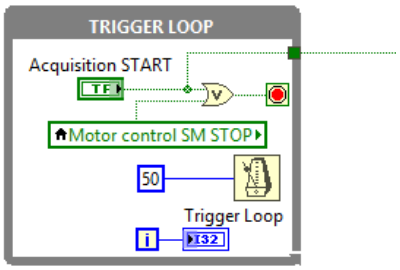

Figure A.1: LabVIEW Block Diagram. Trigger Loop. Used to syncronize the camera recording device with the measured signals acquired by the force sensor.

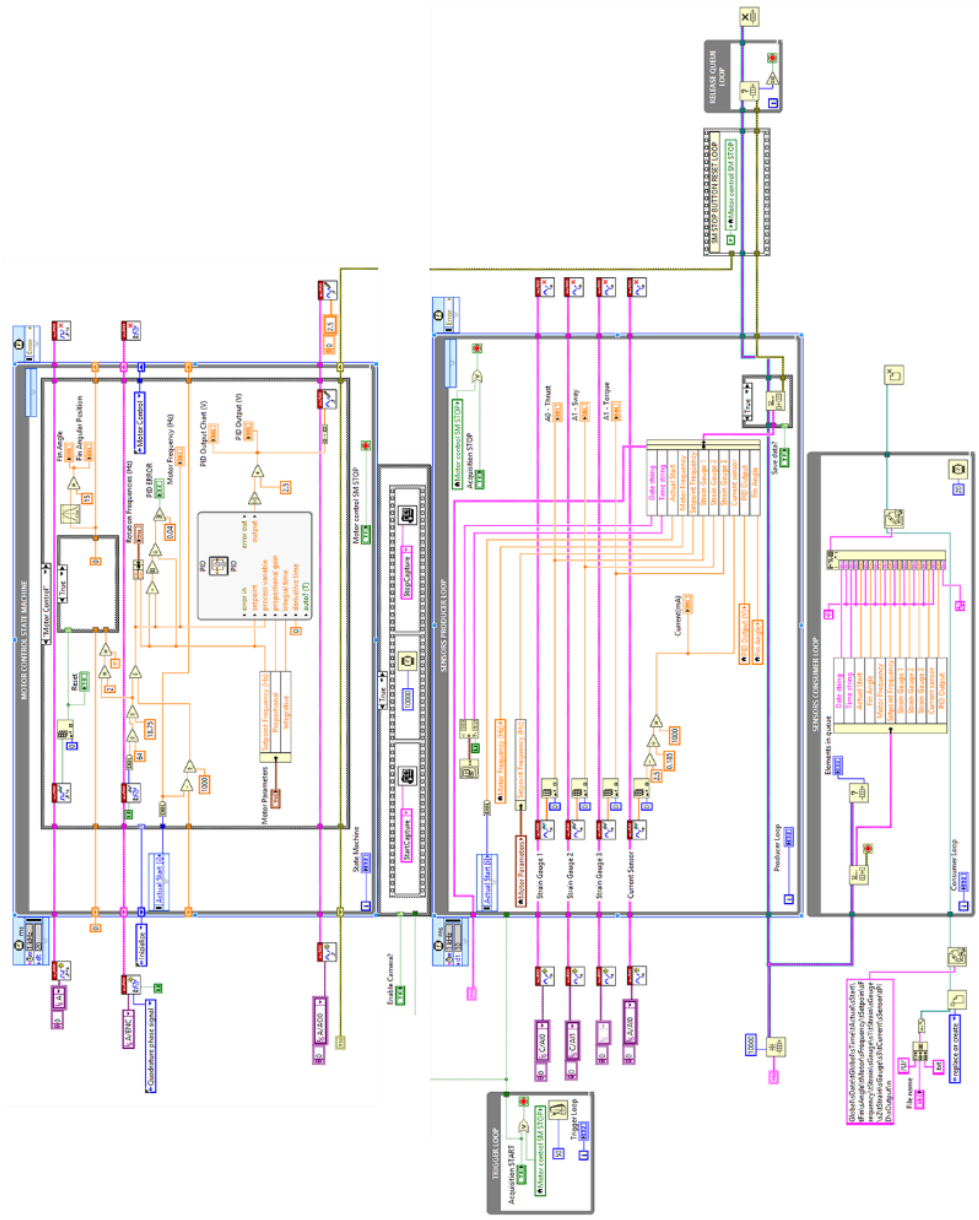

Figure A.2: Experimental tests software architecture. Overview of LabVIEW Block Diagram.

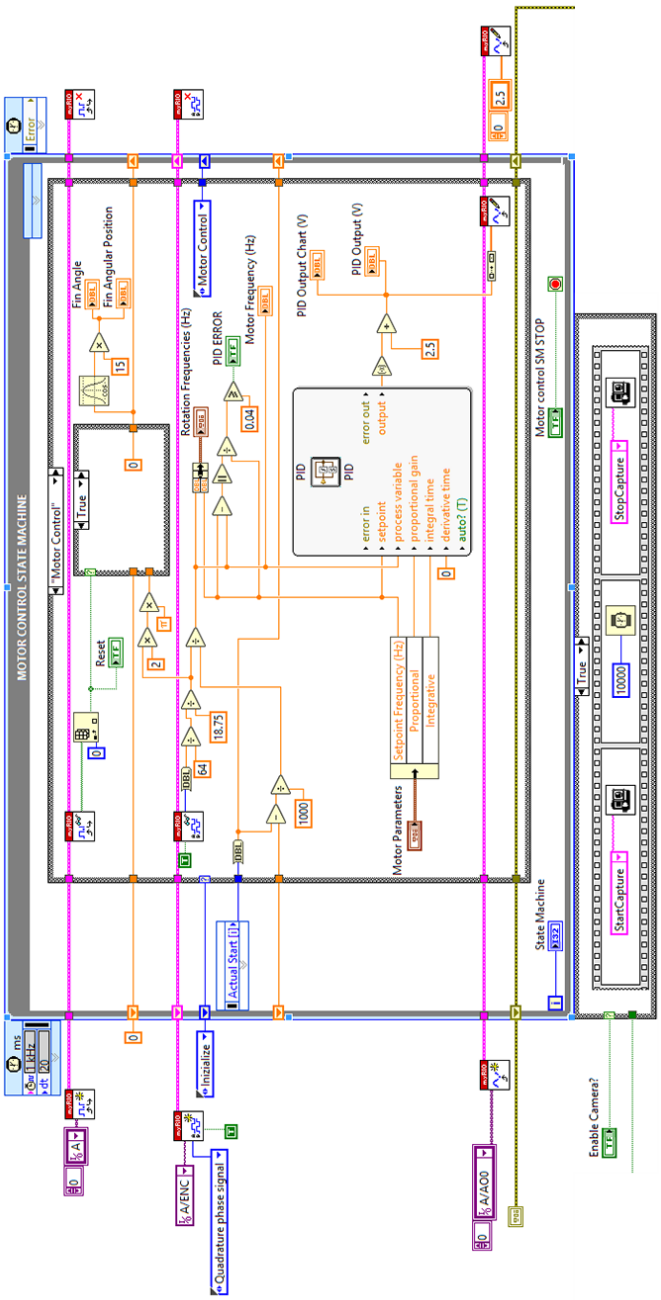

Figure A.3: LabVIEW Block Diagram. Control Loop (State Machine) and Camera Control (Sequence Structure).

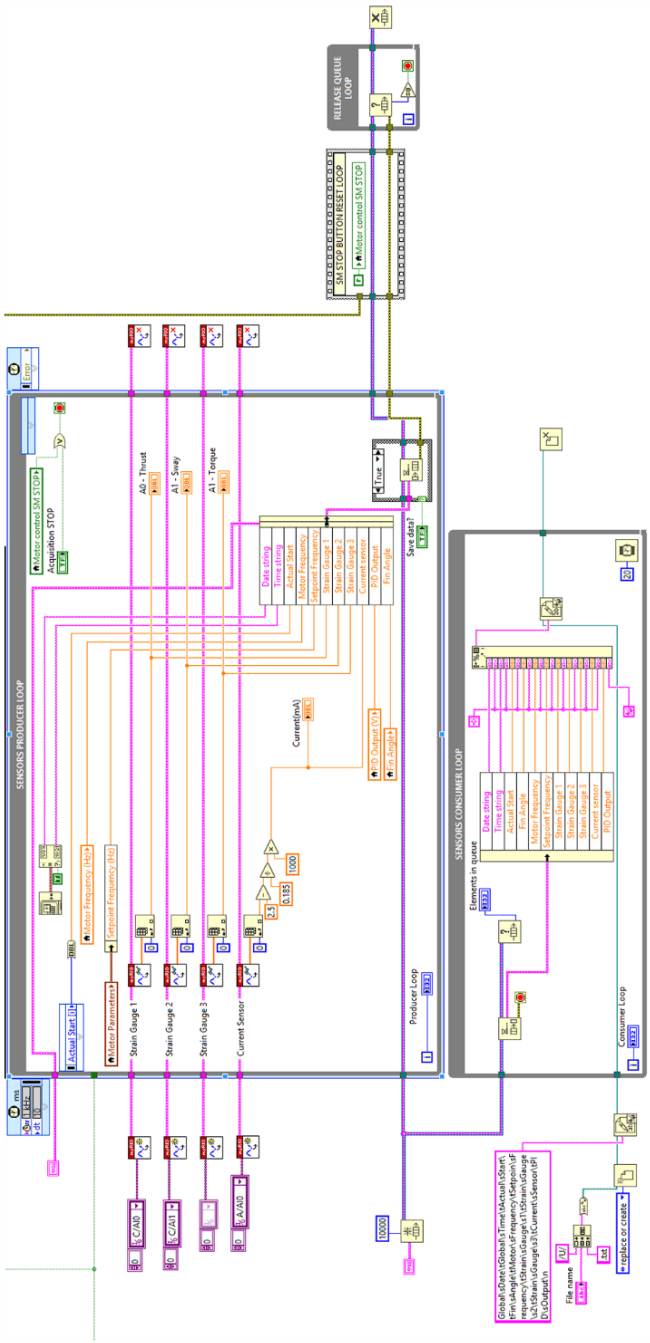

Figure A.4: LabVIEW Block Diagram. Acquisition Loop (Producer – Consumer).